

1

²A SEARCH FOR LONG-LIVED, CHARGED, SUPERSYMMETRIC PARTICLES
³USING IONIZATION WITH THE ATLAS DETECTOR

4

BRADLEY AXEN

5

September 2016 – Version 0.53

6



⁸ Bradley Axen: *A Search for Long-Lived, Charged, Supersymmetric Particles using*
⁹ *Ionization with the ATLAS Detector*, Subtitle, © September 2016

¹⁰

Usually a quotation.

¹¹

Dedicated to.

₁₂ ABSTRACT

₁₃ How to write a good abstract:

₁₄ <https://plg.uwaterloo.ca/~migod/research/beck00PSLA.html>

₁₅ PUBLICATIONS

₁₆ Some ideas and figures have appeared previously in the following publications:

₁₇

₁₈ Put your publications from the thesis here. The packages `multibib` or `bibtopic`
₁₉ etc. can be used to handle multiple different bibliographies in your document.

²¹ ACKNOWLEDGEMENTS

²² Put your acknowledgements here.

²³

²⁴ And potentially a second round.

²⁵

26 CONTENTS

27	I	INTRODUCTION	1
28	1	INTRODUCTION	3
29	II	THEORETICAL CONTEXT	5
30	2	STANDARD MODEL	7
31	2.1	Action and the Lagrangian	7
32	2.2	Gauge Invariance and Forces	8
33	2.2.1	$SU(2) \times U(1)$ and the Electroweak Force	10
34	2.2.2	$SU(3)$ and the Strong Force	10
35	2.3	Noether's Theorem, Charges, and Matter	10
36	2.3.1	Quarks	11
37	2.3.2	Leptons	12
38	2.3.3	Chirality	12
39	2.4	Higgs Mechanism and Mass	13
40	2.5	Phenomenology	14
41	2.5.1	Electroweak Physics	14
42	2.5.2	Strong Physics	15
43	2.5.3	Proton-Proton Collisions	15
44	2.6	Limitations	16
45	2.6.1	Theoretical Concerns	16
46	2.6.2	Cosmological Observations	18
47	3	SUPERSYMMETRY	21
48	3.1	Structure and the MSSM	21
49	3.2	Motivation	22
50	4	LONG-LIVED PARTICLES	23
51	4.1	Mechanisms	23
52	4.1.1	Examples in Supersymmetry	23
53	4.2	Phenomenology	23
54	4.2.1	Disimilarities to Prompt Decays	23
55	4.2.2	Characteristic Signatures	23
56	III	EXPERIMENTAL STRUCTURE AND RECONSTRUCTION	25
57	5	THE LARGE HADRON COLLIDER	27
58	5.1	Injection Chain	28
59	5.2	Design	29
60	5.2.1	Layout	29
61	5.2.2	Magnets	30
62	5.2.3	RF Cavities	31
63	5.2.4	Beam	33
64	5.3	Luminosity Parameters	33
65	5.4	Delivered Luminosity	35

66	6	THE ATLAS DETECTOR	37
67	6.1	Coordinate System	39
68	6.2	Magnetic Field	40
69	6.3	Inner Detector	42
70	6.3.1	Pixel Detector	45
71	6.3.2	Semiconductor Tracker	47
72	6.3.3	Transition Radiation Tracker	49
73	6.4	Calorimetry	50
74	6.4.1	Electromagnetic Calorimeter	52
75	6.4.2	Hadronic Calorimeters	53
76	6.5	Muon Spectrometer	55
77	6.5.1	Monitored Drift Tube	57
78	6.5.2	Resistive Plate Chamber	58
79	6.5.3	Cathode Strip Chamber	58
80	6.5.4	Thin Gap Chamber	58
81	6.6	Trigger	60
82	7	EVENT RECONSTRUCTION	63
83	7.1	Tracks and Vertices	63
84	7.1.1	Pixel Neural Network	65
85	7.1.2	Pixel dE/dx	66
86	7.1.3	Vertex Reconstruction	66
87	7.2	Electrons and Photons	67
88	7.2.1	Photon Identification	68
89	7.2.2	Electron Identification	68
90	7.3	Muons	68
91	7.3.1	Muon Identification	69
92	7.4	Jets	69
93	7.4.1	Topological Clustering	70
94	7.4.2	Jet Algorithms	71
95	7.4.3	Jet Energy Scale	72
96	7.5	Missing Transverse Energy	72
97	IV	CALORIMETER RESPONSE	75
98	8	RESPONSE MEASUREMENT WITH SINGLE HADRONS	77
99	8.1	Dataset and Simulation	78
100	8.1.1	Data Samples	78
101	8.1.2	Simulated Samples	78
102	8.1.3	Event Selection	78
103	8.2	Inclusive Hadron Response	79
104	8.2.1	E/p Distribution	79
105	8.2.2	Zero Fraction	80
106	8.2.3	Neutral Background Subtraction	81
107	8.2.4	Corrected Response	83
108	8.2.5	Additional Studies	85
109	8.3	Identified Particle Response	88
110	8.3.1	Decay Reconstruction	88

111	8.3.2	Identified Response	89
112	8.3.3	Additional Species in Simulation	91
113	8.4	Summary	92
114	9	JET ENERGY RESPONSE AND UNCERTAINTY	95
115	9.1	Motivation	95
116	9.2	Uncertainty Estimate	95
117	9.3	Summary	98
118	V	SEARCH FOR LONG-LIVED PARTICLES	101
119	10	LONG-LIVED PARTICLES IN ATLAS	103
120	10.1	Event Topology	103
121	10.1.1	Detector Interactions	104
122	10.1.2	Lifetime Dependence	105
123	10.2	Simulation	108
124	11	EVENT SELECTION	111
125	11.1	Trigger	112
126	11.2	Kinematics and Isolation	113
127	11.3	Particle Species Rejection	117
128	11.4	Ionization	120
129	11.4.1	Mass Estimation	121
130	11.5	Efficiency	122
131	12	BACKGROUND ESTIMATION	125
132	12.1	Background Sources	125
133	12.2	Prediction Method	126
134	12.3	Validation	127
135	12.3.1	Closure in Simulation	127
136	12.3.2	Validation Region in Data	128
137	13	SYSTEMATIC UNCERTAINTIES AND RESULTS	131
138	13.1	Systematic Uncertainties	131
139	13.1.1	Background Estimate	131
140	13.1.2	Signal Yield	132
141	13.2	Final Yields	138
142	13.3	Cross Sectional Limits	139
143	13.4	Mass Limits	141
144	13.5	Context for Long-Lived Searches	143
145	VI	CONCLUSIONS	147
146	14	SUMMARY AND OUTLOOK	149
147	14.1	Summary	149
148	14.2	Outlook	149
149	VII	APPENDIX	151
150	A	INELASTIC CROSS SECTION	153
151	B	EXPANDED R-HADRON YIELDS AND LIMITS	155
152		BIBLIOGRAPHY	161

153 LIST OF FIGURES

154	Figure 1	A Feynman diagram representing the interaction of the A field with a generic fermion, f	10
155			
156	Figure 2	The particle content of the Standard Model (SM)	12
157	Figure 3		
158			
159			
160			
161	Figure 4	The Feynman diagrams representing the decays of the W and Z bosons to fermions. Here f indicates a generic fermion, \bar{f} its antiparticle, and f' the partner of that fermion in the same generation.	15
162			
163			
164			
165			
166	Figure 5	The parton distribution functions (PDFs) for proton-proton collisions at $Q^2 = 10 \text{ GeV}^2$ and $Q^2 = 10^4 \text{ GeV}^2$. Each shows the fraction of particles which carry a fraction x of the total proton energy at the specified scale [1].	16
167			
168	Figure 6	An approximation of the running of the coupling constants in the SM up to the Planck scale [unification_plot].	17
169			
170			
171			
172	Figure 7	The distribution of velocities of stars as a function of the radius from the center of the galaxy. The contributions to the velocity from the various components of matter in the galaxy are shown [2].	18
173			
174			
175			
176	Figure 8	The four collision points and corresponding experiments of the Large Hadron Collider (LHC). The image includes the location of the nearby city of Geneva as well as the border of France and Switzerland.	28
177			
178			
179			
180			
181	Figure 9	The cumulative luminosity over time delivered to the A Toroidal LHC ApparatuS (ATLAS) experiment from high energy proton-proton collisions since 2011. The energies of the collisions are listed for each of the data-taking periods.	29
182			
183			
184			
185	Figure 10	The accelerator complex that builds up to the full design energies at the LHC . The protons are passed in order to Linac 2, the PSB , the PS , the SPS and then the LHC	30
186			
187			
188			
189	Figure 11	A schematic of the layout of the LHC , not to scale. The arched and straight sections are illustrated at the bottom of the schematic, and all four crossing sites are indicated with their respective experiments.	31
190			
191			
192			
193			
194			
		A cross section of the the cryodipole magnets which bend the flight path of protons around the circumference of the LHC . The diagram includes both the superconducting coils which produce the magnetic field and the structural elements which keep the magnets precisely aligned.	32

195	Figure 12	The arrangement of four radiofrequency (RF) cavities within a cryomodule.	32
196			
197	Figure 13	The cumulative luminosity versus time delivered to ATLAS (green), recorded by ATLAS (yellow), and certified to be good quality data (blue) during stable beams for pp collisions at 13 TeV in 2015.	35
198			
199			
200			
201	Figure 14	The luminosity-weighted distribution of the mean number of interactions per crossing for the 2015 pp collision data at 13 TeV.	36
202			
203			
204	Figure 15	A cut-away schematic of the layout of the ATLAS detector. Each of the major subsystems is indicated.	38
205			
206	Figure 16	A cross-sectional slice of the ATLAS experiment which illustrates how the various SM particles interact with the detector systems.	38
207			
208			
209	Figure 17	The layout of the four superconducting magnets in the ATLAS detector.	41
210			
211	Figure 18	The arrangement of the subdetectors of the ATLAS inner detector. Each of the subdetectors is labeled in the cut-away view of the system.	43
212			
213			
214	Figure 19	A quarter section of the ATLAS inner detector which shows the layout of each of the subdetectors in detail. The lower panel shows an enlarged view of the pixel detector. Example trajectories for a particle with $\eta = 1.0, 1.5, 2.0, 2.5$ are shown. The Insertible B-Layer (IBL), which was added after the original detector commissioning, is not shown.	43
215			
216			
217			
218			
219			
220			
221	Figure 20	A computer generated three-dimensional view of the inner detector along the line of the beam axis. The subdetectors and their positions are labeled.	44
222			
223			
224	Figure 21	An alternative computer generated three-dimensional view of the inner detector transverse to the beam axis. The subdetectors and their positions are labeled.	44
225			
226			
227	Figure 22	The integrated radiation lengths traversed by a straight track at the exit of the ID envelope, including the services and thermal enclosures. The distribution is shown as a function of $ \eta $ and averaged over ϕ . The breakdown indicates the contributions of individual subdetectors, including services in their active volume.	45
228			
229			
230			
231			
232			
233	Figure 23	48
234	Figure 24	An image of the insertion of the IBL into the current pixel detector.	48
235			
236	Figure 25	A three-dimensional computer-generated image of the geometry of the IBL with a view (a) mostly transverse to the beam pipe (b) mostly parallel to the beam pipe.	49
237			
238			
239	Figure 26	An exploded view of the geometry of the silicon microstrip (SCT) double layers in the barrel region.	50
240			

241	Figure 27	51
242	Figure 28	The depth of (a) the electromagnetic barrel calorimeter in radiation lengths and (b) all calorimeters in interaction lengths as a function of pseudorapidity.	52
243			
244			
245	Figure 29	A schematic of the Liquid Argon (LAr) calorimeter in the barrel region, highlighting the accordion structure.	52
246			
247	Figure 30	A schematic of a hadronic tile module which shows the alternating layers of steel and plastic scintillator.	54
248			
249	Figure 31	The segmentation in depth and η of the tile-calorimeter modules in the central (left) and extended (right) barrels.	54
250			
251	Figure 32	A cut-away diagram of the muon systems on ATLAS	55
252	Figure 33	A quarter view of the muon spectrometer which highlights the layout of each of the detecting elements. The BOL, BML, BIL, EOL, EML, and EIL are all Monitored Drift Tube (MDT) elements, where the acronyms encode their positions.	56
253			
254			
255			
256			
257	Figure 34	A schematic of the cross-section of the muon spectrometer in the barrel region.	56
258			
259	Figure 35	A schematic of a single MDT chamber, which shows the multilayers of drift tubes as well as the alignment system.	57
260			
261			
262	Figure 36	A schematic of the Cathode Strip Chamber (CSC) end-cap, showing the overlapping arrangement of the eight large and eight small chambers.	59
263			
264			
265	Figure 37	A schematic of the Thin Gap Chamber (TGC) doublet and triplet layers.	59
266			
267	Figure 38	The L1 Trigger rate broken down into the types of triggers as a function of the luminosity block for the 2015 data collection period.	61
268			
269			
270	Figure 39	The HLT Trigger rate broken down into the types of triggers as a function of the luminosity block for the 2015 data collection period.	62
271			
272			
273	Figure 40	The x and y locations of the hits generated in a simulated $t\bar{t}$ event in the inner detector. The hits which belong to tracks formed using the inside-out algorithm are highlighted in red, while the hits which belong to tracks formed using the outside-in algorithm are circled in black.	64
274			
275			
276			
277			
278			
279	Figure 41	Examples of the clusters formed in a single layer of the pixel detector for (a) a single isolated particle, (b) two nearly-overlapping particles, and (c) a particle which emits a δ -ray [14].	65
280			
281			
282			
283	Figure 42	The total, fractional jet energy scale (JES) uncertainties estimated for 2015 data as a function of jet p_T	73
284			

285	Figure 43	An illustration (a) of the E/p variable used throughout this paper. The red energy deposits come from the charged particle targeted for measurement, while the blue energy deposits are from nearby neutral particles and must be subtracted. The same diagram (b) for the neutral-background selection, described in Section 8.2.3.	80
286			
287			
288			
289			
290			
291	Figure 44	The E/p distribution and ratio of simulation to data for isolated tracks with (a) $ \eta < 0.6$ and $1.2 < p/\text{GeV} < 1.8$ and (b) $ \eta < 0.6$ and $2.2 < p/\text{GeV} < 2.8$	80
292			
293			
294	Figure 45	The fraction of tracks as a function (a, b) of momentum, (c, d) of interaction lengths with $E \leq 0$ for tracks with positive (on the left) and negative (on the right) charge.	82
295			
296			
297			
298	Figure 46	$\langle E/p \rangle_{\text{BG}}$ as a function of the track momentum for tracks with (a) $ \eta < 0.6$, (b) $0.6 < \eta < 1.1$, and as a function of the track pseudorapidity for tracks with (c) $1.2 < p/\text{GeV} < 1.8$, (d) $1.8 < p/\text{GeV} < 2.2$	83
299			
300			
301			
302	Figure 47	$\langle E/p \rangle_{\text{COR}}$ as a function of track momentum, for tracks with (a) $ \eta < 0.6$, (b) $0.6 < \eta < 1.1$, (c) $1.8 < \eta < 1.9$, and (d) $1.9 < \eta < 2.3$	84
303			
304			
305	Figure 48	$\langle E/p \rangle_{\text{COR}}$ calculated using LCW-calibrated topological clusters as a function of track momentum for tracks with (a) zero or more associated topological clusters or (b) one or more associated topological clusters.	85
306			
307			
308			
309	Figure 49	Comparison of the $\langle E/p \rangle_{\text{COR}}$ for tracks with (a) less than and (b) greater than 20 hits in the TRT.	86
310			
311	Figure 50	Comparison of the $\langle E/p \rangle_{\text{COR}}$ for (a) positive and (b) negative tracks as a function of track momentum for tracks with $ \eta < 0.6$	86
312			
313			
314	Figure 51	Comparison of the E/p distributions for (a) positive and (b) negative tracks with $0.8 < p/\text{GeV} < 1.2$ and $ \eta < 0.6$, in simulation with the FTFP_BERT and QGSP_BERT physics lists.	87
315			
316			
317			
318	Figure 52	Comparison of the response of the hadronic calorimeter as a function of track momentum (a) at the EM-scale and (b) after the LCW calibration.	87
319			
320			
321	Figure 53	Comparison of the response of the EM calorimeter as a function of track momentum (a) at the EM-scale and (b) with the LCW calibration.	88
322			
323			
324	Figure 54	The reconstructed mass peaks of (a) K_S^0 , (b) Λ , and (c) $\bar{\Lambda}$ candidates.	89
325			
326	Figure 55	The E/p distribution for isolated (a) π^+ , (b) π^- , (c) proton, and (d) anti-proton tracks.	90
327			
328	Figure 56	The fraction of tracks with $E \leq 0$ for identified (a) π^+ and π^- , and (b) proton and anti-proton tracks	90
329			

330	Figure 57	The difference in $\langle E/p \rangle$ between (a) π^+ and π^- (b) p and π^+ , and (c) \bar{p} and π^-	91
331		$\langle E/p \rangle_{\text{COR}}$ as a function of track momentum for (a) π^+ tracks and (b) π^- tracks.	92
332	Figure 58		
333		The ratio of the calorimeter response to single particles of various species to the calorimeter response to π^+ with the physics list FTFP_BERT.	92
334	Figure 59		
335		The spectra of true particles inside anti- k_t , $R = 0.4$ jets with (a) $90 < p_T/\text{GeV} < 100$, (b) $400 < p_T/\text{GeV} < 500$, and (c) $1800 < p_T/\text{GeV} < 2300$	96
336			
337	Figure 60	The JES uncertainty contributions, as well as the total JES uncertainty, as a function of jet p_T for (a) $ \eta < 0.6$ and (b) $0.6 < \eta < 1.1$	98
338			
339		The JES correlations as a function of jet p_T and $ \eta $ for jets in the central region of the detector.	99
340	Figure 61		
341		A schematic diagram of an R-Hadron event with a lifetime around 0.01 ns. The diagram includes one charged R-Hadron (solid blue), one neutral R-Hadron (dashed blue), Lightest Supersymmetric Particles (LSPs) (dashed green) and charged hadrons (solid orange). The pixel detector, calorimeters, and muon system are illustrated but not to scale.	105
342			
343	Figure 62		
344			
345	Figure 63		
346			
347			
348			
349			
350			
351			
352	Figure 64		
353			
354			
355			
356			
357			
358	Figure 65		
359			
360			
361			
362			
363			
364	Figure 66		
365			
366			
367			
368			
369			
370	Figure 67		
371			
372			
373			
374			

375	Figure 68	The distribution of (a) E_T^{miss} and (b) Calorimeter E_T^{miss} for simulated signal events before the trigger requirement.	112
376			
377			
378	Figure 69	The distribution of E_T^{miss} for data and simulated signal events, after the trigger requirement.	114
379			
380	Figure 70	The trigger efficiency for the HLT_xe70 trigger requirement as a function of (a) E_T^{miss} and (b) Calorimeter E_T^{miss} for simulated signal events.	115
381			
382			
383	Figure 71	The dependence of dE/dx on N_{split} in data after basic track hit requirements have been applied.	116
384			
385	Figure 72	The distribution of dE/dx with various selections applied in data and simulated signal events.	116
386			
387	Figure 73	The distribution of track momentum for data and simulated signal events, after previous selection requirements have been applied.	117
388			
389			
390	Figure 74	The distribution of M_T for data and simulated signal events, after previous selection requirements have been applied.	118
391			
392			
393	Figure 75	The distribution of summed tracked momentum within a cone of $\Delta R < 0.25$ around the candidate track for data and simulated signal events, after previous selection requirements have been applied.	119
394			
395			
396			
397	Figure 76	The normalized, two-dimensional distribution of E/p and f_{EM} for simulated (a) $Z \rightarrow ee$, (b) $Z \rightarrow \tau\tau$, (c) 1200 GeV Stable R-Hadron events, and (d) 1200 GeV, 10 ns R-Hadron events.	120
398			
399			
400			
401	Figure 77	Two-dimensional distribution of dE/dx versus charge signed momentum (qp) for minimum-bias tracks. The fitted distributions of the most probable values for pions, kaons and protons are superimposed.	121
402			
403			
404			
405	Figure 78	The distribution of mass estimated using dE/dx for simulated stable R-Hadrons with masses between 1000 and 1600 GeV.	122
406			
407			
408	Figure 79	The acceptance \times efficiency as a function of R-Hadron (a) mass and (b) lifetime. (a) shows all of the combinations of mass and lifetime considered in this search, and (b) highlights the lifetime dependence for 1000 GeV and 1600 GeV R-Hadrons.	124
409			
410			
411			
412			
413	Figure 80	The distribution of (a) dE/dx and (b) momentum for tracks in data and simulated signal after requiring the event level selection and the track selection on p_T , hits, and N_{split} . Each sub-figure shows the normalized distributions for tracks classified as hadrons, electrons, and muons in data and R-Hadrons in the simulated signal.	126
414			
415			
416			
417			
418			
419			

420	Figure 81	The distribution of $M_{dE/dx}$ (a) before and (b) after the ionization requirement for tracks in simulated W boson decays and for the randomly generated background estimate.	128
421			
422			
423			
424	Figure 82	The distribution of $M_{dE/dx}$ (a) before and (b) after the ionization requirement for tracks in the validation region and for the randomly generated background estimate.	129
425			
426			
427			
428	Figure 83	The trigger efficiency for the HLT_xe70 trigger requirement as a function of Calorimeter E_T^{miss} for simulated data events with a W boson selection. Simulated signal events and simulated W boson events are also included.	134
429			
430			
431			
432			
433	Figure 84	The efficiency of the muon veto for R-hadrons of two different masses, as a function of $\frac{1}{\beta}$ for simulated R-Hadron tracks.	136
434			
435			
436	Figure 85	The average reconstructed MDT β distribution for $Z \rightarrow \mu\mu$ events in which one of the muons is reconstructed as a slow muon, for both data and simulation. A gaussian fit is superimposed.	137
437			
438			
439			
440	Figure 86	The observed mass distribution of events in data and the generated background distribution in (a) the stable and (b) the metastable signal region. A few example simulated signal distributions are superimposed.	138
441			
442			
443			
444	Figure 87	The observed and expected cross section limits as a function of mass for the stable simulated signal. The predicted cross section values for the corresponding signals are included.	141
445			
446			
447			
448	Figure 88	The observed and expected cross section limits as a function of mass for each generated lifetime. The predicted cross section values for the corresponding signals are included.	142
449			
450			
451			
452	Figure 89	The excluded range of masses as a function of gluino lifetime. The expected lower limit (LL), with its experimental $\pm 1\sigma$ band, is given with respect to the nominal theoretical cross-section. The observed 95% LL obtained at $\sqrt{s} = 8$ TeV [70] is also shown for comparison.	144
453			
454			
455			
456			
457	Figure 90	The constraints on the gluino mass as a function of lifetime for a split-supersymmetry model with the gluino R-Hadrons decaying into a gluon or light quarks and a neutralino with mass of 100 GeV. The solid lines indicate the observed limits, while the dashed lines indicate the expected limits. The area below the curves is excluded. The dots represent results for which the particle is assumed to be prompt or stable.	145
458			
459			
460			
461			
462			
463			
464			

465 LIST OF TABLES

466 Table 1	The particles in the SM and their corresponding super-
467	partners in the Minimal Supersymmetric Model (MSSM). 22
468 Table 2	The design parameters of the LHC beam that deter-
469	mines the energy of collisions and the luminosity, for
470	both the injection of protons and at the nominal cir-
471	culation. 34
472 Table 3	The performance goals for each of the subsystems of
473	the ATLAS detector. The $ \eta $ coverage specifies the range
474	where the subsystem needs to be able to provide mea-
475	surements with the specified resolution. The resolu-
476	tions include a p_T or E dependence that is added in
477	quadrature with a p_T/E independent piece. 39
478 Table 4	A summary of the parameters of each of the three mag-
479	net systems on ATLAS 41
480 Table 5	A summary of the parameters of the inner detector
481	and each of the subdetectors [5]. 46
482 Table 6	A summary of the expected performance of the com-
483	bined inner detector [10]. Included are the reconstruc-
484	tion efficiencies for multiple particle types as well as the
485	momentum and impact parameter (IP) resolution for
486	various momenta. 47
487 Table 7	The trigger menu for the 2015 data collection with
488	$L = 5 \times 10^{33} \text{ cm}^{-2} \text{ s}^{-1}$. Both the L1 and high level trig-
489	ger (HLT) selection requirements and their trigger rates
490	are shown measured at the specified luminosity are
491	shown. The typical offline selections represent a typi-
492	cal set of offline requirements imposed after the trig-
493	ger in an analysis. 61
494 Table 8	The dominant sources of corrections and systematic
495	uncertainties in the JES estimation technique, includ-
496	ing typical values for the correcting shift (Δ) and the
497	associated uncertainty (σ). 97
498 Table 9	The expected number of events at each level of the se-
499	lection for metastable 1600 GeV, 10 ns R-Hadrons,
500	along with the number of events observed in data, for
501	3.2 fb^{-1} . The simulated yields are shown with statis-
502	tical uncertainties only. The total efficiency \times accep-
503	tance is also shown for the signal. 123

504	Table 10	A summary of the sources of systematic uncertainty for the data-driven background in the signal region. If the uncertainty depends on the mass, the maximum values are reported.	131
505			
506			
507			
508	Table 11	A summary of the sources of systematic uncertainty for the simulated signal yield. The uncertainty depends on the mass and lifetime, and the maximum negative and positive values are reported in the table.	133
509			
510			
511			
512	Table 12	Example of the contributing systematic variations to the total systematic for the E_T^{miss} Scale, as measured in a 1200 GeV, Stable R-Hadron signal sample.	135
513			
514			
515	Table 13	The estimated number of background events and the number of observed events in data for the specified selection regions prior to the requirement on mass. The background estimates show statistical and systematic uncertainties.	138
516			
517			
518			
519			
520	Table 14	The left and right extremum of the mass window for each generated mass point with a 10 ns lifetime.	139
521			
522	Table 15	The left and right extremum of the mass window used for each generated stable mass point.	139
523			
524	Table 16	The expected number of signal events, the expected number of background events, and the observed number of events in data with their respective statistical errors within the respective mass window for each generated stable mass point	140
525			
526			
527			
528			
529	Table 17	The expected number of signal events, the expected number of background events, and the observed number of events in data with their respective statistical errors within the respective mass window for each generated mass point with a lifetime of 10 ns.	140
530			
531			
532			
533			
534	Table 18	The observed and expected 95% CL lower limit on mass for gluino R-Hadrons for each considered lifetime.	143
535			
536	Table 19	The left and right extremum of the mass window for each generated mass point with a 50 ns lifetime.	155
537			
538	Table 20	The left and right extremum of the mass window for each generated mass point with a 30 ns lifetime.	155
539			
540	Table 21	The left and right extremum of the mass window for each generated mass point with a 10 ns lifetime.	156
541			
542	Table 22	The left and right extremum of the mass window used for each generated mass point with a lifetime of 3 ns.	156
543			
544	Table 23	The left and right extremum of the mass window used for each mass point with a lifetime of 1 ns.	156
545			
546	Table 24	The left and right extremum of the mass window for each generated mass point with a lifetime of 0.4 ns.	157
547			
548	Table 25	The left and right extremum of the mass window used for each generated stable mass point.	157
549			

550	Table 26	The expected number of signal events, the expected number of background events, and the observed number of events in data with their respective statistical errors within the respective mass window for each generated mass point with a lifetime of 50 ns.	157
551			
552			
553			
554			
555	Table 27	The expected number of signal events, the expected number of background events, and the observed number of events in data with their respective statistical errors within the respective mass window for each generated mass point with a lifetime of 30 ns.	158
556			
557			
558			
559			
560	Table 28	The expected number of signal events, the expected number of background events, and the observed number of events in data with their respective statistical errors within the respective mass window for each generated mass point with a lifetime of 10 ns.	158
561			
562			
563			
564			
565	Table 29	The expected number of signal events, the expected number of background events, and the observed number of events in data with their respective statistical errors within the respective mass window for each generated mass point with a lifetime of 3 ns.	159
566			
567			
568			
569			
570	Table 30	The expected number of signal events, the expected number of background events, and the observed number of events in data with their respective statistical errors within the respective mass window for each generated mass point with a lifetime of 1 ns.	159
571			
572			
573			
574			
575	Table 31	The expected number of signal events, the expected number of background events, and the observed number of events in data with their respective statistical errors within the respective mass window for each generated mass point with a lifetime of p4 ns.	160
576			
577			
578			
579			
580	Table 32	The expected number of signal events, the expected number of background events, and the observed number of events in data with their respective statistical errors within the respective mass window for each generated stable mass point	160
581			
582			
583			
584			

586 ACRONYMS

- 587 SM Standard Model
588 CERN European Organization for Nuclear Research
589 SUSY Supersymmetry
590 LSP Lightest Supersymmetric Particle
591 LHC Large Hadron Collider
592 ATLAS A Toroidal LHC ApparatuS
593 CMS Compact Muon Solenoid
594 ALICE A Large Ion Collider Experiment
595 LHCb Large Hadron Collider beauty experiment
596 LEP the Large Electron Positron collider
597 PS Proton Synchrotron
598 PSB Proton Synchrotron Booster
599 SPS Super Proton Synchrotron
600 SCT silicon microstrip
601 TRT transition radiation tracker
602 LAr Liquid Argon
603 EM electromagnetic
604 RPC Resistive Plate Chamber
605 TGC Thin Gap Chamber
606 MDT Monitored Drift Tube
607 CSC Cathode Strip Chamber
608 ToT time over threshold
609 RoI Region of Interest
610 LCW local cluster weighted
611 MIP minimally ionizing particle
612 IP impact parameter

- 613 EPJC European Physical Journal C
614 JES jet energy scale
615 LLP Long-Lived Particle
616 CR Control Region
617 NLO next-to-leading order
618 NLL next-to-leading logarithmic
619 PDF parton distribution function
620 ISR initial state radiation
621 RMS root mean square
622 IBL Insertible B-Layer
623 CP Combined Performance
624 MDT Monitored Drift Tube
625 RF radiofrequency
626 HLT high level trigger
627 QCD quantum chromodynamics
628 BSM beyond the Standard Model
629 MSSM Minimal Supersymmetric Model

630

PART I

631

INTRODUCTION

632

You can put some informational part preamble text here.

1

633

634 INTRODUCTION

635

PART II

636

THEORETICAL CONTEXT

637

You can put some informational part preamble text here.

2

638

639 STANDARD MODEL

640 The SM of particle physics seeks to explain the symmetries and interactions of
641 fundamental particles. The SM provides predictions in particle physics for in-
642 teractions up to the Planck scale (10^{15} - 10^{19} GeV). It has been tested by several
643 generations of experiments and has been remarkably successful; no significant
644 deviations from its predictions have been found.

645 The theory itself is a quantum field theory grown from an underlying sym-
646 metry, $SU(3) \times SU(2) \times U(1)$, that generates all of the interactions consistent
647 with experimental observations. These interactions are referred to as the Strong,
648 Weak, and Electromagnetic forces. Each postulated symmetry necessitates the
649 existence of an associated conserved charge, which appear as properties of the
650 observed particles in nature.

651 Although this model has been very predictive, the theory is incomplete; for
652 example, it is not able to describe gravity or astronomically observed dark mat-
653 ter. These limitations suggest a need for an extension or new theory to describe
654 physics at higher energies.

655 2.1 ACTION AND THE LAGRANGIAN

Originally, both action and the Lagrangian were constructed for an integral reformulation of the laws of classical mechanics, which is a purely mathematical step: any differential equation can be re-expressed in terms of an integral equation. The Lagrangian, \mathcal{L} , is classically given by the difference of kinetic energy and potential energy. The Lagrangian is defined this way so that the action, \mathcal{S} , given by

$$\mathcal{S}[\mathbf{q}(t)] = \int_{t_1}^{t_2} \mathcal{L}(\mathbf{q}, \dot{\mathbf{q}}, t) dt \quad (1)$$

656 returns the classical equations of motion when one requires it to be stationary
657 in the path, $\mathbf{q}(t)$. This formulation of classical mechanics is extremely useful in
658 calculations, and generalizes beautifully to cover all types of physics.

659 In particular, with the development of quantum mechanics in the twentieth
660 century, the concepts of action and the Lagrangian were found to generalize to
661 more complicated physics for which the classical laws do not hold. Quantum
662 mechanics and quantum field theory can be constructed from the action, using
663 the path integral formulation, by assuming that a particle undergoes all possible
664 paths $\mathbf{q}(t)$ with an imaginary phase given by $e^{i\mathcal{S}[\mathbf{q}(t)]/\hbar}$. This reduces to classical
665 mechanics in the limit as \hbar goes to zero, as all paths for which the action is not
666 stationary interfere with each other so as to cancel their contributions. Because
667 the wavefunction of a particle can be completely determined through the action

668 and the action depends only on the Lagrangian, the Lagrangian itself is sufficient
 669 to describe the physics governing the particle.

670 So, in both classical and quantum mechanics, the Lagrangian of a system con-
 671 tains everything there is to know about the system, apart from initial conditions.
 672 Thus, the most natural way to express that a system has a certain symmetry is to
 673 require that the Lagrangian is invariant under a corresponding symmetry trans-
 674 formation. This makes the Lagrangian the central piece of the discussion of
 675 gauge invariance; the mathematical representation of gauge invariance is that a
 676 gauge transformation on the appropriate components of the Lagrangian returns
 677 an identical Lagrangian. That is,

$$\mathcal{L}(\psi, D^\mu) = \mathcal{L}(U\psi, D'^\mu) \quad (2)$$

678 where ψ is the wavefunction and D^μ is the covariant derivative, both of which
 679 transform under a symmetry operation. There are a number of immediate and
 680 surprisingly powerful consequences of requiring that the Lagrangian is invariant
 681 under a symmetry operation.

682 2.2 GAUGE INVARIANCE AND FORCES

683 The simplest possible relativistic, quantum Lagrangian is the free Dirac Lagrangian,
 684 which describes a relativistic fermion in a vacuum.

$$\mathcal{L} = i\bar{\psi}\not{d}\psi - m\bar{\psi}\psi \quad (3)$$

685 A fermion denotes a particle with spin-1/2, and the kinematic term is chosen to
 686 correctly describe the free propagation of a fermionic particle with mass m . This
 687 equation is clearly invariant under a global $U(1)$ transformation, that is chang-
 688 ing ψ by a complex phase has no effect. The derivative operator commutes with
 689 a constant phase factor, and wherever ψ appears its complex conjugate also ap-
 690 pears so as to cancel out the change of phase. However, the Lagrangian as written
 691 is not invariant under the local $U(1)$ symmetry postulated for the SM, which can
 692 be written as $U = e^{ia(x)}$. The piece of the Lagrangian involving a derivative will
 693 return an extra term that will break the invariance of the Lagrangian under this
 694 transformation:

$$\begin{aligned} \mathcal{L}' &= i(\bar{\psi}U^\dagger)\not{d}(U\psi) - m(\bar{\psi}U^\dagger)(U\psi) \\ &= i(\bar{\psi}U^\dagger)U(\not{d} - \gamma^\mu\partial_\mu\alpha(x))\psi - m(\bar{\psi}U^\dagger)(U\psi) \\ &= i\bar{\psi}\not{d}\psi - m\bar{\psi}\psi - i\gamma^\mu\partial_\mu\alpha(x)\bar{\psi}\psi \\ &= \mathcal{L} - i\gamma^\mu\partial_\mu\alpha(x)\bar{\psi}\psi \\ &\neq \mathcal{L} \end{aligned}$$

695 So, in order to enforce the required symmetry, the typical approach is to con-
 696 struct a covariant derivative, that is to add a term to the derivative operator

so that the unwanted term in \mathcal{L}' is exactly canceled. A generic form for such a derivative is given by

$$D^\mu = \partial^\mu - iqA^\mu$$

where at this point A^μ is an arbitrary field that transforms under the $U(1)$ operator and q is a scaling factor. Adding this component to the above Lagrangian gives

$$\mathcal{L}' = i(\bar{\psi}U^\dagger)U(\not{d} - \gamma^\mu\partial_\mu\alpha(x) - iq\gamma^\mu A'_\mu)\psi - m(\bar{\psi}U^\dagger)(U\psi) \quad (4)$$

$$\mathcal{L}' = \mathcal{L} + \gamma^\mu(-i\partial_\mu\alpha(x) - iqA'_\mu + iqA_\mu)\bar{\psi}\psi \quad (5)$$

and because the transformation of A^μ is unspecified, $\mathcal{L} = \mathcal{L}'$ whenever

$$A'_\mu = A_\mu - \frac{1}{q}\partial_\mu\alpha(x)$$

The above procedure demonstrated that beginning with the Lagrangian for a free fermion and imposing a local $U(1)$ symmetry required the existence of a vector field A^μ , and specified its transformation under the $U(1)$ gauge group. The additional term in the derivative can be expanded to form a completely separate term in the Lagrangian,

$$\mathcal{L} = i\bar{\psi}\not{d}\psi - m\bar{\psi}\psi - (q\bar{\psi}\gamma^\mu\psi)A^\mu \quad (6)$$

and in this form it is clear that the A^μ term has the exact form of the electromagnetic interaction. That is, this is the Lagrangian which reproduces the relativistic form of Maxwell's equations for a particle interacting with an electromagnetic field. It is natural to also introduce a term to the Lagrangian at this point to describe the free propagation of the vector A field, where the propagation of a vector field has the form of

$$-\frac{1}{16\pi}F^{\mu\nu}F_{\mu\nu} \quad \text{with} \quad F_{\mu\nu} = \partial_\mu A_\nu - \partial_\nu A_\mu \quad (7)$$

This then also describes the electromagnetic interactions in a vacuum and the propagation of a photon. The photon is an example of a gauge boson, a spin-0 particle required to exist by a gauge symmetry of the Lagrangian and one that corresponds to a force. In summary, requiring the $U(1)$ symmetry was enough to recover all of electromagnetism and to predict the existence of a photon in the SM.

The interaction term that was placed into the Lagrangian by this procedure can be conveniently summarized with Feynman diagrams, which diagrammatically represent a transition from an initial state to a final state. All diagrams that start with the same initial state and end with the same final state must be considered, but more complicated diagrams can be built by linking together the simplest versions. A diagram that corresponds to the above term, $(q\bar{\psi}\gamma^\mu\psi)A^\mu$, is shown in Figure 1, for an interaction with a generic fermion.

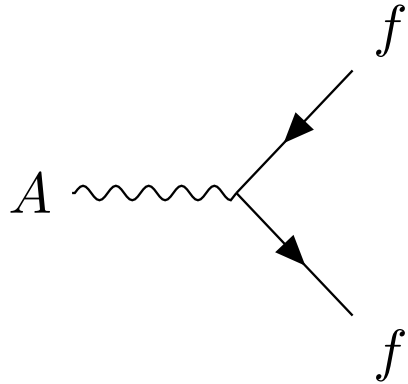


Figure 1: A Feynman diagram representing the interaction of the A field with a generic fermion, f .

727 2.2.1 $SU(2) \times U(1)$ AND THE ELECTROWEAK FORCE

728 The full picture of the electroweak section of the SM is more complicated than the
729 simplified explanation of the electromagnetic piece described above. In practice,
730 it is necessary to consider the entire $SU(2) \times U(1)$ symmetry together, but the
731 procedure is the same. Enforcing the symmetry on the Lagrangian requires the
732 introduction of a covariant derivative, this time with four total distinct terms,
733 one for each of the generators of $SU(2) \times U(1)$. The result is a series of terms
734 in the Lagrangian which describe the interaction of a fermion with four vector
735 fields, the W_1 , W_2 , W_3 , and B fields. These fields can mix in the quantum sense,
736 and linear combinations form the W^+ , W^- , Z , and A fields that are considered
737 actual particles in the SM¹.

738 2.2.2 $SU(3)$ AND THE STRONG FORCE

739 The same procedure can be applied starting with the $SU(3)$ symmetry require-
740 ment, where eight additional fields must be introduced, one for each of the gen-
741 erators of $SU(3)$. The resulting Lagrangian describes quantum chromodynam-
742 ics (QCD) and predicts the existence of eight gauge bosons known collectively as
743 gluons.

744 2.3 NOETHER'S THEOREM, CHARGES, AND MATTER

745 Another direct consequence of the symmetries stipulated in the SM are a series
746 of conserved quantities, Noether charges, named after the mathematician and
747 physicist Emmy Noether. The charges arise as a direct consequence of Noether's
748 theorem, which can be informally stated as

1 These states are the actual particles because they are mass eigenstates, but the full explanation of this will have to wait for the discussion of the Higgs mechanism.

749 *For every symmetry of the Lagrangian, there exists a corresponding phys-*
 750 *ical quantity whose value is conserved in time.*

751 Or, stated another way, symmetries of the Lagrangian mathematically require
 752 the conservation of specific quantities taken from the Lagrangian. This rela-
 753 tionship can also be thought of as operating in the other direction, the exis-
 754 tence of a conserved charge can be shown to generate the symmetry in the La-
 755 grangian. This theorem is actually quite striking in a somewhat unexpected re-
 756 lation between simple geometric symmetries and physically observable conser-
 757 vation laws. For example, the theorem connects the translation invariance of
 758 the Lagrangian in space to the conservation of momentum and the translation
 759 invariance in time to the conservation of energy.

760 In the context of the SM, the required symmetries of $U(1) \times SU(2) \times SU(3)$
 761 correspond to the charges that are considered properties of all elementary par-
 762 ticles. The most familiar of these properties is the electric charge, Q , which is
 763 one of the conserved quantities of $SU(2) \times U(1)$. The remaining pieces of
 764 $SU(2) \times U(1)$ correspond to weak isospin, T and T_3 , where T has only non-
 765 negative values and T_3 can be positive and negative. The $SU(3)$ symmetry is
 766 generated by the three colors of QCD, red, green, and blue, each with a corre-
 767 sponding opposite color, anti-red, anti-green, and anti-blue.

768 The matter in the observable universe consists of a collection of particles which
 769 carry these charges, in addition to spin and mass. The particles typically thought
 770 of as matter are all fermions: particles with spin-1/2. All of the fermions belong
 771 to one of two groups, quarks and leptons, and one of three generations. Each
 772 of the generations have similar properties but significantly different masses; the
 773 particles in consecutive generations have increasing mass. Quarks are distin-
 774 guished from leptons in that they carry color charge, in addition to electric charge
 775 and weak isospin. The particles in the SM are summarized in Figure 2, and the
 776 matter particles are the twelve types of fermions displayed on the left side of the
 777 graphic.

778 2.3.1 QUARKS

779 The three generations of quarks each have a particle with electric charge +2/3
 780 and one with charge -1/3. They are referred to us up and down, charm and
 781 strange, and top and bottom respectively, and these are referred to as the quark
 782 flavors. Although Figure 2 only shows these six flavors, there is a unique particle
 783 for each combination of the three colors and flavor. And each quark has an anti-
 784 particle with the opposite electric and color charge values.

785 However, individual quarks are never observed in nature, but instead form
 786 color-neutral bound states. One way to form a color neutral combination is a
 787 bound state of three quarks with three different color charges, called a baryon.
 788 Baryons are the most common type of quark configuration in conventional mat-
 789 ter, and include protons and neutrons. The other common configuration is a
 790 bound state of a quark and an anti-quark, called a meson, where the two quarks
 791 have the same type but opposite colors. The conservation of the various charges
 792 carried by quarks, along with the requirement that quarks appear in color-neutral

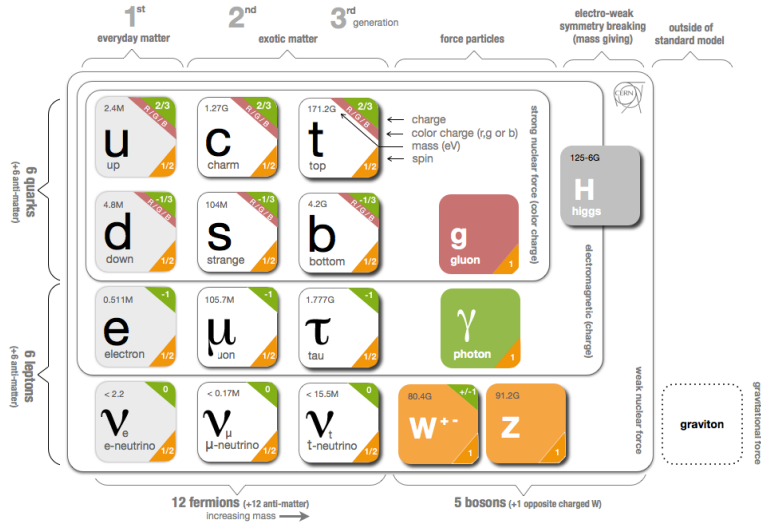


Figure 2: The particle content of the SM.

793 states, result in the observed conservation of baryon number, B , where baryons
 794 have $B = 1$ and mesons have $B = 0$.

795 2.3.2 LEPTONS

796 The remaining fermions, the leptons, do not carry color charge. Each generation
 797 contains an electrically charged lepton, the electron, muon, and tau, and an elec-
 798 trically neutral lepton called a neutrino. For the charged leptons, the flavors are
 799 mass eigenstates, with the masses listed in Figure 2. The flavors of the neutrinos,
 800 on the other hand, are not mass eigenstates: they propagate in mass eigenstates
 801 and so can oscillate between different flavors. The absolute masses of the neu-
 802 trinos are not currently known, but the phenomenon of oscillations shows that
 803 they have three different mass values. Although there is no direct conservation
 804 law resulting from the symmetries of the SM Lagrangian, no interactions have
 805 been observed which alter lepton number, L , the difference in the number of lep-
 806 tons and anti-leptons.

807 2.3.3 CHIRALITY

808 All of the fermions described above have two possible values of the magnitude
 809 of weak isospin, T , either 0 or 1/2. The fermions with $T = 0$ are called right-
 810 handed, while those with $T = 1/2$ are called left-handed. For left-handed fermions,
 811 each of the quark and lepton generations have one particle with $T_3 = -1/2$ and
 812 one with $T_3 = +1/2$. The neutrinos have $T_3 = +1/2$, while the charged leptons
 813 have $T_3 = -1/2$. Similarly, the positively charged quarks have $T_3 = +1/2$ and the
 814 negatively charged quarks have $T_3 = -1/2$. Because the right-handed neutrinos
 815 would have no charge of any type, it is not clear if they exist at all.

816 2.4 HIGGS MECHANISM AND MASS

817 The description of the electroweak forces above left out an important part of the
 818 observed nature of the electroweak force. Many physical experiments observed
 819 phenomena corresponding to the interaction of the weak bosons that were best
 820 explained if they had significant masses. A large mass for the W and Z bosons
 821 would explain the relative weakness of their interactions compared to the elec-
 822 tromagnetic field. The Lagrangian's discussed above did not include a mass term
 823 for the gauge bosons, and in fact such a term would not be allowed by the require-
 824 ment of gauge invariance. This was a significant problem for the SM, and the
 825 symmetry of the electroweak sector would have to be broken in order to allow
 826 for non zero masses for some of the gauge bosons.

827 One mechanism to allow for this spontaneous symmetry breaking is the Higgs
 828 mechanism, which posits the existence of an additional scalar field. It begins
 829 with a $SU(2) \times U(1)$ invariant Lagrangian of the form

$$\mathcal{L} = |D_\mu \phi|^2 - \frac{1}{2}\mu^2\phi^+\phi - \frac{1}{4}\lambda(\phi^+\phi)^2 \quad (8)$$

830 where ϕ is the new scalar field and, importantly, μ^2 is negative. This leads to a
 831 minimum value of the field at a non-zero value of ϕ , specifically where

$$\langle \phi \rangle = \frac{1}{\sqrt{2}} \begin{pmatrix} 0 \\ v \end{pmatrix} \quad \text{with} \quad v = \frac{2\mu^2}{\lambda} \quad (9)$$

832 Expanding the original Lagrangian about its expectation value,

$$\langle \phi \rangle = \frac{1}{\sqrt{2}} \begin{pmatrix} 0 \\ v + H \end{pmatrix} \quad (10)$$

833 gives potential terms in the Lagrangian like

$$\mathcal{L}_H = -\frac{1}{2}m_H^2H^2 - \sqrt{\frac{\lambda}{2}}m_HH^3 - \frac{1}{4}\lambda H^4 \quad (11)$$

834 where $m_H = \sqrt{2}\mu$. The form of this Lagrangian shows that the non-zero ex-
 835 pectation value of the ϕ field has introduced a massive scalar field H with self
 836 interaction terms. It has an additional important consequence on the description
 837 of the gauge bosons, through the expansion of the term involving the covariant
 838 derivative:

$$|D_\mu \phi|^2 \supset \frac{1}{8} (g^2(W_{1\mu}W_1^\mu + W_{2\mu}W_2^\mu) + (g'B_\mu - gW_3\mu)^2) \quad (12)$$

839 where the W_i and B fields are the original $SU(2) \times U(1)$ gauge fields men-
 840 tioned previously. The above equation can be rearranged using linear combina-
 841 tions of the fields to from mass terms for the gauge bosons, and the mass eigen-
 842 states are exactly the W^\pm , Z , and A fields. Only the A field, corresponding to

843 the photon, results in a zero mass, and the remaining three fields acquire masses.
 844 Because the originally introduced Lagrangian, written in terms of ϕ , was clearly
 845 gauge invariant, this resulting configuration must also be gauge invariant.

846 This is the Higgs mechanism, where the introduction of a gauge invariant
 847 scalar field with a non-zero expectation value can generate masses for the gauge
 848 bosons without violating the underlying symmetries. The particle that is asso-
 849 ciated with the perturbations of this field, H , is called the Higgs boson, and is
 850 said to generate the masses of the remaining bosons. The resulting masses are
 851 listed in Figure 2. Because this mechanism was so successful in describing the
 852 observed properties of the W and Z bosons, it has been considered part of the
 853 SM for decades, although the actual Higgs boson was only recently observed in
 854 2012, confirming the theory.

855 The Higgs mechanism is also responsible for generating the masses of the
 856 fermions. The original mass terms that were listed in the Lagrangian for fermions
 857 are replaced with Yukawa coupling terms, which introduce interactions between
 858 the ϕ field and the fermions. Like with the gauge bosons, the non-zero expec-
 859 tation value of the field yields mass terms, and the expansion about that value
 860 introduces interaction terms between the fermions and the Higgs boson. The
 861 masses are different between each fermion because each has a different Yukawa
 862 coupling, which results in the masses listed in Figure 2.

863 2.5 PHENOMENOLOGY

864 The SM Lagrangian described above contains all of the information necessary
 865 to describe particle physics through the path integral formulation. However, a
 866 tremendous amount of complexity emerges from that description because of the
 867 diverse allowed interactions between the ensemble of particles in the SM. A qual-
 868 itative understanding of the phenomenology produced by those interactions is
 869 immensely helpful in understanding the analysis of particle physics.

870 2.5.1 ELECTROWEAK PHYSICS

871 The masses of the W and Z bosons result in significantly different processes
 872 for the weak fields than the electromagnetic field, despite their interactions be-
 873 ing similar before symmetry breaking. The massless photon is stable, and can
 874 propagate in a vacuum, resulting in the familiar long range interactions of elec-
 875 tromagnetism. The W and Z bosons, however, are unstable, as they have large
 876 enough masses to decay to fermions, such as the decays shown in Figure 3. For
 877 this reason, photons can be observed directly, while the other bosons are suffi-
 878 ciently short-lived that they can only be measured from their decay products.

879 Because the W and Z bosons interact with both quarks and leptons, they are
 880 responsible for the production of leptons in proton-proton collisions. Z bosons
 881 produce pairs of opposite sign, same flavor leptons. W bosons, on the other hand,
 882 produce a single lepton and the corresponding neutrino.

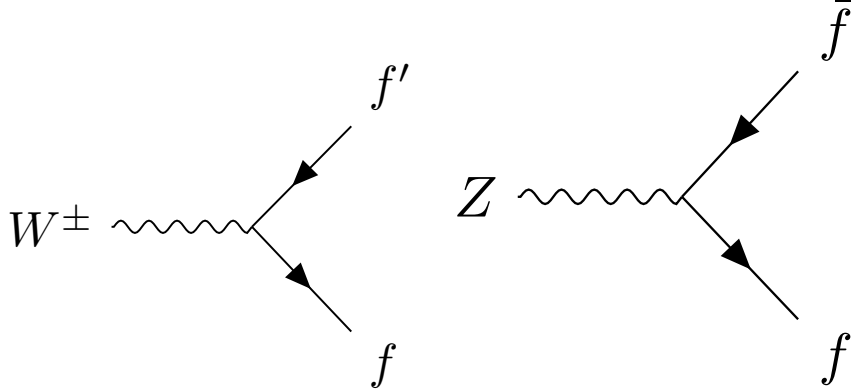


Figure 3: The Feynman diagrams representing the decays of the W and Z bosons to fermions. Here f indicates a generic fermion, \bar{f} its antiparticle, and f' the partner of that fermion in the same generation.

883 2.5.2 STRONG PHYSICS

884 The phenomenology of the strong sector differs significantly from the weak sec-
 885 tor because the gluons are massless but color charged. Because of this, gluons
 886 can interact with each other, and contributions from multiple gluon interactions
 887 lead to a significant growth in the strength of the field at low energies. The depen-
 888 dence of the field strength on the energy scale is described by renormalization,
 889 and in QCD the coupling is only small at high energies. Above around the GeV
 890 scale, the interactions of quarks become perturbative, similar to the electroweak
 891 fields; this phenomenon is known as asymptotic freedom.

892 At lower energies, however, the strength of the strong interaction is so signif-
 893 icant that the interactions of color-charged particles create additional particles
 894 until they form neutral bound-states. This process is known as hadronization,
 895 and explains why no quarks are observed isolated in nature: they all form bound
 896 states of hadrons like protons, neutrons, and pions. The hadronization process
 897 can produce a significant number of particles, so that a single energetic quark
 898 recoiling against another quark can generate a cascade of dozens of hadrons.
 899 Because of the initial boost of such an energetic configuration, the resulting
 900 hadrons are collimated, and conical spray of particles often referred to as a jet.

901 2.5.3 PROTON-PROTON COLLISIONS

902 Proton-proton collisions are a convenient way to generate high energy interac-
 903 tions to probe the SM and to search for new physics. At the energies that will be
 904 discussed in this analysis, the substructure of the protons is very important to the
 905 description of the resulting interactions. At lowest order, protons are composed
 906 of two up quarks and one down quark, but this description is incomplete. The
 907 actual bound state includes a chaotic sea of additional quarks and gluons, each of
 908 which carries a variable fraction of the proton's energy. When a proton-proton

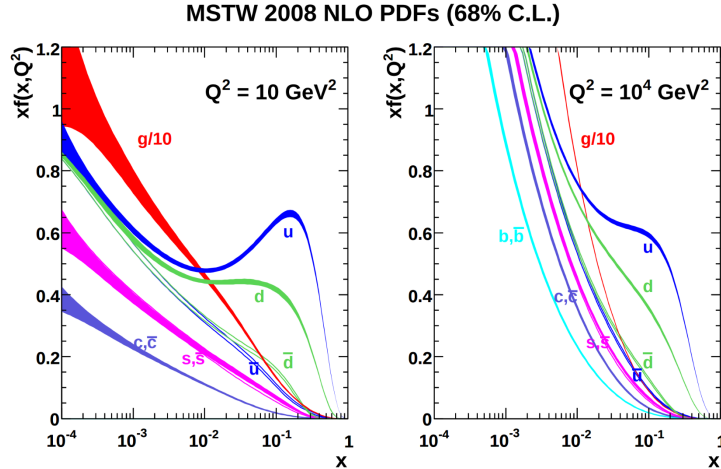


Figure 4: The PDFs for proton-proton collisions at $Q^2 = 10 \text{ GeV}^2$ and $Q^2 = 10^4 \text{ GeV}^2$. Each shows the fraction of particles which carry a fraction x of the total proton energy at the specified scale [1].

909 collision takes place, it is these constituents that interact with each other, resulting
 910 in a highly variable collision energy even when the proton-proton energy is
 911 consistent.

912 The fraction of the energy carried by each constituent varies moment to moment,
 913 but can be modelled probabilistically by PDFs. These are difficult to predict
 914 theoretically, as the QCD calculations are extremely complex, and instead
 915 are measured in hard-scattering experiments. They are usually represented by
 916 how often a given type of particle carries a fraction x of the total proton energy.
 917 Those fraction change significantly with the scale of the interaction; the PDFs of
 918 proton-proton collisions at both $Q^2 = 10 \text{ GeV}^2$ and $Q^2 = 10^4 \text{ GeV}^2$ are shown
 919 in Figure 4.

920 26 LIMITATIONS

921 Despite the great success of the relatively simple SM in describing such a broad
 922 range of emergent phenomena, it is clear that the picture it presents of the interactions
 923 of fundamental particles is incomplete. The SM contains concerning
 924 coincidences that suggest a more ordered underlying substructure that is not ex-
 925 pressed in the current form. It also fails to explain a number of cosmological
 926 measurements of the nature of matter in the universe. These limitations suggest
 927 the need for new, beyond the Standard Model (BSM) physics that would provide
 928 a more complete description at higher energies.

929 2.6.1 THEORETICAL CONCERNS

930 There have been no successful integrations of the SM's description of the elec-
 931 troweak and strong forces with the description of gravity, and it is still unclear
 932 how to account for the effects of gravity at the Plank scale of approximately 10^{19}

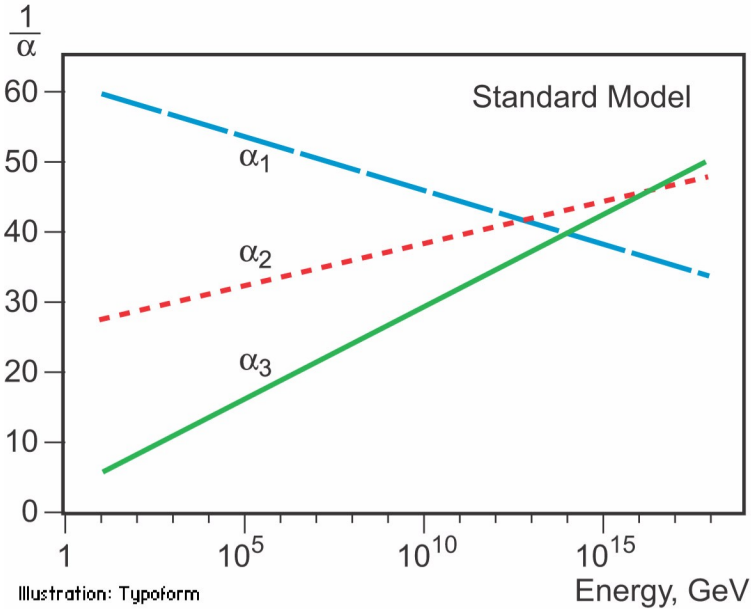


Figure 5: An approximation of the running of the coupling constants in the SM up to the Planck scale [unification_plot].

933 GeV, where it can no longer be ignored. The Plank scale is an important cutoff
 934 for the SM, as it is clear that the SM must break down somewhere between the
 935 current highest energy tests of the SM, around 1 TeV, and the Plank scale.

936 One example of this is the Higgs mass, which is determined in the SM by a
 937 sum of its bare mass and the interactions in the vacuum with all massive parti-
 938 cles. As their must be new physics at the Plank scale to describe gravity, some
 939 of those corrections would include contributions at a scale seventeen orders of
 940 magnitude above the mass of the Higgs. Either the bare mass of the Higgs boson
 941 precisely cancels those contributions to leave a remainder seventeen orders of
 942 magnitudes smaller, or a new theory exists at a lower scale the shields the Higgs
 943 mass from those terms. A theory where such a unlikely cancellation of free pa-
 944 rameters occurs is called fine-tuned, and one that is free from such cancellations
 945 is called natural. Theories where the mass of the Higgs is natural are usually
 946 preferred, as the suggest an underlying coherent structure.

947 There is also a compelling argument that the $SU(3) \times SU(2) \times U(1)$ gauge
 948 structure of the SM might originate from a single, unified gauge theory. For ex-
 949 ample, it is possible to represent that gauge structure as a $SU(5)$ gauge group
 950 with only a few inconsistencies with the current implementation. This unifica-
 951 tion is suggested by the scaling of the coupling constants for each of the forces
 952 under renormalization, they come close to converging to a single value at higher
 953 energies, as seen in Figure 5. An additional correction to the scaling of the cou-
 954 pling constants from new physics above the TeV scale could cause them to merge
 955 into a single value at high energies.

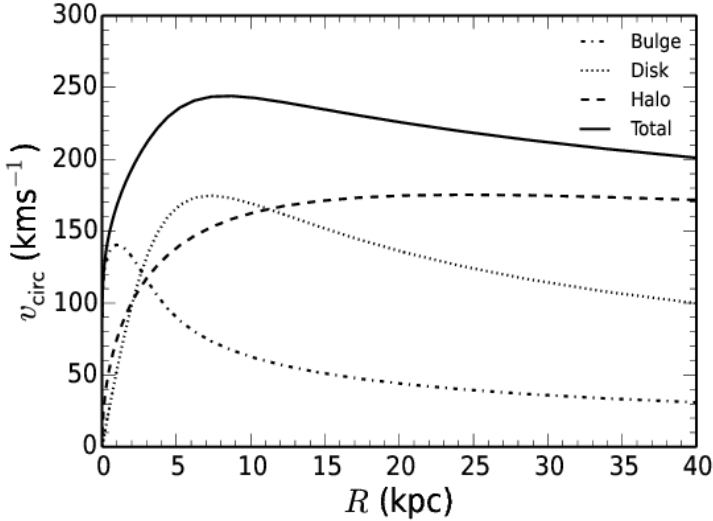


Figure 6: The distribution of velocities of stars as a function of the radius from the center of the galaxy. The contributions to the velocity from the various components of matter in the galaxy are shown [2].

956 2.6.2 COSMOLOGICAL OBSERVATIONS

957 The SM contains a symmetry in the description of matter and antimatter that is
 958 not reflected in cosmological observations. The process of the standard model
 959 create or remove matter and antimatter in equal amounts, so a universe that be-
 960 gins with an equal quantity of each should result in a universe with an approxi-
 961 mate balance of matter and antimatter. However, cosmological observations of
 962 the relative amount of each type clearly show that the directly observable mass
 963 of the universe is overwhelmingly made of matter. As this difference is largely
 964 a difference in the generation of baryons and anti-baryons, this discrepancy is
 965 often referred to as the baryogenesis problem.

966 A number of astrophysical observations of large scale gravitational interac-
 967 tions suggest the presence of a significant amount of non-luminous matter that
 968 interacts with the normal matter only gravitationally. The first evidence of this
 969 came from the observation of galactic rotation curves, the velocities of stars as
 970 a function of the radius from the center of a galaxy. These can be directly pre-
 971 dicted from the amount of matter contained within the sphere up to the radius
 972 of the star. An estimate based only on the luminous matter in the galaxies would
 973 predict a dependence that falls off with the radius, but the observed curves show
 974 a mostly constant distribution of velocities [2], as seen in Figure 6. The higher
 975 velocities than predicted by the luminous matter can be explained by a halo of
 976 dark matter that extends significantly outside the galactic disk.

977 This dark matter accounts for a majority of the matter in the universe, and is
 978 incompatible with the matter particles predicted by the SM. Many observations
 979 support its existence, but there have been no direct detections of a particle which
 980 could account for the large quantity of gravitationally interacting dark matter.
 981 The SM would have to require a significant extension to include the particles

982 needed to explain dark matter and the processes needed to explain the observed
983 matter-antimatter asymmetry.

984

985 SUPERSYMMETRY

986 The theory of Supersymmetry (**SUSY**) presents an extension to the **SM** that solves
 987 a number of the outstanding issues. It is based on another proposed symmetry,
 988 one which introduces an equality between the fermionic particles and proposed
 989 bosonic partners. The symmetry is defined by extended spacetime into a super-
 990 space, which includes on dimension that describes a particle's spin: a transfor-
 991 mation in this spacetime moves a fermion with spin-1/2 to a boson with spin-0 or
 992 vice-versa. Requiring the **SM** to be symmetrical under these transformations re-
 993 quires the existence of a bosonic partner for every current matter fermion in the
 994 **SM** and a fermionic partner for every boson. The partners are called sparticles,
 995 where quarks partner with squarks and leptons partner with sleptons, and each
 996 boson has a fermionic partner called a gaugino, such as the wino for the W boson.
 997 The superpartners, in the original form of the theory, should be identical to the
 998 original particle in every way except for spin; that is they would have the same
 999 quantum charges and the same mass.

1000 However, the simplest version of the theory, where the symmetry is unbroken,
 1001 is incompatible with current observations of physics in a number of systems. For
 1002 example, the existence of an electron with spin-0 would introduce a stable, elec-
 1003 trically charged constituent of atoms that would not follow the Pauli exclusion
 1004 principle and would thus significantly change atomic structure. Various high en-
 1005 ergy physics measurements have also confirmed the spin of the W and Z bosons,
 1006 for example, and a fermionic gaugino has never been produced at those masses.
 1007 The solution to this incompatibility with observation is to conjecture that the
 1008 symmetry exists but is broken, where the masses of the supersymmetric parti-
 1009 cles are significantly larger than those of the current **SM** particles.

1010 3.1 STRUCTURE AND THE MSSM

1011 There are a number of ways to model **SUSY**, but many of the resulting phenomena
 1012 are similar, and a discussion of an example is sufficient to describe the structure
 1013 and results of the theory. The **MSSM** is one example of a complete description
 1014 that includes the necessary symmetry breaking to result in the different masses
 1015 between particles and sparticles. It is called minimal because it is designed to
 1016 use the simplest possible extension to the **SM** that incorporates **SUSY** and remains
 1017 self-consistent. The theory includes a sparticle partner for every standard model
 1018 particle, which are listed in Table 1.

1019 To then provide the different masses for those sparticles, the **MSSM** then intro-
 1020 duces a second Higgs interaction. The resulting scalar field, along with the origi-
 1021 nal Higgs field, generates five total particles, h^0 , the original Higgs boson, A^0 , H^0 ,
 1022 and H^\pm , where the last two are electrically charged. These Higgs bosons can mix
 1023 with the supersymmetric gauginos to form a series of mass eigenstates. These

Sector	Particles	Sparticles
Baryonic Matter	(u, d)	(\tilde{u}, \tilde{d})
	(c, s)	(\tilde{c}, \tilde{s})
	(t, b)	(\tilde{t}, \tilde{b})
Leptonic Matter	(ν_e, e)	$(\tilde{\nu}_e, \tilde{e})$
	(ν_μ, μ)	$(\tilde{\nu}_\mu, \tilde{\mu})$
	(ν_τ, τ)	$(\tilde{\nu}_\tau, \tilde{\tau})$
Higgs	(H_u^+, H_u^0)	$(\tilde{H}_u^+, \tilde{H}_u^0)$
	(H_d^0, H_d^-)	$(\tilde{H}_d^0, \tilde{H}_d^-)$
Strong	g	\tilde{g}
Electroweak	(W^\pm, W^0)	$(\tilde{W}^\pm, \tilde{W}^0)$
	B^0	\tilde{B}^0

Table 1: The particles in the **SM** and their corresponding superpartners in the **MSSM**.

1024 are usually referred to by the order of their masses, where the neutral gauginos
 1025 (neutralinos) are labelled $\tilde{\chi}_1^0, \tilde{\chi}_2^0, \tilde{\chi}_3^0$, and $\tilde{\chi}_4^0$. The charged gauginos (charginos)
 1026 are similarly labelled $\tilde{\chi}_1^\pm$ and $\tilde{\chi}_2^\pm$.

1027 In addition to the new particle content, the **MSSM** introduces new interactions
 1028 for the gauge bosons and gauginos. All interaction terms are added to the La-
 1029 grangian which describe the interaction of a gauge boson or gaugino with a par-
 1030 ticle or sparticle with the appropriate charge. Such terms include a few interac-
 1031 tions which would violate the observed $B - L$ symmetry that prevents proton
 1032 decay. Either the couplings on these terms must be fine-tuned to match the ex-
 1033 perimental limits on those decays, or an additional symmetry must be imposed
 1034 to exclude the terms. The **MSSM** and several other **SUSY** models choose to intro-
 1035 duce a new symmetry known as R-parity. Sparticles are R-parity odd while **SM**
 1036 particles are R-parity even. And by requiring that each term in the supersymmet-
 1037 ric Lagrangian conserves R-parity, it is enforced that sparticles are produced in
 1038 pairs.

1039 The conservation of R-parity removes the $B - L$ violating terms naturally
 1040 from the Lagrangian. The remaining terms include all of the interactions of the
 1041 **SM** where two of the particles are replaced with their **SUSY** partners, so that R-
 1042 parity is conserved in the interactions. This also has an important significance in
 1043 making the **LSP**, the $\tilde{\chi}_1^0$, stable, as it cannot decay to only **SM** particles without vi-
 1044 olating the conservation of R-parity. The heavier sparticles then decay in chains,
 1045 emitting an **SM** particle in each step, and leaving behind the **LSP** at the end of the
 1046 chain.

1047 3.2 MOTIVATION

4

1048

1049 LONG-LIVED PARTICLES

1050 4.1 MECHANISMS

1051 4.1.1 EXAMPLES IN SUPERSYMMETRY

1052 4.2 PHENOMENOLOGY

1053 4.2.1 DISIMILARITIES TO PROMPT DECAYS

1054 4.2.2 CHARACTERISTIC SIGNATURES

1055

PART III

1056

EXPERIMENTAL STRUCTURE AND RECONSTRUCTION

1057

You can put some informational part preamble text here.

1058

1059 THE LARGE HADRON COLLIDER

1060 The LHC, a two-ring superconducting hadron accelerator, provides high energy
1061 proton-proton collisions for several large experiments at European Organization
1062 for Nuclear Research (CERN) in Geneva, Switzerland [3, 4]. It is the largest,
1063 highest-luminosity, and highest-energy proton collider ever built, and was con-
1064 structed by a collaboration of more than 10,000 scientists from the more than
1065 100 countries that contribute to CERN. The original design of the LHC focused on
1066 providing collision energies of up to 14 TeV and generating enough collisions to
1067 reveal physics beyond the SM which is predicted to exist at higher energy scales.

1068 The LHC was installed in an existing 27 km tunnel at CERN which was origi-
1069 nally designed to house the Large Electron Positron collider (LEP). This allows
1070 the collider to use existing accelerators at the same complex to provide the initial
1071 acceleration of protons up to 450 GeV before injecting into LHC. The injected
1072 hadrons are accelerated up to as much as 14 TeV while being focused into two
1073 beams traveling in opposite directions. During this process the protons circulate
1074 around the tunnel millions of times, while the beams are intermittently crossed
1075 at the four locations of the experiments to provide collisions. These collision
1076 points correspond to the four major LHC experiments: ATLAS, Compact Muon
1077 Solenoid (CMS), Large Hadron Collider beauty experiment (LHCb), and A Large
1078 Ion Collider Experiment (ALICE), and Figure 7 shows the layout of the exper-
1079 iments both on the surface and below. ATLAS and CMS are both general pur-
1080 pose, high-luminosity detectors which search for a wide range of new types of
1081 physics [5, 6]. LHCb studies the interactions of b-hadrons to explore the asymme-
1082 try between matter and antimatter [7]. ALICE focuses on the collisions of lead
1083 ions, which the LHC also provides, in order to study the properties of quark-
1084 gluon plasma [8].

1085 During the first five years of operation, after the LHC turned on in 2010, the
1086 LHC has provided four major data collecting periods. In 2010 the LHC generated
1087 collisions at several energies, starting at 900 GeV. It increased the energy from
1088 900 GeV to 2.76 TeV and then subsequently to 7 TeV, with a peak luminos-
1089 ity of $2 \times 10^{32} \text{ cm}^{-2}\text{s}^{-1}$, and a total delivered luminosity of 50 pb^{-1} . The next
1090 run, during 2011, continued the operation at 7 TeV and provided an additional 5
1091 fb^{-1} with a peak luminosity of $4 \times 10^{33} \text{ cm}^{-2}\text{s}^{-1}$. The energy was then increased
1092 to 8 TeV for the data collection during 2012, which provided 23 fb^{-1} with a peak
1093 luminosity of $7.7 \times 10^{33} \text{ cm}^{-2}\text{s}^{-1}$. After the first long shutdown for 2013 and
1094 2014, the LHC resumed operation and increased the energy to 13 TeV in 2015,
1095 where it delivered 4.2 fb^{-1} with a peak luminosity of $5.5 \times 10^{33} \text{ cm}^{-2}\text{s}^{-1}$. The
1096 LHC is currently providing additional 13 TeV collisions in 2016 with higher lu-
1097 minosities than during any previous data collection periods. These running peri-
1098 ods are summarized in Figure 8, which shows the total delivered luminosity over

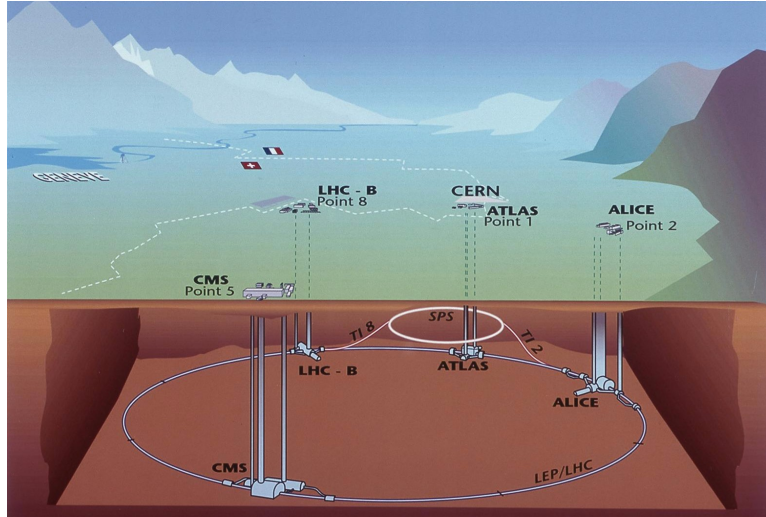


Figure 7: The four collision points and corresponding experiments of the [LHC](#). The image includes the location of the nearby city of Geneva as well as the border of France and Switzerland.

time for the [ATLAS](#) experiment during each of the four years of data collection since 2011.

5.1 INJECTION CHAIN

The [LHC](#) takes advantage of the presence of previously built accelerators at [CERN](#) to work up to the target energy in consecutive stages. The series of accelerators that feed into the [LHC](#) are known collectively as the injection chain, and together with the [LHC](#) form the accelerator complex. The full complex is illustrated in Figure 9, which details the complex series required to reach collisions of 13 or 14 TeV.

Protons at the [LHC](#) begin as hydrogen atoms in the Linac 2, a linear accelerator which replaced Linac 1 as the primary proton accelerator at [CERN](#) in 1978. In Linac 2, the hydrogen atoms are stripped of their electrons by a strong magnetic field, and the resulting protons are accelerated up to 50 MeV by cylindrical conductors charged by radio frequency cavities. The protons are then transferred to the Proton Synchrotron Booster ([PSB](#)), which uses a stack of four synchrotron rings to accelerate the protons up to 1.4 GeV. Then the protons are injected into the Proton Synchrotron ([PS](#)) which again uses synchrotron rings to bring the energy up to 25 GeV. The intermediate step between Linac 2 and the [PS](#) is not directly necessary, as the [PS](#) can accelerate protons starting from as low as 50 MeV. The inclusion of the [PSB](#) allows the [PS](#) to accept a higher intensity of injection and so increases the deliverable luminosity in the [LHC](#). The penultimate stage of acceleration is provided by the Super Proton Synchrotron ([SPS](#)), a large synchrotron with a 7 km circumference that was commissioned at [CERN](#) in 1976. During this step the protons increase in energy to 450 GeV, after which they can be directly injected into the [LHC](#).

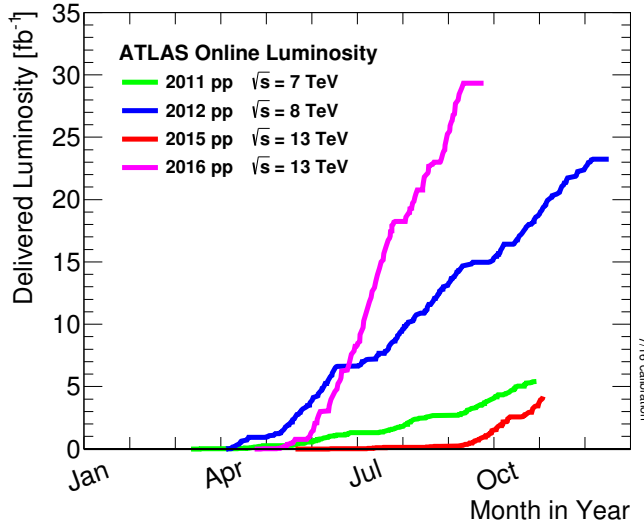


Figure 8: The cumulative luminosity over time delivered to the [ATLAS](#) experiment from high energy proton-proton collisions since 2011. The energies of the collisions are listed for each of the data-taking periods.

The final step is the [LHC](#) itself, which receives protons from the [SPS](#) into two separate beam pipes which circulate in opposite directions. The filling process at this steps takes approximately 4 minutes, and the subsequent acceleration to the final energy (6.5 TeV during 2015 and up to 7 TeV by design) takes approximately half an hour. At this point the protons circulate around the circumference tens of thousands of times a second and continue for up to two hours.

5.2 DESIGN

5.2.1 LAYOUT

Many of the aspects of the [LHC](#) design are driven by the use of the existing [LEP](#) tunnel. This tunnel slopes gradually, with a 1.4% decline, with 90% of its length built into molasse rock which is particularly well suited to the application. The circumference is composed of eight 2987 meter arcs and eight 528 meter straight sections which connect them; this configuration is illustrated in Figure 10. The tunnel diameter is 3.7 m throughout its length.

The design energy is directly limited by the size of this tunnel, with its radius of curvature of 2804 m. A significant magnetic field is required to curve the protons around that radius of curvature; the relationship is given by

$$p \simeq 0.3BR \quad (13)$$

where p is the momentum of the particle in GeV, B is the magnetic field in Tesla, and R is the radius of curvature in meters. From the target design energy of 14 TeV, or 7 TeV of momentum for protons in each beam, the required magnetic field is 8.33 Tesla. This is too large a field strength to be practical with

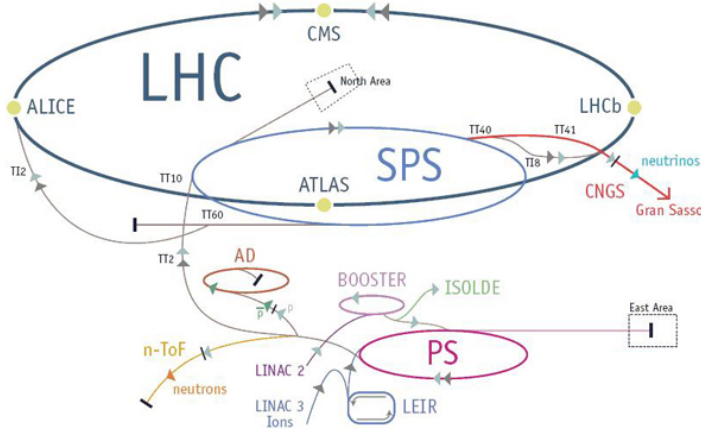


Figure 9: The accelerator complex that builds up to the full design energies at the [LHC](#).
The protons are passed in order to Linac 2, the [PSB](#), the [PS](#), the [SPS](#) and then the [LHC](#).

iron electromagnets, because of the enormous power required and the resulting requirements for cooling. Because of these constraints, the [LHC](#) uses superconducting magnets which can maintain that field strength with significantly less power consumption.

5.2.2 MAGNETS

Specifically the magnets chosen were Niobium and Titanium (NbTi) which allow for field strengths as high as 10 Tesla when cooled down to 1.9 K. Reaching the target temperature of 1.9 K for all of the magnets requires superfluid helium and a large cryogenic system along the entire length of the tunnel. During normal operation, the [LHC](#) uses 120 tonnes of helium within the magnets, and the entire system is cooled by eight cryogenic helium refrigerators. The temperature increase that occurs during transit from the refrigerator along the beam necessitates that the refrigerators cool the helium down to 1.8 K. Any significant increase above this temperature range can remove the superconductive properties of the magnets, which in turn generates drastically larger heat losses from the current within the magnets and causes a rapid rise in temperature called a quench.

In all there are approximately 8000 superconducting magnets distributed around the [LHC](#). The 1232 bending magnets, which keep the protons curving along the length of the beam, are twin bore cryodipoles, which allow both proton beams to be accommodated by one magnet and all of the associated cooling structure. Figure 11 shows the cross section of the design for these dipoles. The magnets are very large, 16.5 m long with a diameter of 0.57 meters and a total weight of 28 tonnes. They are slightly curved, with an angle of 5.1 mrad, in order to carefully match the beam path. The twin bore accommodates both magnets inside the two 5 cm diameter holes which are surrounded by the superconducting coils. The coils require 12 kA of current in order to produce the required mag-

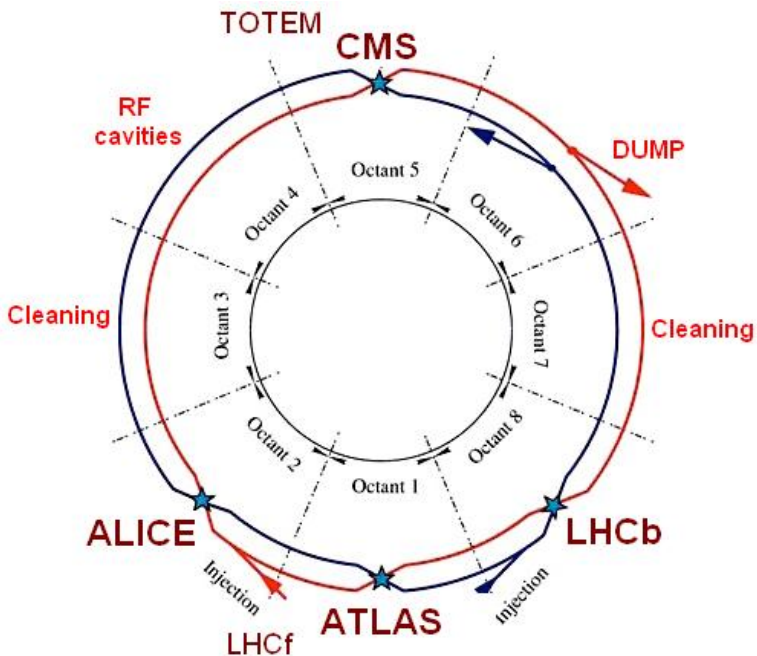


Figure 10: A schematic of the layout of the LHC, not to scale. The arched and straight sections are illustrated at the bottom of the schematic, and all four crossing sites are indicated with their respective experiments.

1172 netic field. These coils are comprised of NbTi cable wound in two layers; the
 1173 wire in the inner layer has a diameter of 1.065 mm while the wire in the outer
 1174 layer has a diameter of 0.825 mm.

1175 The large currents in the wires, along with the magnetic field produced, result
 1176 in forces on the magnets which would tend to push them apart with over 10,000
 1177 Newtons per meter. Constraining the magnets requires a significant amount of
 1178 structure including non-magnetic stainless steel collars. Both the presence of
 1179 these electromagnetic forces and the varying thermal contraction coefficient of
 1180 the pieces of the magnet produce significant forces on the cold mass structure.
 1181 The cold mass is carefully engineered to so that these stresses do not significantly
 1182 alter the magnetic field shape, which must be maintained between magnets to a
 1183 precision of approximately 10^{-4} for successful operation.

1184 The remaining 6800 magnets are a variety of quadrupole, sextapole, octopole,
 1185 and single bore dipole magnets. These are used to damp oscillations, correct
 1186 beam trajectories, focus the beams during circulation, and to squeeze the beams
 1187 before collisions.

1188 5.2.3 RF CAVITIES

1189 Sixteen RF cavities produce the actual acceleration of the proton beam up to the
 1190 design energy. These RF cavities are tuned to operate at 400 MHz, and are pow-
 1191 ered by high-powered electron beams modulated at the same frequency, called
 1192 klystrons. The resonance within the cavity with the oscillating electric field
 1193 establishes a voltage differential of 2 MV per cavity. The sixteen cavities are

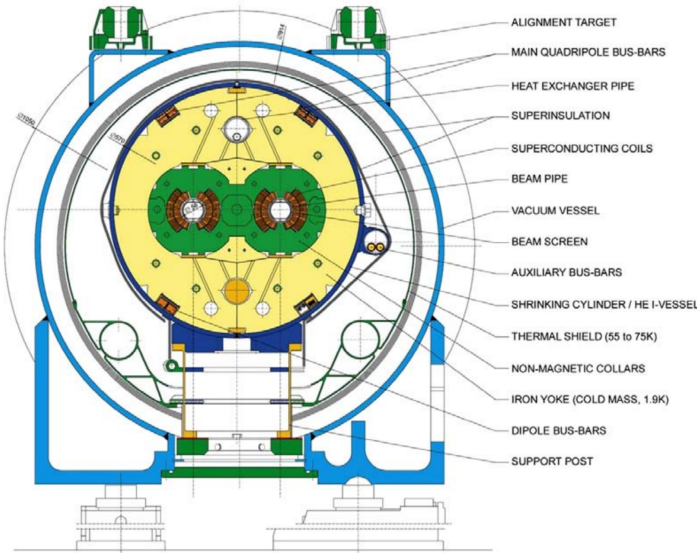


Figure 11: A cross section of the cryodipole magnets which bend the flight path of protons around the circumference of the LHC. The diagram includes both the superconducting coils which produce the magnetic field and the structural elements which keep the magnets precisely aligned.

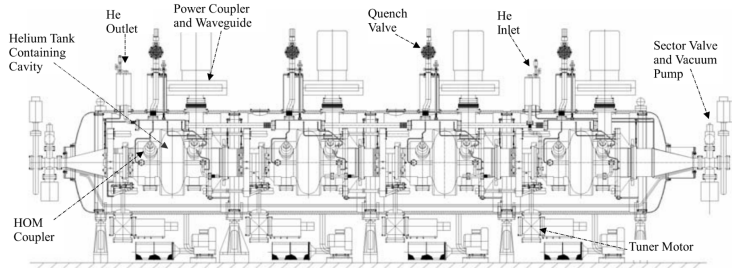


Figure 12: The arrangement of four RF cavities within a cryomodule.

split between the two beams, so combined the cavities provide 16 MV per beam, which accelerate the protons on each consecutive pass through the cavity. This acceleration is also necessary during circulation even after the target energy has been reached in order to compensate for losses from synchrotron radiation.

The cavities are arranged in cryomodules which contain four cavities, with two cryomodules per beam; this arrangement is illustrated in Figure 12. These cryomodules are necessary to maintain the superconducting state of the cavities, which are also constructed from niobium. The RF cavities use niobium along with copper to allow for low power losses in the superconductors. The copper provides a reduced susceptibility to quenching, as it rapidly conducts away heat generated by imperfections in the niobium, as well as natural shielding from the earth's magnetic field which can interfere with the RF system.

The nature of the radio frequency oscillations tends to group protons together into buckets. A proton traveling exactly in phase with the RF oscillations will not be displaced at all during a single circulation, and those slightly ahead or behind

1209 of that phase will slightly decelerate or accelerate, respectively. This produces
 1210 separate clusters of protons which arrive in phase to the cavities every 2.5 ns,
 1211 corresponding to the 400 MHz frequency.

1212 5.2.4 BEAM

1213 The beams of protons circulate within 54 km of 5 cm diameter beam pipe. This
 1214 entire structure is kept under vacuum at 1.9 K to prevent interactions between
 1215 the beam pipe and the magnets as well as to prevent any interactions between the
 1216 circulating protons and gas in the pipe. The vacuum within the pipe establishes
 1217 a pressure as low as 10^{-9} mbar before the protons are introduced.

1218 Because of the very high energies of the circulating protons, synchrotron ra-
 1219 diation is not negligible in the bending regions. The protons are expected to
 1220 radiate 3.9 kW per beam at 14 TeV, with 0.22 W/m, which is enough power to
 1221 heat the liquid helium and cause a quench were it absorbed by the magnets. To
 1222 prevent this, a copper screen is placed within the vacuum tube that absorb the
 1223 emitted photons. This screen is kept between 5 and 20 K by the liquid helium
 1224 cooling system.

1225 5.3 LUMINOSITY PARAMETERS

1226 In addition to the high energy of the collisions, the rate of collisions is extremely
 1227 important to enabling the discovery of new physics. Many measurements and
 1228 searches require a large number of events in order to be able to make statistically
 1229 significant conclusions. The rate of collisions is measured using luminosity, the
 1230 number of collisions per unit time and unit cross section for the proton-proton
 1231 collisions. From the beam parameters, luminosity is given by

$$\mathcal{L} = \frac{N_b^2 n_b f_{rev} \gamma}{4\pi\epsilon_n \beta^*} F \quad (14)$$

1232 where N_b is the number of protons per bunch, n_b is the number of bunches per
 1233 beam, f_{rev} is the frequency of revolution, γ is the Lorentz factor for the protons
 1234 at the circulating energy, ϵ_n is the emittance, β^* is the amplitude function at the
 1235 collision point, and F is a geometric factor that accounts for the crossing angle of
 1236 the beams at the collision point. The emittance measures the average spread of
 1237 particles in both position and momentum space, while the amplitude function
 1238 is a beam parameter which measures how much the beam has been squeezed.
 1239 Together ϵ_n and β^* give the size of the beam in the transverse direction, $\sigma = \sqrt{\epsilon\beta^*}$. β
 1240 changes over the length of the beam as the accessory magnets shape the
 1241 distribution of protons, but only the value at the point of collisions, β^* , affects
 1242 the luminosity.

1243 The luminosity is maximized to the extent possible by tuning the parameters
 1244 in Equation 14. A number of these are constrained by the design decisions. The
 1245 revolution frequency is determined entirely by the length of the tunnel, as the

Parameter	Unit	Injection	Nominal
Beam Energy	TeV	0.450	7
Peak Instantaneous Luminosity	$\text{cm}^{-2}\text{s}^{-1}$	-	10^{34}
Bunch Spacing	ns	25	25
Number of Filled Bunches	-	2808	2808
Normalized Transverse Emittance	μm	3.75	3.75
Frequency	MHz	400.789	400.790
RF Voltage/Beam	MV	8	16
Stored Energy	MJ	-	362
Magnetic Field	T	0.54	8.33
Operating Temperature	K	1.9	1.9

Table 2: The design parameters of the [LHC](#) beam that determines the energy of collisions and the luminosity, for both the injection of protons and at the nominal circulation.

1246 protons travel at very close to the speed of light. The geometric factor F is de-
 1247 termined by the crossing angle of the beams at the collision points, again a com-
 1248 ponent of the tunnel design; this angle is already very small at $285 \mu\text{rad}$, which
 1249 helps to maximize the geometric factor.

1250 The major pieces that can be adjusted are the number of protons per bunch,
 1251 N_b , the number of bunches in the beam, n_b , and the amplitude function β . In-
 1252 creasing either N_b or n_b increases the amount of energy stored in the beam,
 1253 which presents a danger if control of the beam is lost. At design specifications,
 1254 the beam stores 362 MJ, which is enough energy to damage the detectors or ac-
 1255 celerator if the beam were to wander out of the beam pipe. So, the luminosity
 1256 is primarily controlled at the [LHC](#) by adjusting β^* , where lowering β^* increases
 1257 the luminosity. β^* is tuned to provide the various values of luminosity used at
 1258 the [LHC](#) which can be raised to as much as 10^{34} .

1259 The nominal bunch structure consists of 3654 bunches, each holding 10^{11} pro-
 1260 tons, which cross a collision point in 25 ns. These are further subdivided into the
 1261 buckets mentioned in Section 5.2.3 by the clustering properties of the [RF](#) cavities.
 1262 The bunches are further grouped into trains of 72 bunches which are separated
 1263 by a gap which would otherwise hold 12 bunches. At nominal operation 2808
 1264 of the bunches will actually be filled with protons, while the remainder are left
 1265 empty to form an abort gap that can be used in case the beam needs to be dumped.

1266 The various beam parameters are summarized in Table 2 for the designed op-
 1267 eration. In practice the beam has operated at lower energies and lower luminosi-
 1268 ties than the design values, but the [LHC](#) is expected to operate at the full design
 1269 values during Run 2.

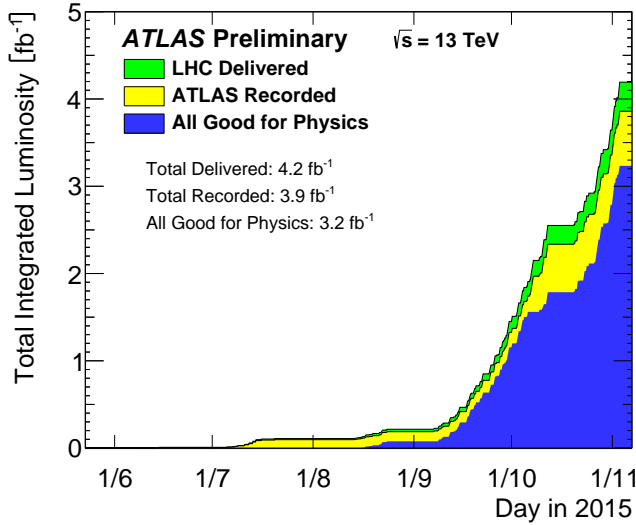


Figure 13: The cumulative luminosity versus time delivered to ATLAS (green), recorded by ATLAS (yellow), and certified to be good quality data (blue) during stable beams for pp collisions at 13 TeV in 2015.

1270 5.4 DELIVERED LUMINOSITY

During the data collection of 2015, the [LHC](#) operated at luminosities as large as 5×10^{33} . It is convenient to refer to the integrated luminosity, the integral of the instantaneous luminosity, which corresponds directly to the number of delivered events for a given process.

$$N = \sigma \times \int \mathcal{L}(t) dt$$

1271 where σ is the cross section for the process of interest. The integrated luminosity over time is shown in Figure 13. This includes the luminosity delivered by
 1272 the [LHC](#) as well as the luminosity that was recorded by [ATLAS](#). Some of the de-
 1273 livered luminosity is not recorded because [ATLAS](#) is placed in standby until the
 1274 [LHC](#) reports that the beam conditions are stable, and only then does [ATLAS](#) begin
 1275 recording. The figure also includes the amount of luminosity marked as good for
 1276 physics, which includes additional requirements on the operation of the detector
 1277 during data collection that are necessary for precise measurements.
 1278

1279 In addition to the instantaneous luminosity, the beam conditions also influ-
 1280 ence the number of collisions that occur within a single bunch crossing. The
 1281 multiple interactions at each crossing are referred to as pileup, often denoted μ ,
 1282 and each of these interactions are present in a single measured event. Figure 14
 1283 shows the luminosity-weighted distribution of the mean number of interactions
 1284 for events collected in 2015. The presence of as many as 20 events in a single
 1285 collision provides a significant challenge in reconstructing events and isolating
 1286 the targeted physical processes.

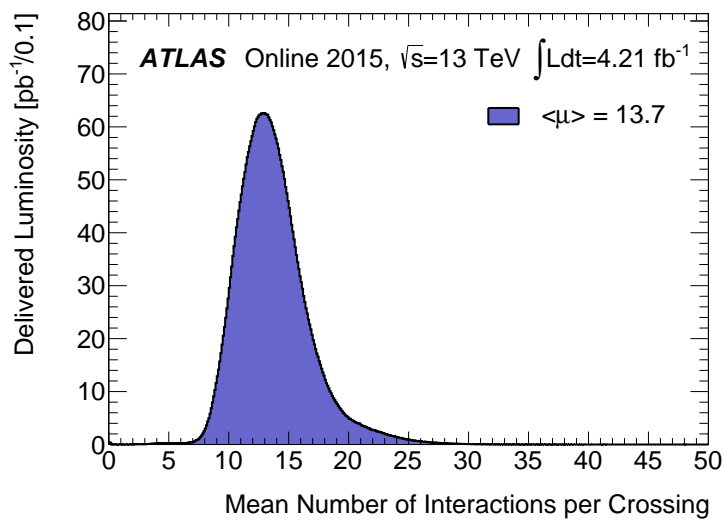


Figure 14: The luminosity-weighted distribution of the mean number of interactions per crossing for the 2015 pp collision data at 13 TeV.

1287

1288 THE ATLAS DETECTOR

1289 The four major LHC experiments at CERN seek to use the never before matched
1290 energies and luminosities of the new collider to explore the boundaries of par-
1291 ticle physics and to gain insight into the fundamental forces of nature. Two of
1292 these experiments, ATLAS and CMS, are general purpose detectors that seek to
1293 measure a variety of processes in the up to 14 TeV proton-proton collisions that
1294 occur as much as 40 million times per second at the LHC at the design luminosity
1295 of $10^{34} \text{ cm}^{-2}\text{s}^{-1}$. ATLAS employs a hermetic detector design, one which encloses
1296 the particle collisions as completely as possible with detecting elements, that al-
1297 lows it to study a wide range of physics from SM and Higgs measurements to
1298 searches for new physics in models like Supersymmetry [5].

1299 Accommodating this wide variety of goals is a challenge for the design of the
1300 detector. The wide range of energies involved requires high measurement pre-
1301 cision over several orders of magnitude and the ability to measure a variety of
1302 particle types. At the time of the construction of ATLAS, the Higgs boson had yet
1303 to be discovered, but the diphoton decay mode was (correctly) expected to be
1304 important and necessitated a high resolution photon measurement. The poten-
1305 tial for decays of new heavy gauge bosons, W' and Z', required a similarly high
1306 momentum resolution for leptons with momentum up to several TeV. Hadronic
1307 decay modes of several possible new high energy particles could result in very
1308 energetic jets, again up to several TeV, and reconstructing the decay resonances
1309 would again require good energy resolution. Several models, such as SUSY or Ex-
1310 tra Dimensions, predict the existence of particles which would not interact with
1311 traditional detecting elements. However these particles can still be observed in a
1312 hermetic detector by accurately measuring the remaining event constituents to
1313 observe an imbalance in energy called missing energy or E_T^{miss} . Measuring E_T^{miss}
1314 implicitly requires a good resolution on all SM particles that can be produced.
1315 And at the lower end of the energy spectrum, precision SM measurements would
1316 require good resolution of a variety of particle types at energies as low as a few
1317 GeV, so the design needs to accommodate roughly three orders of magnitude.

1318 This broad spectrum of measurements requires a variety of detector systems
1319 working together to form a cohesive picture of each collision. Two large magnet
1320 systems provide magnetic fields that provide a curvature to the propagation of
1321 charged particles and allows for precision momentum measurements by other
1322 systems. The inner detector uses a combination of tracking technologies to re-
1323 construct particle trajectories and vertices for charged particles. A variety of
1324 calorimeters measure the energies of hadrons, electrons, and photons over a
1325 large solid angle. A large muon spectrometer identifies muons and uses the sec-
1326 ond magnet system to provide an independent measurement of their momentum
1327 from the inner detector and improve the resolution. The layout of all of these
1328 systems is shown in Figure 15.

1329 The performance goals needed to achieve the various targeted measurements
 1330 and searches discussed above can be summarized as resolution and coverage re-
 1331 quirements on each of these systems. Those requirements are listed in Table 3.

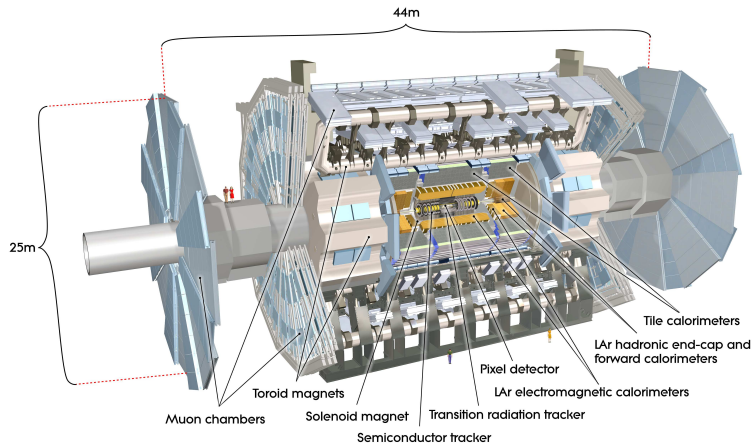


Figure 15: A cut-away schematic of the layout of the [ATLAS](#) detector. Each of the major subsystems is indicated.

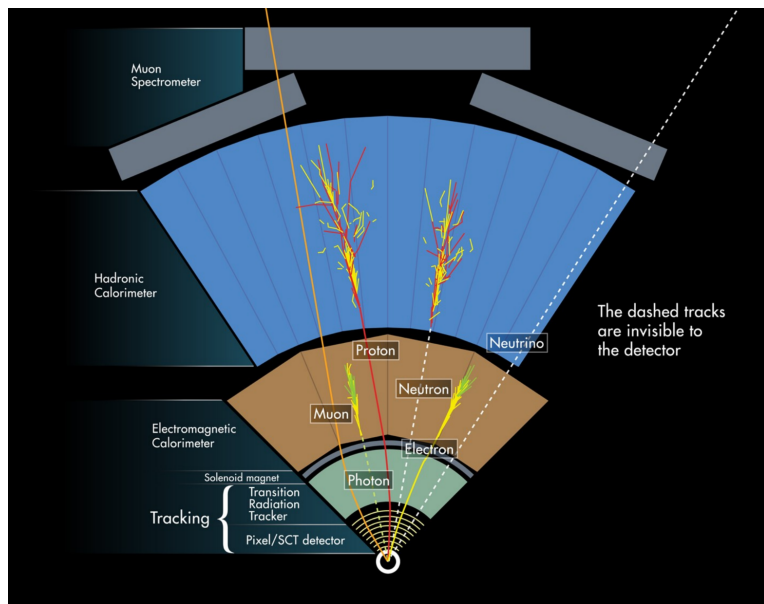


Figure 16: A cross-sectional slice of the [ATLAS](#) experiment which illustrates how the various SM particles interact with the detector systems.

1332 Incorporating these various pieces into a single detector is a significant tech-
 1333 nical challenge. The resulting detector has a diameter of 22 m, is 46 m long,
 1334 and weighs 7,000 tons; it is the largest volume particle detector ever constructed.
 1335 The various detector elements need to be constructed and assembled with pre-
 1336 cision as low as micrometers. These systems all need to function well even after
 1337 exposure to the significant radiation dose from the collisions. Designing, con-
 1338 structing, and installing the detector took the combined effort of more than 3000
 1339 scientists from 38 countries over almost two decades.

Detector Component	Required Resolution	$ \eta $ Coverage	
		Measurement	Trigger
Tracking	$\sigma_{p_T}/p_T = 0.05\% p_T + 1\%$	2.5	-
EM Calorimetry	$\sigma_E/E = 10\%/\sqrt{E} + 0.7\%$	3.2	2.5
Hadronic Calorimetry			
Barrel and Endcap	$\sigma_E/E = 50\%/\sqrt{E} + 3\%$	3.2	3.2
Forward	$\sigma_E/E = 100\%/\sqrt{E} + 10\%$	3.1 – 4.9	3.1 – 4.9
Muon Spectrometer	$\sigma_{p_T}/p_T = 10\% \text{ at } p_T = 1 \text{ TeV}$	2.7	2.4

Table 3: The performance goals for each of the subsystems of the [ATLAS](#) detector. The $|\eta|$ coverage specifies the range where the subsystem needs to be able to provide measurements with the specified resolution. The resolutions include a p_T or E dependence that is added in quadrature with a p_T/E independent piece.

1340 6.1 COORDINATE SYSTEM

1341 The coordinate system defined for the [ATLAS](#) detector is used throughout all of
 1342 the sections of this thesis. The choice of coordinate system reflects the cylindri-
 1343 cal symmetry of the [ATLAS](#) detector, and is oriented by the direction of the
 1344 beamline which defines the z -direction. The positive z side of the detector is
 1345 commonly referred to as the A -side, and the negative z side is referred to as
 1346 the C -side. The $x - y$ plane is then the plane transverse to the beam direction,
 1347 with the x direction defined as pointing from the interaction point to the center
 1348 of the [LHC](#) ring and the y direction defined as pointing upwards. The nominal
 1349 interaction point is the origin of this system.

1350 It is more convenient in practice to use a cylindrical coordinate system. The
 1351 angle from the z -axis is θ . The azimuthal angle uses the usual definition, with ϕ
 1352 running around the z -axis and $\phi = 0$ corresponding to the x -axis. Many aspects
 1353 of the detector are independent of the this coordinate to first order. The re-
 1354 maining direction is typically specified using rapidity or pseudorapidity, where
 1355 rapidity is defined as

$$y = \frac{1}{2} \ln \frac{E + p_z}{E - p_z} \quad (15)$$

1356 Rapidity is particularly useful to indicate the component along the z direction
 1357 because differences in rapidity are invariant to boosts along the z -direction. A
 1358 similar quantity which depends only the θ is pseudorapidity,

$$\eta = -\ln \tan \frac{\theta}{2} \quad (16)$$

1359 which is the same as rapidity when the particle is massless and in the limit where
 1360 the energy is much larger than the particle's mass. It is often useful to refer to
 1361 differences in solid angle using the pseudorapidity and the azimuthal angle:

$$\Delta R = \sqrt{\Delta\phi^2 + \Delta\eta^2} \quad (17)$$

1362 The pseudorapidity is also invariant to boosts along the z -axis for high mo-
 1363 mentum particles, and is preferable to rapidity because it does not depend on
 1364 the specific choice of particle. Pseudorapidity is also preferable to θ because
 1365 of the aforementioned boost-invariance and also because particle production is
 1366 roughly uniform in equal-width intervals of η up to about $\eta = 5.0$. A particle
 1367 traveling along the beampipe has $\eta = \text{inf}$ and a particle traveling perpendicular
 1368 to the beampipe has $\eta = 0$. The extent of the tracker, $|\eta| < 2.5$, corresponds
 1369 to approximately $0.05\pi < \theta[\text{rad}] < 0.95\pi$ and the extent of the calorimeters,
 1370 $|\eta| < 4.9$ corresponds to approximately $0.005\pi < \theta[\text{rad}] < 0.995\pi$. Many de-
 1371 tector components are broken into multiple subsystems to provide coverage at
 1372 greater $|\eta|$. The lower $|\eta|$ region is referred to as the barrel, typically with $|\eta| \lesssim 2$,
 1373 and the greater $|\eta|$ region is often referred to as the endcap.

1374 The initial energy and momentum of a proton-proton collision along the z di-
 1375 rection is unknown in hadron colliders because different energies and momenta
 1376 can be carried by the partons. Along the transverse plane, however, the vector
 1377 sum of momentum will be zero. For this reason, many physical quantities are
 1378 quantified in terms of their projection onto the transverse plan, such as p_T or
 1379 E_T . In addition, p_T alone determines the amount of curvature in the magnetic
 1380 field, and can be measured independently by measuring the curvature of a parti-
 1381 cle's propagation.

1382 6.2 MAGNETIC FIELD

1383 The magnet system used in [ATLAS](#) is designed to provide a substantial magnetic
 1384 field in the two regions where the trajectory of particles is measured, the inner
 1385 detector and the muon spectrometer. The magnetic field provides a curvature
 1386 to the trajectory of charged particles and allows the precision tracking measure-
 1387 ments to make high resolutions measurements of p_T . To provide a magnetic field
 1388 in these regions, [ATLAS](#) uses a hybrid system with four separate, superconduct-
 1389 ing magnets. A single solenoid provides a 2 T axial magnetic field for the inner
 1390 detector, while a barrel toroid and two endcap toroids produce a magnetic field
 1391 of 0.5 and 1 T, respectively, for the muon detectors. This geometry is illustrated
 1392 in Figure 17, and the parameters of the three magnet systems are summarized in
 1393 Table 4.

1394 The central solenoid uses a single-layer coil with a current of 7.730 kA to gen-
 1395 erate the 2 T axial field at the center of the magnet. The single-layer coil design
 1396 enables a minimal amount of material to be used in the solenoid's construction,
 1397 which is important because the solenoid is placed between the inner detector
 1398 and the calorimeters. At normal incidence the magnet has only 0.66 radiation
 1399 lengths worth of material, where one radiation length is the mean distance over

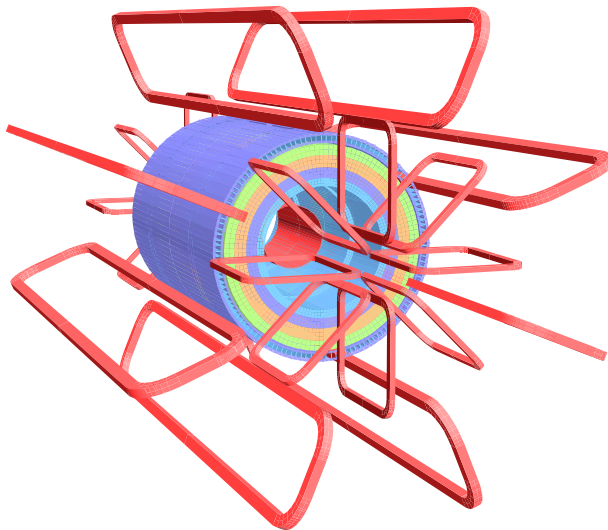


Figure 17: The layout of the four superconducting magnets in the [ATLAS](#) detector.

Parameter	Unit	Solenoid	Barrel Toroid	Endcap Toroids
Inner Diameter	m	2.4	9.4	1.7
Outer Diameter	m	2.6	20.1	10.7
Axial Length	m	5.3	25.3	5.0
Weight	tons	5.7	830	239
Conductor Size	mm ²	30×4.25	57×12	41×4.25
Peak Field	T	2.6	3.9	4.1
Heat Load	W	130	990	330
Current	kA	7.7	20.5	20.0
Stored Energy	MJ	38	1080	206

Table 4: A summary of the parameters of each of the three magnet systems on [ATLAS](#).

1400 which a high-energy electron loses all but $1/e$ of its energy through material in-
 1401 teractions [9]. The coil is made of a high-strength aluminum stabilized NbTi
 1402 superconductor which was optimized to achieve a high field with minimal thick-
 1403 ness. The axial magnetic field produced by the solenoid bends charged particles
 1404 in the ϕ direction.

1405 The barrel toroid consists of eight coils which generate a 0.5 T magnetic field
 1406 in the cylindrical region around the calorimeters with an approximately 20 kA
 1407 current. The coils are separated only by air to reduce the scattering of muons as
 1408 they propagate through the region. The coils are made of an aluminum stabilized
 1409 NbTiCu superconductor and each is separately housed in a vacuum and cold
 1410 chamber. This magnetic configuration produces a field in the ϕ and so curves
 1411 muons traversing the volume primarily in the η direction.

1412 The endcap toroids follow a similar design to the barrel toroid, with eight
 1413 separate NbTiCu coils, but in this case all eight are housed within a single cold
 1414 mass. This extra structure is necessary to withstand the Lorentz forces exerted
 1415 by the magnets. These magnets are rotated 22.5% relative to the barrel toroid to
 1416 provide a uniform field in the transition between the two systems. The endcap
 1417 toroids also produce a field in the ϕ direction and curve muons primarily in the
 1418 η direction.

1419 6.3 INNER DETECTOR

1420 The [ATLAS](#) inner detector provides excellent momentum resolution as well as
 1421 accurate primary and secondary vertex measurements through robust pattern
 1422 recognition that identifies tracks left by charged particles. These tracks fulfill
 1423 a number of important roles in the [ATLAS](#) measurement system: they measure
 1424 the momentum of charged particles including electrons and muons, they can
 1425 identify electrons or photon conversions, they assign various particles and jets
 1426 to different vertices, and they provide a correction to E_T^{miss} measurements from
 1427 low energy particles. The system has to be accurate enough to separate tracks
 1428 from dozens of vertices and to resolve each vertex individually, as well as accu-
 1429 rate enough to measure the p_T of very high momentum tracks which curve very
 1430 little even in the large magnetic field. This is accomplished by several indepen-
 1431 dent layers of tracking systems. Closest to the interaction point is the very high
 1432 granularity Pixel detector, which is followed by the [SCT](#) layers. These subdetec-
 1433 tors both use discrete space-points to reconstruct track patterns. The final layer,
 1434 the transition radiation tracker ([TRT](#)), uses many layers of straw tube elements
 1435 interleaved with transition radiation material to provide continuous tracking.
 1436 The arrangement of these subdetectors is shown in Figure 18. To provide the
 1437 desired hermetic coverage, the subdetectors are divided into barrel and endcap
 1438 geometries. Figure 19 shows the layout of the subdetectors in more detail, and
 1439 illustrates how tracks at various pseudorapidities can traverse the subdetectors;
 1440 tracks with $\eta > 1.1$ begin to traverse the endcap subdetectors rather than those
 1441 in the barrel, and tracks with $\eta > 1.7$ use primarily endcap elements. The [IBL](#)
 1442 was not present during the original commissioning of the inner detector and is
 1443 not shown in this figure.

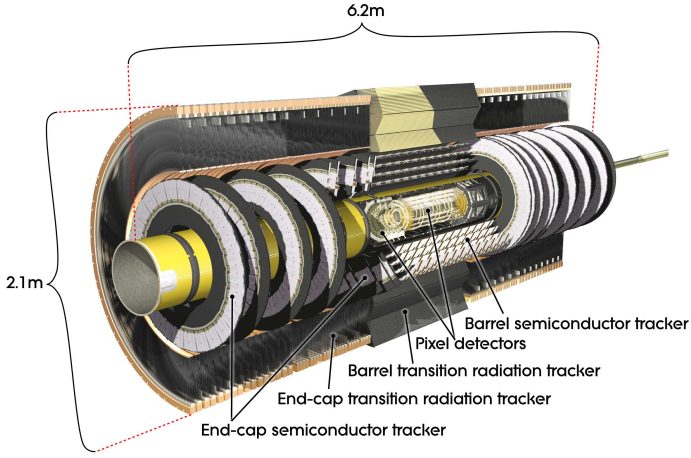


Figure 18: The arrangement of the subdetectors of the ATLAS inner detector. Each of the subdetectors is labeled in the cut-away view of the system.

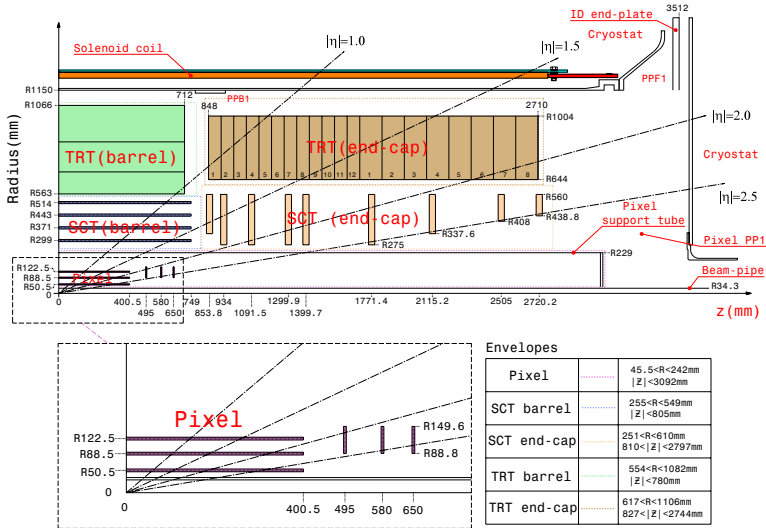


Figure 19: A quarter section of the ATLAS inner detector which shows the layout of each of the subdetectors in detail. The lower panel shows an enlarged view of the pixel detector. Example trajectories for a particle with $\eta = 1.0, 1.5, 2.0, 2.5$ are shown. The IBL, which was added after the original detector commissioning, is not shown.

1444 Figure 20 shows a computer generated three-dimensional view of the inner
 1445 detector along the beam axis, which emphasizes the straw tube structure of the
 1446 **TRT** as well as the overlapping geometry of the **SCT**. This figure also includes
 1447 the **IBL**, which was added during the long shutdown and provides an additional
 1448 measurement layer in the Pixel detector as of the beginning of Run 2. Figure 21
 1449 shows an alternative computer generated three-dimensional view transverse to
 1450 the beam axis which emphasizes the endcap structures of the **SCT** and **TRT**.

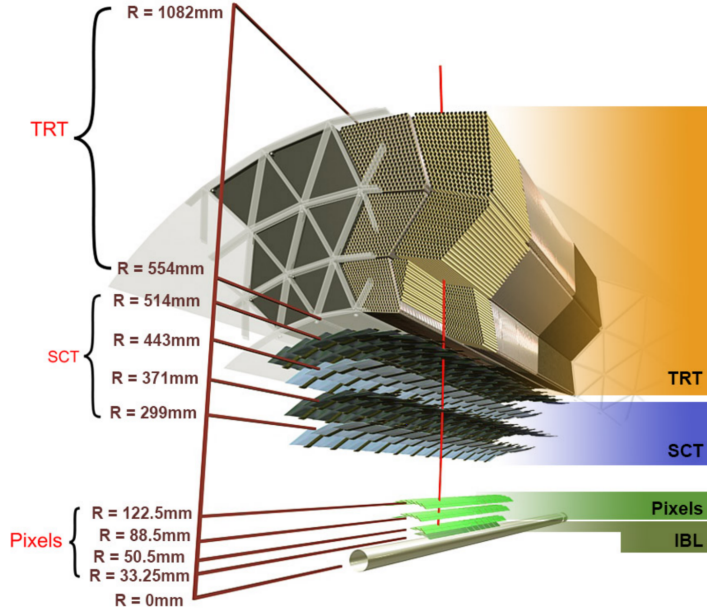


Figure 20: A computer generated three-dimensional view of the inner detector along the line of the beam axis. The subdetectors and their positions are labeled.

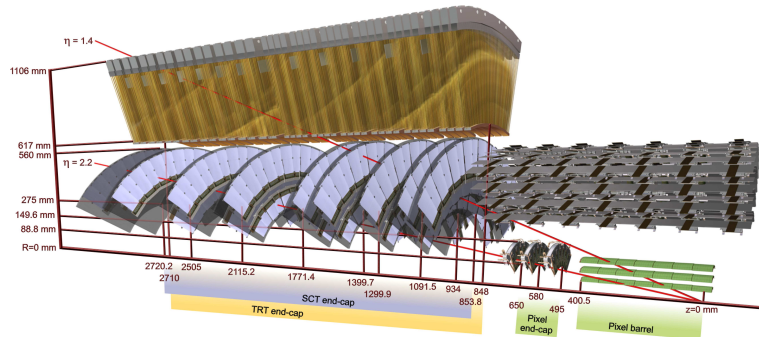


Figure 21: An alternative computer generated three-dimensional view of the inner detector transverse to the beam axis. The subdetectors and their positions are labeled.

1451 As the closest system to the interaction point, it is crucial for the inner de-
 1452 tector to use as little material as possible to avoid scattering of charged parti-
 1453 cles or photon conversions before they reach the remaining subdetectors. The
 1454 various components, including the readout electronics, cooling infrastructure,
 1455 gas volumes, and support structures, were designed to use as little material as

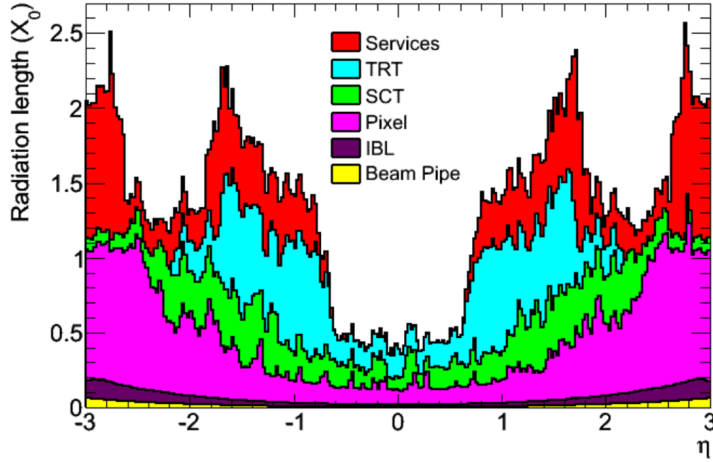


Figure 22: The integrated radiation lengths traversed by a straight track at the exit of the ID envelope, including the services and thermal enclosures. The distribution is shown as a function of $|\eta|$ and averaged over ϕ . The breakdown indicates the contributions of individual sub-detectors, including services in their active volume.

possible. Even with these optimizations, the combination of stringent performance requirements and the harsh radiation environment in the inner detector requires a significant amount of material. This material causes many electrons to lose most of their energy before reaching the electromagnetic calorimeter and approximately 40% of photons convert into an electron-positron pair while traversing the inner detector. Figure 22 shows the integrated radiation lengths traversed by a straight track in the inner detector as a function of η , grouped by subdetector. There is a large increase in the amount of material for support structures around $|\eta| = 1.7$, where the inner detector transitions from barrel to endcap.

The inner detector is designed to work as a cohesive unit to provide complete tracking information for charged particulars, and the subdetectors are complementary. Table 5 summarizes the parameters of each of the subdetectors as well as the parameters of the combined inner detector. Table 6 summarizes the expected performance that can be achieved by the inner detector as a whole.

6.3.1 PIXEL DETECTOR

The Pixel detector is the closest detector to the interaction point and therefore is designed to provide extremely high granularity while simultaneously handling a very large dose of radiation from collisions. It consists of four layers of silicon pixel modules, each of which provides a precision measurement on the trajectory of any charged particle. In the barrel region, the four layers are located at radial distances of 31 mm, 51 mm, 89 mm, and 123 mm. The three outer layers also include endcap elements, illustrated in Figure 19, which are located at 495 mm, 580 mm, and 650 mm away from the interaction point.

Parameter	Inner Detector	Pixel	SCT	TRT
Inner Radius	3.1 cm	3.1 cm	30 cm	56 cm
$ \eta $ Coverage	-	2.5	2.5	2.0
Cell Width	-	50 μm	80 μm	4 mm
Cell Length	-	400 μm	12 cm	70 cm
Material at $ \eta = 0.0$	0.3 X/X_0			
Material at $ \eta = 1.7$	1.2 X/X_0			
Material at $ \eta = 2.5$	0.5 X/X_0			
Number of Hits	48	4	8	36
Channels	99 M	92 M	6.3 M	350 k

Table 5: A summary of the parameters of the inner detector and each of the subdetectors [5].

1480 The pixel sensor technology uses a p-n junction of n-type bulk that contains
 1481 both p⁺ and n⁺ impurities. This combination is crucial in maintaining perfor-
 1482 mance after a significant radiation dose, as the n⁺ implants allow the sensor to
 1483 continue function after the n-type bulk has been converted to a p-type bulk by
 1484 the accumulation of radiation.

1485 The size of the pixels in the original three layers are 50 $\mu\text{m} \times$ 400 μm in the
 1486 $r - \phi$ and z directions, respectively. Those pixels are bump-bonded to front-end
 1487 readout chips, the FE-I3, which contains a total of 2880 pixels per chip. In the
 1488 three original pixel layers, the chips are grouped into modules composed of 16
 1489 chips each with 46,080 pixels per module and a total size of 20 mm x 60 mm
 1490 x 250 μm . The modules are further arranged into long rectangular structures
 1491 that run parallel to the beamline called staves. By tiling several staves with an
 1492 offset of 20°, the stave geometry provides full azimuthal coverage in the barrel
 1493 region while accommodating the readout and cable systems. The endcap regions
 1494 are instead arranged into petals and then into wheels. This arrangement can be
 1495 seen in Figure 23 which shows a computer-generated, cut-away image of the
 1496 outer three layers of the pixel detector. Together these three layers contain 1744
 1497 modules between the barrel and two endcap sections.

1498 The innermost layer, the IBL, was added during the long shutdown before Run
 1499 2, and provides the fourth track measurement. It was inserted directly into the
 1500 existing pixel detector by removing the existing beam pipe and replacing it with
 1501 a significantly smaller version. This insertion can be seen in action in Figure 24,
 1502 which emphasizes the extreme precision required to place the the 70 cm long
 1503 layer with only 2 mm of clearance. The IBL was commissioned to provide con-
 1504 tinued tracking robustness and high precision in the higher luminosity environ-
 1505 ment of Run 2 [11]. The proximity of this layer to the collisions necessitated an
 1506 even higher granularity and better radiation hardness than the other pixel lay-
 1507 ers. And the strict space requirements to add an active sensing layer so close to
 1508 the interaction point required a sensor chip with a much higher active area and
 1509 a larger overall area per chip. These requirements led to the development of a

Parameter	Particle	Value
Reconstruction Efficiency	Muon, $p_T = 1 \text{ GeV}$	96.8%
	Pion, $p_T = 1 \text{ GeV}$	84.0%
	Electron, $p_T = 5 \text{ GeV}$	90.0%
Momentum Resolution	$p_T = 1 \text{ GeV}, \eta \approx 0$	1.3%
	$p_T = 1 \text{ GeV}, \eta \approx 2.5$	2.0%
	$p_T = 100 \text{ GeV}, \eta \approx 0$	3.8%
	$p_T = 100 \text{ GeV}, \eta \approx 2.5$	11%
Transverse IP Resolution	$p_T = 1 \text{ GeV}, \eta \approx 0$	$75 \mu\text{m}\%$
	$p_T = 1 \text{ GeV}, \eta \approx 2.5$	$200 \mu\text{m}$
	$p_T = 1000 \text{ GeV}, \eta \approx 0$	$11 \mu\text{m}$
	$p_T = 1000 \text{ GeV}, \eta \approx 2.5$	$11 \mu\text{m}$
Longitudinal IP Resolution	$p_T = 1 \text{ GeV}, \eta \approx 0$	$150 \mu\text{m}\%$
	$p_T = 1 \text{ GeV}, \eta \approx 2.5$	$900 \mu\text{m}$
	$p_T = 1000 \text{ GeV}, \eta \approx 0$	$90 \mu\text{m}$
	$p_T = 1000 \text{ GeV}, \eta \approx 2.5$	$190 \mu\text{m}$

Table 6: A summary of the expected performance of the combined inner detector [10]. Included are the reconstruction efficiencies for multiple particle types as well as the momentum and IP resolution for various momenta.

1510 new chip type, the FE-I4 (compared to the FE-I3 chips used in the original pixel
 1511 detector) with improved radiation hardness and a larger active footprint of 90%.
 1512 The IBL is comprised of 448 of these individual chips arranged in 14 staves, with
 1513 26,880 pixels per chip and a chip size of 18.5 mm x 41.3 mm x 200 μm . The
 1514 staves, like in the other layers of the pixel detector, are offset by 14° to provide
 1515 full azimuthal coverage. This arrangement can be seen in Figure 25, which shows
 1516 two computer-generated images of the IBL geometry and includes the some of
 1517 the remaining pixel layers.

1518 6.3.2 SEMICONDUCTOR TRACKER

1519 The SCT, the subdetector which immediately surrounds the Pixel detector, pro-
 1520 vides additional discrete measurements of the trajectory of a charged particle.
 1521 Because the SCT is further away from the interaction point, the spatial resolution
 1522 does not need to be as high as in the pixel detector, and so the SCT uses micro-
 1523 strips instead of pixels. Although pixels provide a more accurate measurement,
 1524 the number of pixels and readout channels required to cover the cylindrical area
 1525 at the radius of the SCT layers would be prohibitively complicated and expensive.
 1526 Each individual silicon strip sensor contains 768 individual readout strips
 1527 with a total area of 6.36 cm x 6.40 cm and a pitch of 80 μm . Pairs of these sen-
 1528 sors are then bonded together to form a combined strip with a length of 12.8 cm.
 1529 Two of these combined strips are then placed back to back with a relative tilt

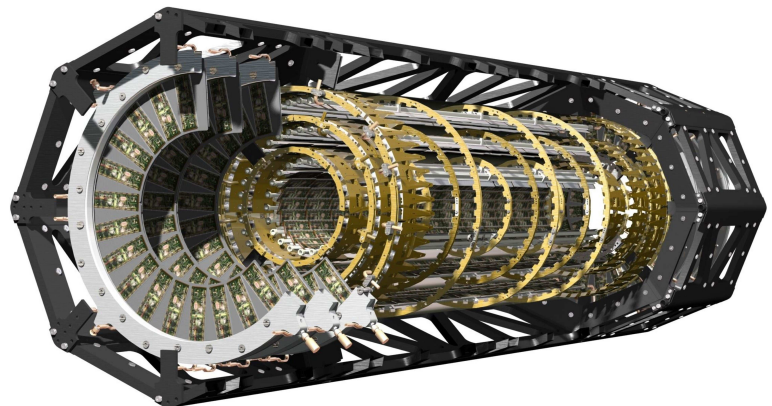


Figure 23



Figure 24: An image of the insertion of the [IBL](#) into the current pixel detector.

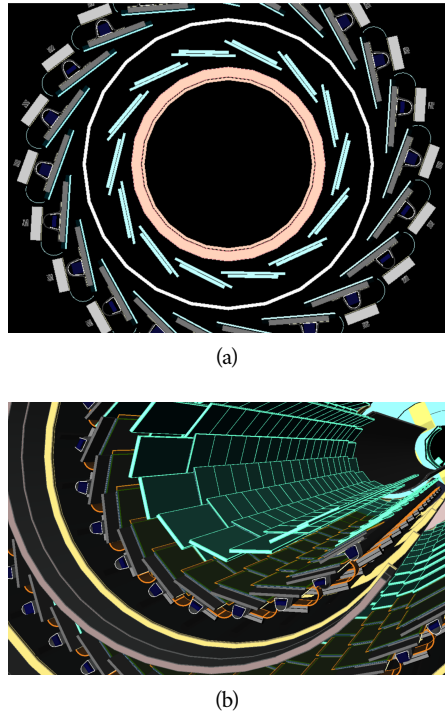


Figure 25: A three-dimensional computer-generated image of the geometry of the [IBL](#) with a view (a) mostly transverse to the beam pipe (b) mostly parallel to the beam pipe.

of 40 mrad. This geometry is illustrated in an exploded-out view in Figure 26. The purpose of angular offset of the consecutive layers is to allow the strip sensor areas to more accurately measure the position of a particle by comparing the overlap of the two strips which were traversed by a track.

Four of these double layers are placed in the barrel region, with radii of 284 mm, 355 mm, 427 mm, and 498 mm. Together these layers provide eight additional measurements for each track that traverses the central $|\eta|$ region. In the endcap region, the layers are arranged in wheels, with the double layers similarly offset to provide improved resolution. With these configurations, the [SCT](#) achieves a spatial resolution of $17 \mu\text{m}$ in the $r - \phi$ direction and $580 \mu\text{m}$ in the z direction.

6.3.3 TRANSITION RADIATION TRACKER

The final component of the inner detector, the [TRT](#), provides continuous tracking using straw drift tubes. The tubes are made of Kapton and aluminum with a diameter of 4 mm and are filled with a gas mixture of 70% Xe, 27% CO₂, and 3% O₂. At the center of each tube is a gold-plated anode tungsten wire $30 \mu\text{m}$ in diameter. When a charged particle passes through these tubes, it ionizes the gas within. The ions produced drift in the electric field established between the wire and the tube wall, and the large electric field near the wire produces avalanche multiplication and results in an electric current on the wire that is read out by the electronics and provides a track measurement. The time it takes the ioniza-

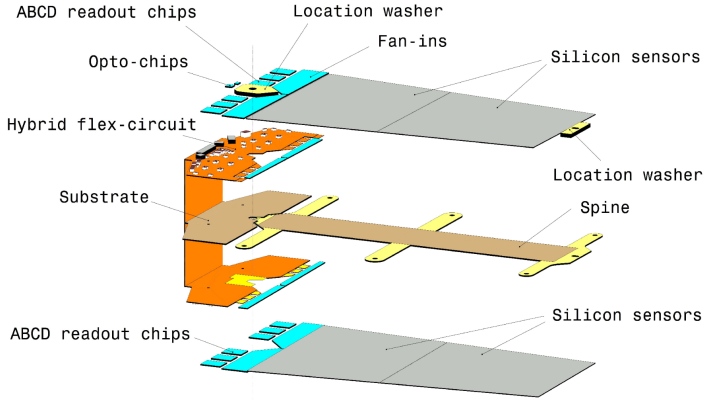


Figure 26: An exploded view of the geometry of the [SCT](#) double layers in the barrel region.

tion to drift to the wire can be used to estimate the distance from the wire that the particle passed through the tube; this gives a resolution on the distance of approximately $130\mu\text{m}$. Combining several such measurements between consecutive hits in the [TRT](#) tubes allows the trajectory of the particle to be reconstructed.

In addition to the continuous tracking, the detector can use transition radiation produced when a particle passes between the layers to distinguish between electrons and heavier charged particles. The space between the tubes is filled with CO_2 , and so has a different dielectric constant than the gas within the tubes which contains Xe. At the transition between those media, a relativistic particle emits radiation proportional to γ , so inversely proportional to mass at a fixed momentum. The photons produced in this transition then produces an ionization cascade which is significantly larger than the signal for the minimally-ionizing charged particles. To distinguish between these two cases, the [TRT](#) defines two signal thresholds, a low threshold for the typical signal produced by a minimally ionizing particle ([MIP](#)) and a high threshold for the the signal produced by transition radiation. A high momentum electron is expected to produce approximately 7 to 10 high threshold hits as it traverses the [TRT](#), and thus these hits provide a way to distinguish electrons from other charged particles.

The [TRT](#) contains 351,000 tubes in total, divided between the barrel and endcap regions. In the barrel region, the tubes are 144 cm long and arranged in 73 layers parallel to the beampipe. In the endcap region, the tubes are 37 cm long and arranged in 160 layers transverse to the beampipe. These configurations can be seen in Figure 20 and Figure 21. With this geometry the [TRT](#) achieves a resolution of $130\mu\text{m}$ in the $r - \phi$ direction.

1575 6.4 CALORIMETRY

1576 The combination of calorimeter systems used in [ATLAS](#) can measure the energy
 1577 of electrons, photons, hadrons, and hadronic jets with complete coverage up to
 1578 $|\eta| < 4.9$ and across ϕ . Unlike the inner detector, the calorimeters are capable
 1579 of measuring neutral particles. To accomplish precision measurements of these

1580 particle types, the [ATLAS](#) calorimeter system uses four individual calorimeters,
 1581 a [LAr](#) electromagnetic calorimeter in the barrel region, a tile hadronic calorime-
 1582 ter in the barrel region, a [LAr](#) hadronic endcap calorimeter, and a [LAr](#) forward
 1583 calorimeter. Together these provide hermetic coverage for the [ATLAS](#) detector.
 1584 The configuration of these calorimeters is illustrated in Figure 27. **Note: I could**
 1585 **make this section much longer. It might be nice to include a more com-**
 1586 **plete description of showers for example. I will extend this section if their**
 1587 **is space at the end.**

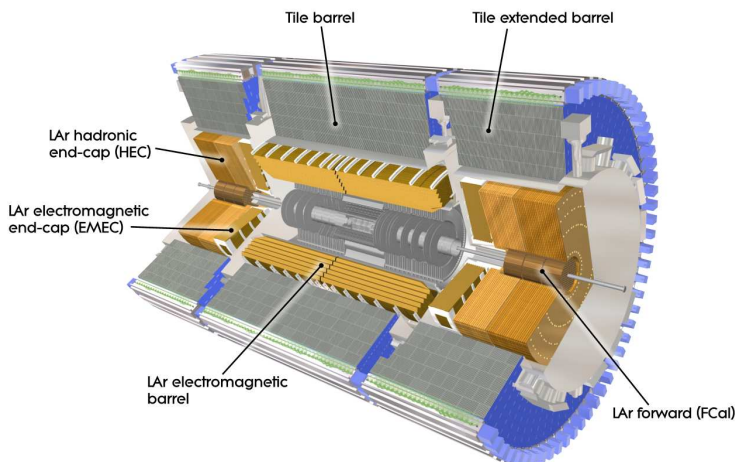


Figure 27

1588 The calorimeters are designed to absorb and measure the energy carried by
 1589 a particle, and completely stop the particle's propagation in the process. This
 1590 requires a significant amount of material to provide interactions. These interac-
 1591 tions then produce secondary particles, which can produce secondary particles
 1592 in turn, and thus form a cascade of particles called an electromagnetic ([EM](#)) or
 1593 hadronic shower, depending on the governing mechanism. Electromagnetic and
 1594 hadronic showers have very different properties and require different technolo-
 1595 gies to measure them accurately. All of the calorimeters in the [ATLAS](#) calorimeter
 1596 system are sampling calorimeters, that is they use alternating layers of absorbing
 1597 and active material. The dense absorbing layers initiate the showers while the ac-
 1598 tive layers measure the energy of the produced particles. A fraction of the energy
 1599 is lost in the inactive layers, so the energy measurement from the active layers
 1600 has to be corrected to estimate the actual energy of the particle.

1601 The [EM](#) calorimeter provides around 20 radiation lengths (X_0) while the hadronic
 1602 calorimeter provides around 10 interaction lengths (λ_0). As mentioned previ-
 1603 ously, radiation lengths measure the distance over which an electromagnetically
 1604 interacting particle loses a characteristic fraction of its energy. Interaction lengths,
 1605 on the other hand, measure the mean distance traveled by a hadronic particle be-
 1606 fore undergoing a nuclear interaction [9]. Figure 28 show the radiation lengths
 1607 in the layers of the [EM](#) calorimeter in the barrel region as well as the interaction
 1608 lengths for all calorimeters.

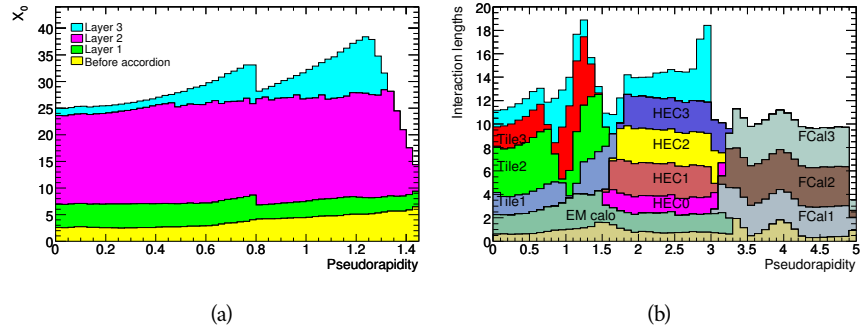


Figure 28: The depth of (a) the electromagnetic barrel calorimeter in radiation lengths and (b) all calorimeters in interaction lengths as a function of pseudorapidity.

1609 6.4.1 ELECTROMAGNETIC CALORIMETER

1610 The electromagnetic calorimeters use alternating layers of Liquid Argon and
1611 lead in an accordion shape. The accordion shape allows a construction that pro-
1612 vides complete coverage in the ϕ direction while also providing many alternat-
1613 ing layers for the a particle to pass through. The configuration is detailed in
1614 Figure 29. When an electron or photon passes through the lead, it produces an
1615 electromagnetic shower. The particles produced in those showers then pass into
1616 and ionize the Liquid Argon; the ions produced can then be collected by an elec-
1617 trode in the Liquid Argon layer to provide the actual energy measurement.

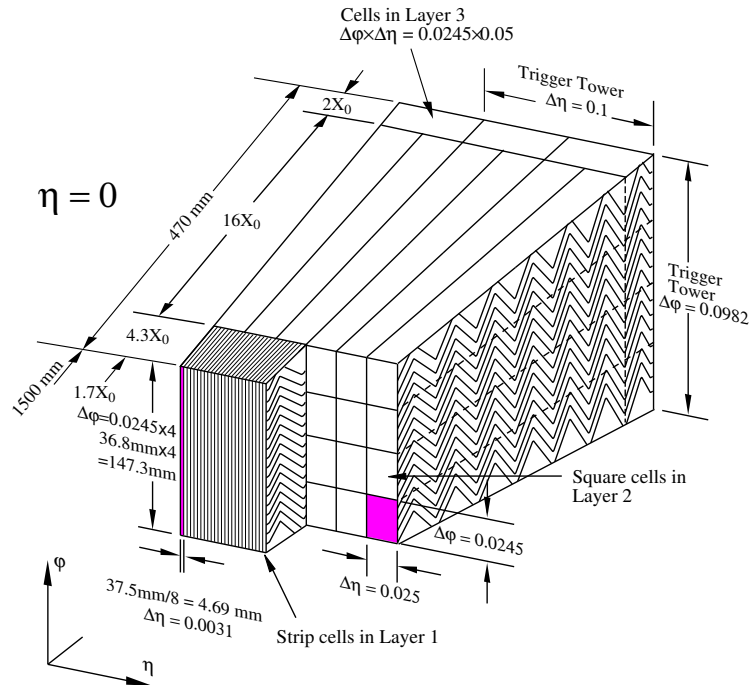


Figure 29: A schematic of the LAr calorimeter in the barrel region, highlighting the accordion structure.

1618 The barrel region is covered by a presampler and three separate sampling layers
 1619 with decreasing segmentation. The presampler is just a thin layer of Liquid
 1620 Argon which measures the energy of any electromagnetic showers which are
 1621 initiated before the particle reaches the calorimeter due to interactions with the
 1622 detector material. The first layer is the strip layer, which has fine segmentation
 1623 in η to enhance the identification of shower shapes and to provide a precise η
 1624 measurement for reconstructing photons and electrons. The strip layer has only
 1625 4 radiation lengths worth of material, and has a segmentation of $\Delta\eta = 0.003$
 1626 and $\Delta\phi = 0.1$. The second layer is also finely segmented, with a segmentation
 1627 of $\Delta\eta = 0.025$ and $\Delta\phi = 0.025$, and a thickness of $16 X_0$. This layer is designed
 1628 to contain an electromagnetic shower and to measure the majority of the energy
 1629 for photons and electrons. The third layer is only $2 X_0$ thick and measures the
 1630 energy of electromagnetic showers which leak out of the second layer, and helps
 1631 to separate electromagnetic showers from hadronic showers. The structure of
 1632 the LAr endcap calorimeter is similar except that the layers are arranged parallel
 1633 to the beampipe to measure energy deposits from high η particles.

1634 6.4.2 HADRONIC CALORIMETERS

1635 The hadronic calorimeters use a few different technologies to satisfy the resolu-
 1636 tion demands in the different areas of the detector, and together they cover the
 1637 region $|\eta| < 2.7$. In the barrel region, for $|\eta| < 1.7$, the hadronic calorimeters
 1638 are constructed of alternating tiles of steel and plastic scintillator. Like in the
 1639 electromagnetic calorimeter, the dense layer initiates a shower (in this case the
 1640 dense layer is the steel and the shower is hadronic) of particles which pass into
 1641 and ionize the following layer. The ionization in the plastic scintillator instead
 1642 produces a light signal proportional to the amount of ionization produced by the
 1643 shower, and this signal is measured using photomultipliers and provides the ac-
 1644 tual energy measurement. The construction of a tile in the calorimeter is shown
 1645 Figure 30, which highlights the alternating layers of steel and scintillator.

1646 This tile calorimeter, as well as the remaining hadronic calorimeters, have a
 1647 much coarser granularity than the electromagnetic calorimeters. The high gran-
 1648 ularity is not needed for an accurate energy measurement, and the hadronic
 1649 calorimeters are not designed to distinguish particle types like the electromag-
 1650 netic calorimeters. The tile granularity is approximately $\Delta\eta = 0.1$ and $\Delta\phi = 0.1$,
 1651 and the segmentation in depth and η is shown in Figure 31.

1652 The remaining hadronic calorimeters all use the same alternating, sampling
 1653 structure but with different active and inactive materials. The hadronic endcap
 1654 calorimeter covers the range of $1.5 < |\eta| < 3.2$ and uses an inactive layer of
 1655 copper and an active layer of Liquid Argon. The forward calorimeter covers the
 1656 range of $3.1 < |\eta| < 4.9$ and uses a dense matrix of copper and tungsten filled
 1657 with Liquid Argon.

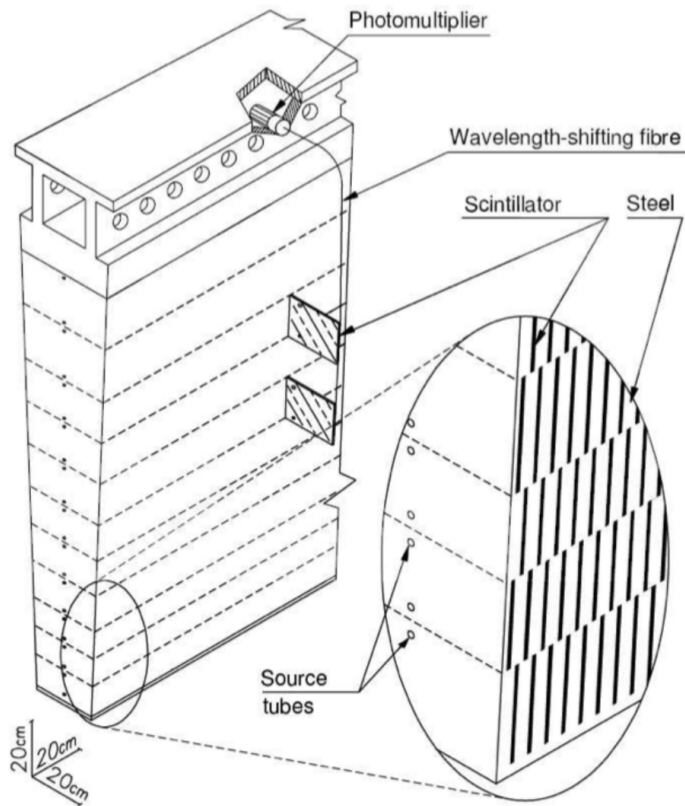


Figure 30: A schematic of a hadronic tile module which shows the alternating layers of steel and plastic scintillator.

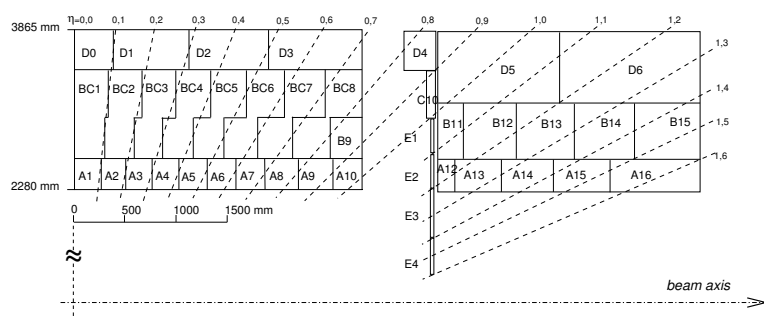


Figure 31: The segmentation in depth and η of the tile-calorimeter modules in the central (left) and extended (right) barrels.

1658 6.5 MUON SPECTROMETER

1659 Among SM particles, only muons and neutrinos consistently pass through the
 1660 calorimeters. Because the neutrinos are also electrically neutral, there is no fea-
 1661 sible option to measure them directly in ATLAS. The muons, on the other hand,
 1662 are charged and are thus already measured as a track in the inner detector. The
 1663 muon spectrometer provides a way to consistently identify muon tracks and also
 1664 a way to provide an additional measurement of their momentum.

1665 The muon spectrometer contains four subdetectors that cover the barrel and
 1666 endcap regions. In the barrel region, the muon spectrometer uses a combination
 1667 of Resistive Plate Chambers (RPCs) and MDTs to provide both a coarse, fast mea-
 1668 surement for triggering and a precise momentum measurement for offline event
 1669 reconstruction. Similarly, in the endcap region, the TGCs, MDTs, and CSCs allow
 1670 for both triggering and precise measurements. The CSCs are used only in the in-
 1671 nermost layer of the endcap region between $2.0 < |\eta| < 2.7$ where the particle
 1672 flux is too large for the MDTs to provide accurate measurements. The overall
 1673 layout of the muon systems are shown in the cut-away diagram in Figure 32,
 1674 and Figure 33 shows a precise schematic of the layout of each of the detecting
 1675 elements. The geometric arrangement shown provides consistent coverage for
 1676 muons produced up to $|\eta| < 2.7$, and takes full advantage of the bending of the
 1677 muons in the toroidal magnetic field, described in Section 6.2, to measure their
 1678 momentum. Figure 34 shows a cross-section of the arrangement of the muon
 1679 spectrometer in the barrel; the layers are divided into eight small and eight large
 1680 chambers that are overlapped to provide complete coverage in ϕ .

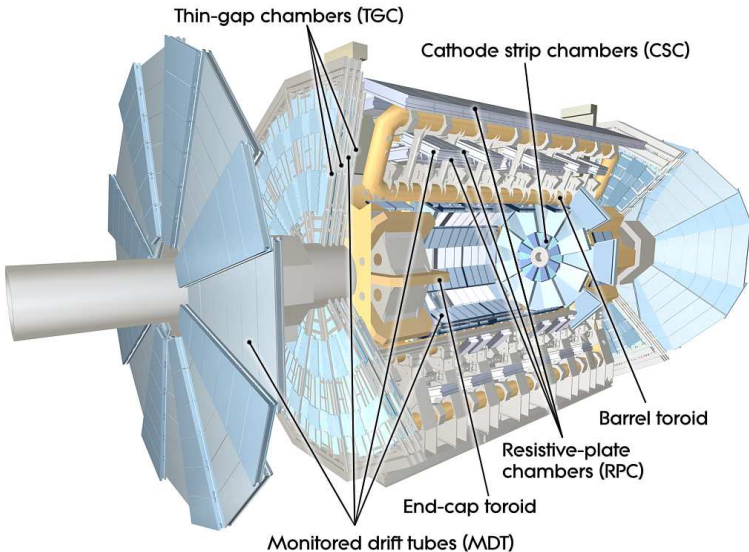


Figure 32: A cut-away diagram of the muon systems on ATLAS.

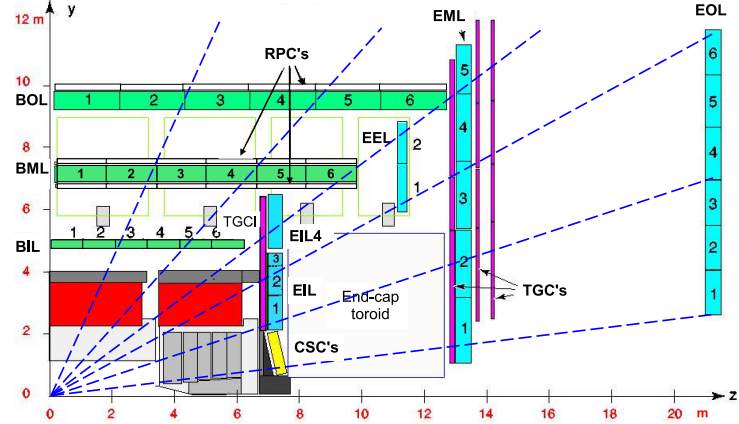


Figure 33: A quarter view of the muon spectrometer which highlights the layout of each of the detecting elements. The BOL, BML, BIL, EOL, EML, and EIL are all MDT elements, where the acronyms encode their positions.

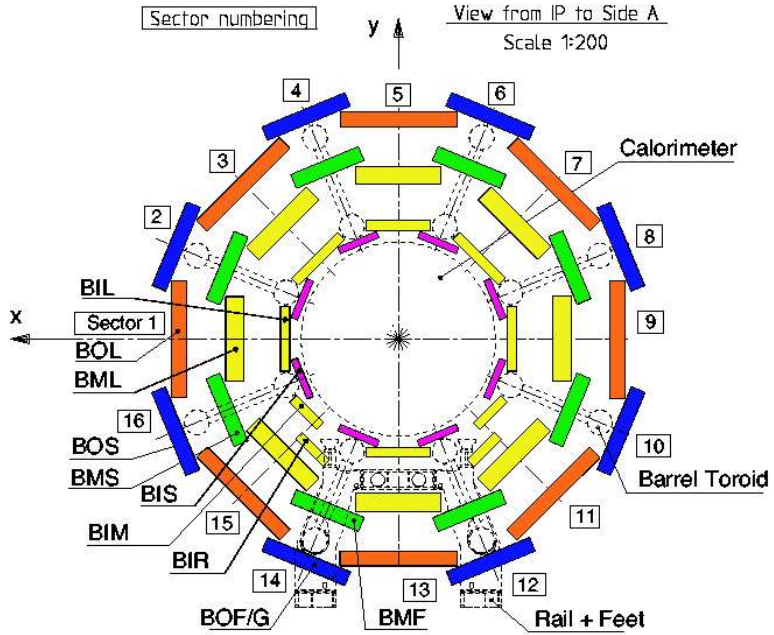


Figure 34: A schematic of the cross-section of the muon spectrometer in the barrel region.

1681 6.5.1 MONITORED DRIFT TUBE

1682 The momentum measurements in the barrel region are provided by three consecutive layers of MDT elements, located at approximately 5 m, 7 m, and 9 m from
 1683 the interaction point. Each of these layers is a composite of two multilayers of
 1684 drift tubes: two layers of three to four layers of tubes, as shown in Figure 35.
 1685 These aluminum tubes are 3 cm in diameter, with lengths between 0.9 and 6.2 m,
 1686 and are filled with a mixture of ArCO₂ kept at 3 bar absolute pressure. A central
 1687 tungsten-rhenium wire with a diameter of 50 μm runs along the length of the
 1688 tube, and is kept at a potential of 3080 V.

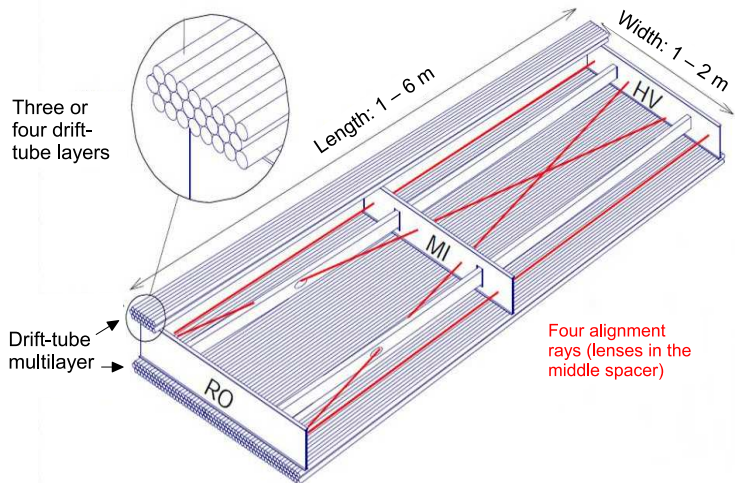


Figure 35: A schematic of a single MDT chamber, which shows the multilayers of drift tubes as well as the alignment system.

1690 A muon traversing these tubes ionizes the gas, and the ionization electrons
 1691 then drift in the electric field toward the central wire. Close to the wire, the
 1692 electric field is strong enough to cause the original ionization electrons to ionize
 1693 additional electrons, producing an avalanche that can be measured as a current
 1694 along the wire. The time of arrival of that current depends on how far the
 1695 muon entered from the wire, and can be used to achieve a position resolution of
 1696 80 μm in an individual tube. The combination of the measurements in the con-
 1697secutive layers of tubes improves this position resolution to 35 μm .

1698 To achieve a good resolution over the entire length of a muon track, the rel-
 1699 ative positions of the tubes of the muon spectrometer must be known to an ac-
 1700 curacy of 30 μm . This is achieved by an optical laser alignment system placed in
 1701 each of the individual chambers and throughout the cavern. These monitor any
 1702 changes in position or alignment due to effects like gravitational sag, tempera-
 1703 ture shifts, and the magnetic field. The configuration of the alignment system
 1704 within an individual chamber is also shown in Figure 34.

1705 6.5.2 RESISTIVE PLATE CHAMBER

1706 The **RPC** is the outermost detecting layer in the muon spectrometer in the barrel
 1707 region, and provides a fast measurement of the ϕ position of muons for trig-
 1708 gering. The speed of the measurement, with a time resolution of just a few
 1709 nanoseconds, requires a poor spatial resolution of approximately 1 cm. There
 1710 are three **RPCs** layers in the muon spectrometer, two located on either side of
 1711 the central **MDT** layer and one located outside the final **MDT** layer, as shown in
 1712 Figure 33. The **RPCs** consist of two layers of parallel plates filled with a gas mix-
 1713 ture of $C_2H_2F_4$. A muon passing through these systems ionizes the gas, like in
 1714 the **MDT**, which causes an avalanche of ionization electrons in the electric field
 1715 maintained between the plates. Metal strips on the outside of the chamber ca-
 1716 pacitively couple to the accumulated charge, and are read out to measure the η
 1717 and ϕ positions of the muon track.

1718 6.5.3 CATHODE STRIP CHAMBER

1719 The majority of the momentum measurements in the endcap region are provided
 1720 by the **MDTs**. In the most forward region of the muon spectrometer, between
 1721 $2.0 < \eta < 2.7$, the particle flux is very high due to contributions from low energy
 1722 photons and neutrons. The **MDT** can only sustain a hit rate of approximately 150
 1723 Hz/cm² because of limitations in the drift times of the gas and the capacity of
 1724 the readout electronics. The **CSCs** were designed to handle higher hit rates, up to
 1725 1000 Hz/cm², and provide the necessary coverage in that high flux region.

1726 The **CSC** consists of several multiwire proportional chambers, where the wires
 1727 are oriented in the radial direction out from the beampipe. There are eight large
 1728 and eight small chambers, arranged to partially overlap in the ϕ direction, as
 1729 shown in Figure 36. Like in the **MDT**, a muon traversing the system produces
 1730 ionization in the gas; here, however, the ionization is collected on a number of
 1731 wires. These wires couple to cathodes on the chambers which are segmented
 1732 into strips in two directions. The relative amount of charge on each of the neigh-
 1733 boring strips can be used to interpolate to the position of the muon in both η
 1734 and ϕ .

1735 6.5.4 THIN GAP CHAMBER

1736 Like in the barrel region, a separate, fast detector is required to provide position
 1737 measurements of muons for trigger in the endcap region. This is provided by
 1738 the **TGC** which consists of seven layers in the middle station of the endcap, two
 1739 doublet layers and one triplet layer, and a single doublet layer in the inner endcap
 1740 station. Figure 37 shows the arrangement of the triple and doublet layers of the
 1741 **TGCs**.

1742 Like the **CSCss**, the **TGCs** are multiwire proportional chambers with a wire-to-
 1743 cathode distance of 1.4 mm and a wire-to-wire distance of 1.8 mm. Readout
 1744 strips on the outside of the chambers run perpendicular to the wires, and couple
 1745 to the charge collected on the wires to provide a position measurement in the η

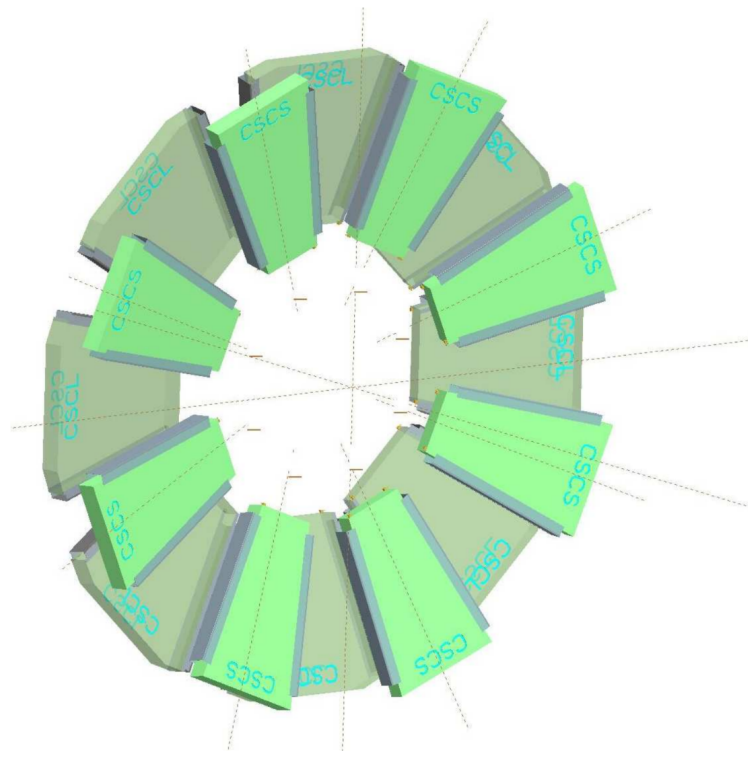


Figure 36: A schematic of the **CSC** endcap, showing the overlapping arrangement of the eight large and eight small chambers.

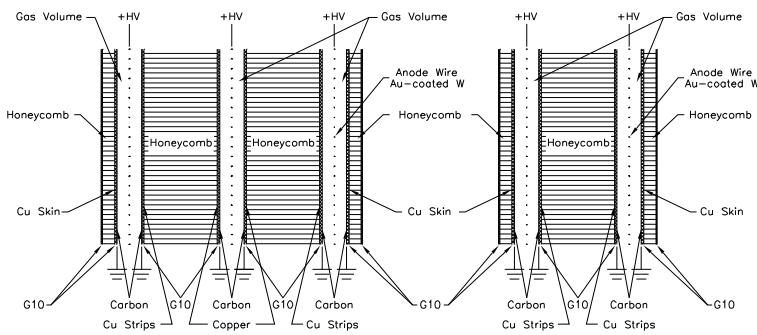


Figure 37: A schematic of the **TGC** doublet and triplet layers.

1746 direction. The current induced on the wires is also readout to provide a position
 1747 measurement in the ϕ direction. The high electric field and small wire-to-wire
 1748 distance give it the required good time resolution to be used for triggering events.

1749 6.6 TRIGGER

1750 It is not possible for the detector and the associated computing systems to record
 1751 the terabytes of data that the 40 MHz of proton-proton collisions produce every
 1752 second. Instead, a small fraction of these events are selected by the trigger sys-
 1753 tem to be recorded and later analyzed. Selecting interesting events at such a high
 1754 rate poses a significant challenge for the both the detector design and the imple-
 1755 mentation of a trigger decision and data acquisition system. The trigger must
 1756 balance the time needed to decide to keep an event, to avoid losing information,
 1757 with the filtering accuracy to consistently select a full menu of physics events
 1758 that can be used for the wide array of searches and measurements targeted by
 1759 [ATLAS](#).

1760 The [ATLAS](#) trigger system, as of Run 2, consists of two levels of decision mak-
 1761 ing. The first level, referred to as L1, is hardware based and uses inputs from
 1762 a subset of the detector elements to narrow the considered event rate from the
 1763 original 40 MHz down to 100 kHz. The 100 kHz rate is the maximal rate that
 1764 the event information can be transferred from the detector. The second level,
 1765 referred to as the [HLT](#), makes the final decisions on which events to keep for
 1766 analysis and selects a rate of around 1 kHz. The collection of selection criteria
 1767 used to make the L1 decisions feed into subsequent selection criteria in the [HLT](#),
 1768 and the set of these combinations of L1 and [HLT](#) criteria from the trigger menu
 1769 which defines exactly what events are recorded on [ATLAS](#). The entirety of the
 1770 trigger menu used for 2015 data collection is shown in Table 7, which summa-
 1771 rizes the selection requirements at both levels and additionally shows the peak
 1772 measured rates contributed by each.

1773 At L1, the trigger system uses information primarily from the calorimeters
 1774 and muon spectrometer to select high p_T jets, electrons, photons, and muons.
 1775 The electromagnetic calorimeter uses reduced granularity energy measurements
 1776 as well as isolation requirements to select electrons and photons. The hadronic
 1777 calorimeter also uses a combination of reduced granularity energy measurements
 1778 and isolation to select high momentum jets and hadronically decaying tau lept-
 1779 ons. The calorimeters are also used to provide triggers based on missing energy:
 1780 the coarse granularity energy measurements are used to calculate a directional
 1781 sum of energies and to trigger on a significant imbalance. Only the [RPCs](#) and [TGCs](#)
 1782 muon subdetectors contribute to the decision at L1, and are used to identify high
 1783 momentum muons. The contributions to the triggering rate of the various types
 1784 of L1 triggers are shown in Figure 38. The total rate is indicated in black and
 1785 is lower than the sum of individual rates because their is significant overlap be-
 1786 tween different trigger channels. The majority of the rate comes from lepton
 1787 and photon triggers.

1788 After an event is chosen by the L1 trigger, the detector measurements from the
 1789 bunch crossing which fired the trigger is read out from the front-end electronics

Trigger	Typical offline selection	Trigger Selection		Level-1 Peak Rate (kHz)	HLT Peak Rate (Hz)
		Level-1 (GeV)	HLT (GeV)	$L = 5 \times 10^{33} \text{ cm}^{-2}\text{s}^{-1}$	
Single leptons	Single iso μ , $p_T > 21$ GeV	15	20	7	130
	Single e , $p_T > 25$ GeV	20	24	18	139
	Single μ , $p_T > 42$ GeV	20	40	5	33
	Single τ , $p_T > 90$ GeV	60	80	2	41
Two leptons	Two μ 's, each $p_T > 11$ GeV	2×10	2×10	0.8	19
	Two μ 's, $p_T > 19, 10$ GeV	15	18, 8	7	18
	Two loose e 's, each $p_T > 15$ GeV	2×10	2×12	10	5
	One e & one μ , $p_T > 10, 26$ GeV	20 (μ)	7, 24	5	1
	One loose e & one μ , $p_T > 19, 15$ GeV	15, 10	17, 14	0.4	2
	Two τ 's, $p_T > 40, 30$ GeV	20, 12	35, 25	2	22
	One τ , one μ , $p_T > 30, 15$ GeV	12, 10 (+jets)	25, 14	0.5	10
Three leptons	One τ , one e , $p_T > 30, 19$ GeV	12, 15 (+jets)	25, 17	1	3.9
	Three loose e 's, $p_T > 19, 11, 11$ GeV	15, 2 \times 7	17, 2 \times 9	3	< 0.1
	Three μ 's, each $p_T > 8$ GeV	3 \times 6	3 \times 6	< 0.1	4
	Three μ 's, $p_T > 19, 2 \times 6$ GeV	15	18, 2 \times 4	7	2
One photon	Two loose γ 's, $p_T > 40, 30$ GeV	2×10 (μ 's)	$2 \times 10, 12$	0.8	0.2
	Two tight γ 's, $p_T > 25, 25$ GeV	$2 \times 8, 10$	$2 \times 12, 10$	0.3	< 0.1
Two photons	one γ , $p_T > 125$ GeV	22	120	8	20
	Two loose γ 's, $p_T > 40, 30$ GeV	2×15	35, 25	1.5	12
Single jet	Two tight γ 's, $p_T > 25, 25$ GeV	2×15	2×20	1.5	7
	Jet ($R = 0.4$), $p_T > 400$ GeV	100	360	0.9	18
E_T^{miss}	Jet ($R = 1.0$), $p_T > 400$ GeV	100	360	0.9	23
	$E_T^{\text{miss}} > 180$ GeV	50	70	0.7	55
Multi-jets	Four jets, each $p_T > 95$ GeV	3×40	4 \times 85	0.3	20
	Five jets, each $p_T > 70$ GeV	4×20	5 \times 60	0.4	15
	Six jets, each $p_T > 55$ GeV	4×15	6 \times 45	1.0	12
b -jets	One loose b , $p_T > 235$ GeV	100	225	0.9	35
	Two medium b 's, $p_T > 160, 60$ GeV	100	150, 50	0.9	9
	One b & three jets, each $p_T > 75$ GeV	3 \times 25	4 \times 65	0.9	11
	Two b & two jets, each $p_T > 45$ GeV	3 \times 25	4 \times 35	0.9	9
b -physics	Two μ 's, $p_T > 6, 4$ GeV plus dedicated b -physics selections	6, 4	6, 4	8	52
Total				70	1400

Table 7: The trigger menu for the 2015 data collection with $L = 5 \times 10^{33} \text{ cm}^{-2}\text{s}^{-1}$. Both the L1 and HLT selection requirements and their trigger rates are shown measured at the specified luminosity are shown. The typical offline selections represent a typical set of offline requirements imposed after the trigger in an analysis.

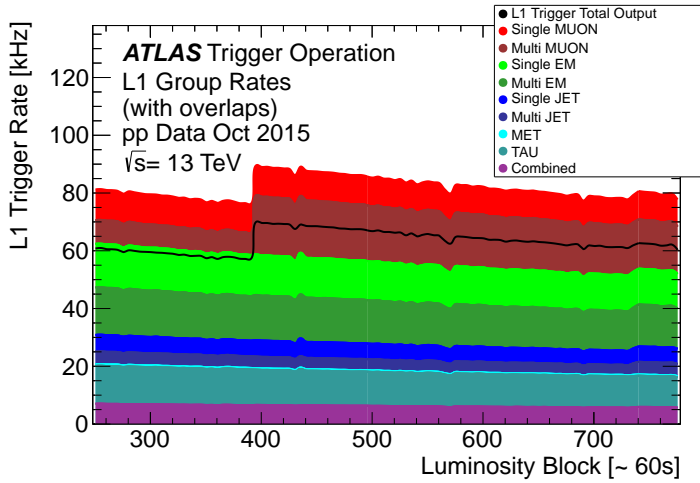


Figure 38: The L1 Trigger rate broken down into the types of triggers as a function of the luminosity block for the 2015 data collection period.

1790 and stored on read-out boards. This inclusive information is necessary to make
 1791 more the more precise event selections than is possible with the reduced infor-
 1792 mation at L1. The **HLT** then uses this information with software algorithms to
 1793 decide whether or not to permanently record the event. The L1 trigger also for-
 1794 wards which decision was made and Region of Interests (**RoIs**) to the **HLT**, which
 1795 allows the **HLT** to focus on particular algorithms and particular sections of the
 1796 detector to greatly improve the algorithmic selection speed. The additional in-
 1797 formation available to the **HLT** allows it to implement additional trigger targets,
 1798 such as identified jets from the decays of b-hadrons. The contributions to the
 1799 triggering rate of the various types of **HLT** triggers are shown in Figure 39.

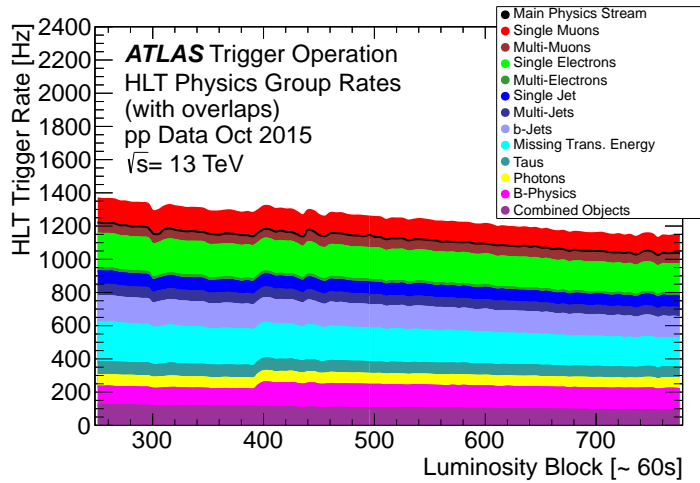


Figure 39: The HLT Trigger rate broken down into the types of triggers as a function of the luminosity block for the 2015 data collection period.

1800

1801 EVENT RECONSTRUCTION

1802 The ATLAS experiment combines measurements in the subdetectors to form a
 1803 cohesive picture of each physics event. The majority of particles that traverse
 1804 the detector leave behind some combination of ionization hits in the tracking
 1805 detectors or energy deposits in the calorimeters, and these measurements can
 1806 be used to reconstruct physical quantities like the particle's energy, momentum,
 1807 or trajectory. Even the type of the particle can be distinguished by comparing
 1808 the various ways that different species of stable particles interact with the subde-
 1809 tectors. Reconstruction is the process which takes the electronic outputs of the
 1810 detector and collects them into individual physics objects. The physics objects
 1811 summarize the properties of particles produced by the collision or subsequent
 1812 decays, either for individual isolated particles like leptons, or for a collection of
 1813 the cascade of products produced in the decay of an energetic hadron, called a
 1814 jet. These are the objects and quantities most often used in analysis to make
 1815 measurements of SM processes or to search for new physics.

1816 7.1 TRACKS AND VERTICES

1817 As described in Section 6.3, charged particles that traverse the inner detector
 1818 leave behind hits in the subdetectors. Each of these hits translates into a position
 1819 measurement along the trajectory of that particle, with position resolutions de-
 1820 pending on the subdetector that provided the measurement. Track reconstruc-
 1821 tion uses these position measurements to cluster hits in consecutive layers of
 1822 the detector into a trajectory consistent with a particle curving in a magnetic
 1823 field [12, 13]. The number of hits in the inner detector for each event makes
 1824 a combinatorial method completely infeasible: the algorithms that form tracks
 1825 must be significantly more intelligent so that event reconstruction does not ex-
 1826 haust computing resources.

1827 The first and primary algorithm employed in track reconstruction is called
 1828 the inside-out method, which begins with the assumption that the track orig-
 1829 inated from the interaction point. Its purpose is to identify primary particles,
 1830 those which originate in the proton-proton collisions and with a lifetime long
 1831 enough to reach the inner detector. Combinations of three space points are con-
 1832 sidered from measurements in the Pixel detector and the first layer of the SCT,
 1833 and form the seed for a track. The seed is then extrapolated into the SCT and
 1834 hits in each layer are considered to be added to the track using a combinatorial
 1835 Kalman filter [13]. After all of the SCT layers have been considered, tracks are
 1836 filtered to reduce ambiguities from other nearby tracks or from combinatorial
 1837 coincidences. Then the tracks are extended into the TRT in the same way. This
 1838 algorithm is how the hits are chosen to be incorporated into a single track. Once
 1839 the hits are collected, a fitting algorithm calculates the track parameters which

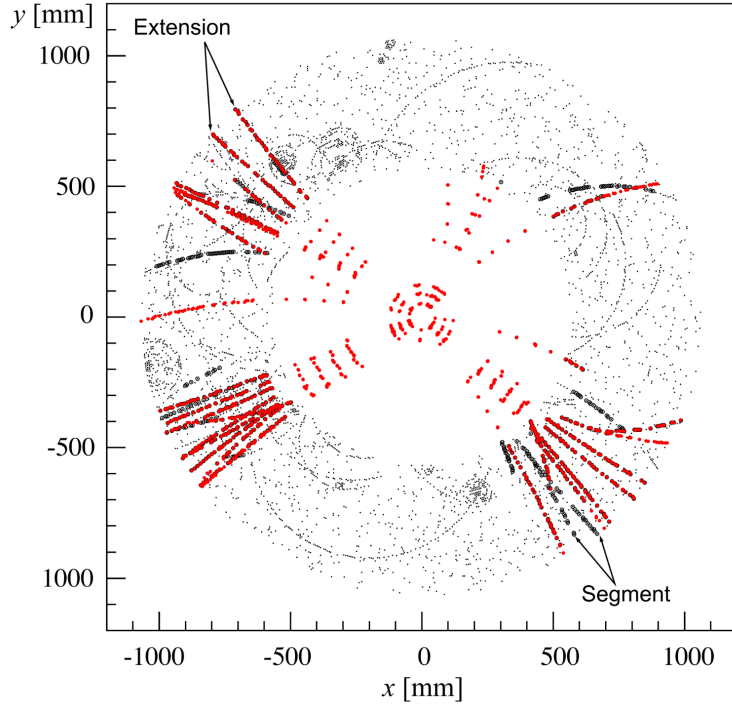


Figure 40: The x and y locations of the hits generated in a simulated $t\bar{t}$ event in the inner detector. The hits which belong to tracks formed using the inside-out algorithm are highlighted in red, while the hits which belong to tracks formed using the outside-in algorithm are circled in black.

best model the locations of the hits and their resolutions. Those parameters directly determine the direction and momentum of the particle which produced the track.

This inside-out algorithm is complemented by an outside-in algorithm, which is used to find tracks from secondary particles, those produced in the decays or interactions of the primary particles inside the detector. As the name indicates, the outside-in algorithm begins by seeding tracks in the outermost layers of the inner detector, in the TRT. The seed in this case is formed by a segment in the TRT, and the track is propagated backwards into the SCT before being refitted to use all the included points. Some tracks are found with TRT segments only, which can result from interactions with the detector following the SCT. Figure 40 shows an example of the geometry of tracks formed by both algorithms, where the hits belonging to tracks found using the inside-out algorithm are highlighted in red, and the hits belonging to the tracks found using the outside-in algorithm are circled in black. The figure highlights the presence of a large number of both primary and secondary tracks in a single event, as well as the overall large number of hits present in the inner detector.

The tracks resulting from these algorithms can be contaminated by nearby particles confusing the tracking algorithm in a high luminosity environment. For example, enough hits present in the inner detector can lead to fake tracks from combinations of hits from multiple individual tracks. Therefore, after the tracks are formed and fitted, additional quality requirements are imposed in

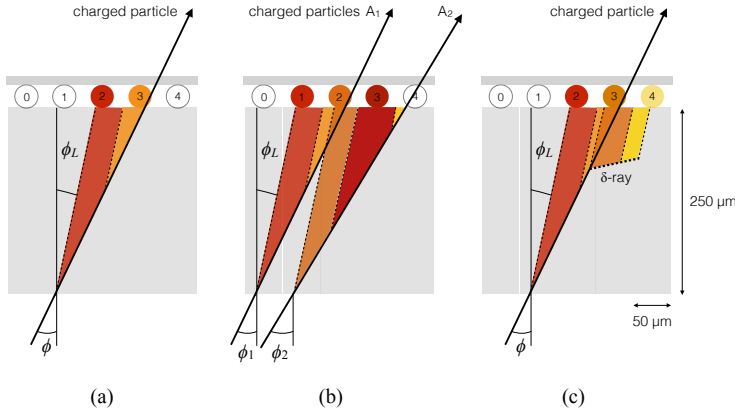


Figure 41: Examples of the clusters formed in a single layer of the pixel detector for (a) a single isolated particle, (b) two nearly-overlapping particles, and (c) a particle which emits a δ -ray [14].

order to reduce such backgrounds. Most tracking applications require at least seven silicon hits, that is, seven hits between the Pixel detector and [SCT](#). Then the tracks are required to have at most two holes in the Pixel detector, where holes are non-existing but expected measurements in a layer of the subdetector. If the missing hit corresponds to an inactive module, however, it is not counted as a hole but instead as a hit for tracking as the lack of a measurement is expected in that case.

7.1.1 PIXEL NEURAL NETWORK

The hits in the Pixel detector are not typically confined to a single pixel, but rather the charge is spread over several pixels per layer which are grouped together into clusters. The clustering of these pixels for isolated tracks is relatively straightforward, but complications can arise in the high track density environment where hits from multiple particles can overlap in a single cluster. Figure 41 shows examples of clusters generated by a single isolated particle, two nearly overlapping particles, and a particle which emits a δ -ray. A δ -ray is a secondary electron which is generated with enough energy to escape a significant distance away from the original particle and to generate additional ionization.

A series of neural-networks analyzes the shape of the clusters to determine how many particles produced the cluster and to find the positions of each of the particles within the cluster. These allow for an identification of clusters caused by more than one particle or by a particle that emits a δ -ray. In a high-density tracking environment, the multiple position outputs can be used as the locations of individual hits to allow reconstruction of tracks which almost overlap and with a much better separation than is possible without the splitting of individual clusters.

1887 7.1.2 PIXEL DE/DX

1888 A hit in the Pixel detector corresponds to the voltage generated from ionization
 1889 current rising above a threshold value that is tuned to consistently record the
 1890 passing of MIPs. A larger amount of charge deposited results in a larger voltage,
 1891 and a larger signal remains above the threshold for a longer period of time. The
 1892 time over threshold (`ToT`) is read out of the Pixel detector, and can be used to
 1893 provide a measurement of the charge deposited in each pixel. The charge mea-
 1894 surements from each of the pixels included in a pixel cluster are summed to form
 1895 one charge measurement per layer of the pixel detector. That charge measure-
 1896 ment, combined with the angle of incidence of the track and the known sizes of
 1897 each detector element, can be converted into a measurement of dE/dx , the ion-
 1898 ization energy deposited per unit distance, measured in $\text{MeVg}^{-1}\text{cm}^2$. The IBL
 1899 only has sixteen available values (4 bits) of `ToT` to readout, compared to the 256
 1900 available values (8 bits) in the remaining pixel layers. To help alleviate this lack
 1901 of range, the IBL also records if it is in overflow: when the ionization is sufficient
 1902 to generate a `ToT` above the largest value that can be recorded in the 4 bits.

1903 The measurements across multiple layers are combined to form an average
 1904 value of dE/dx for the track as a whole. To reduce the influence of the typical
 1905 long Landau tails of the distribution of dE/dx deposits [9], the average is calcu-
 1906 lated as a truncated mean. The value measured in the IBL is removed if it is in
 1907 overflow, as the measured value is not reliable in that case. If a track has five
 1908 measurements in the pixel detector, the two highest cluster values are removed.
 1909 If a track has two, three, or four measurements in the pixel detector, only the
 1910 single highest cluster value is removed. The remaining values are averaged to
 1911 form the pixel dE/dx .

1912 7.1.3 VERTEX RECONSTRUCTION

1913 A vertex represents the intersection of multiple tracks and corresponds to the
 1914 location of an interaction. If at least two charged particles result from the in-
 1915 teraction, the intersection of their resulting tracks reveals its position with high
 1916 precision. Vertices are divided into two groups, primary vertices which corre-
 1917 spond to the actual proton-proton collisions, and secondary vertices which cor-
 1918 respond to decays of short-lived particles or interactions with the detector. Pri-
 1919 mary vertices are particularly important, as they can provide a precise location
 1920 for the interaction which generated the observed particles. Understanding that
 1921 location is crucial in understanding the geometry of the event.

1922 Primary vertices are reconstructed by iteratively identifying seeds from re-
 1923 constructed tracks. Each track's extrapolated z position at the beamline forms a
 1924 seed, and nearby tracks are fitted using that position as a point along their trajec-
 1925 tory. The goodness of fit with that vertex is considered for each track, measured
 1926 in χ^2 . The final position of the vertex is determined by a fit to all of the con-
 1927 sidered tracks, where the contribution from each track is weighted according to
 1928 the χ^2 compatibility with that vertex. Any tracks from this procedure that are
 1929 displaced by more than 7σ from that vertex are removed from the fit and used

1930 to seed a new vertex. This procedure is iterated until no additional vertices can
 1931 be found.

1932 This procedure is typically performed twice. The first set of vertices is used
 1933 to fit a profile for the beamspot, which indicates the position of the intersection
 1934 of beams in that particular bunch crossing. The fitted beamspot then provides
 1935 a constraint for the second attempt to locate primary vertices, where both the
 1936 track fitting and seeding of vertices are required to be consistent with interac-
 1937 tions occurring within the beamspot.

1938 7.2 ELECTRONS AND PHOTONS

1939 Electrons are measured as both a charged particle track and energy deposits in
 1940 the electromagnetic calorimeter. Photons, on the other hand, leave energy de-
 1941 posits in the electromagnetic calorimeter but do not produce a corresponding
 1942 track. Because the electromagnetic interactions with the calorimeter of both
 1943 photons and electrons produces more photons and electrons, the behavior in the
 1944 calorimeter is very similar and there is significant overlap in the reconstruction
 1945 techniques for each.

1946 The reconstruction of a photon or an electron in the calorimeter is based on
 1947 clustering algorithms which identify groups of energy deposits [15]. For this
 1948 purpose, the entire electromagnetic calorimeter is subdivided into a grid of 200
 1949 by 256 towers in the η and ϕ directions, respectively, where the individual grid
 1950 units have a size of $\Delta\eta = 0.025$ and $\Delta\phi = 0.025$. These towers correspond to
 1951 individual cells in the middle, coarsest layer of the EM calorimeter, and in the
 1952 remaining layers the cells are grouped together cover the same area in $\eta - \phi$
 1953 space. The clustering begins by finding seeds with a sliding-window algorithm
 1954 based on the towers: a window of 3 by 5 towers is formed and translated until
 1955 the sum of the energy within the window is maximized. If that energy is above
 1956 2.5 GeV, then that region becomes a seed. The choice of 2.5 GeV was chosen to
 1957 compromise between maximizing reconstruction efficiency while minimizing
 1958 fake electron seeds from electronic noise or pileup. The seeds are rejected if the
 1959 energy measured in the hadronic calorimeter behind the seed is large, as this
 1960 typically indicates a hadron rather than an electron or photon.

1961 Next, the inner detector tracks within a cone of $\Delta R = 0.3$ are compared to
 1962 the location and energy of the seed. Tracks are matched to the cluster if the ex-
 1963 trapolation of the track to the energy-weighted center in the middle layer of the
 1964 EM calorimeter falls within $\Delta\phi < 0.2$ in the direction of the curvature of the
 1965 track or $\Delta\phi < 0.05$ in the direction opposite of the curvature of the track. If the
 1966 seed matches with a track that originated from a primary vertex, the combina-
 1967 tion of track and electromagnetic cluster is reconstructed as an electron. If the
 1968 seed matches with a track that did not originate from a primary vertex, then the
 1969 electromagnetic cluster is reconstructed as a converted photon. And if there is
 1970 no corresponding track in the inner detector, then the cluster is reconstructed
 1971 as a photon.

1972 After classification, the final clustering of the energy in the EM calorimeter
 1973 calorimeter is performed. The classification must be done first, as the expected

1974 size of the energy deposits in the calorimeter are different for electrons and photons.
 1975 In the barrel region, the final clusters for electrons are formed in rectangles
 1976 of 3 towers in the η -direction and 7 towers in the ϕ -direction. This asymmetric
 1977 window accounts for the curving of the produced charged particles only in the
 1978 ϕ direction. For photons, the size of the rectangle is 3 towers by 5 towers. In the
 1979 endcap region, all object types are clustered in rectangles of 5 towers by 5 tow-
 1980 ers, as the effect of the magnetic field curvature is less pronounced in this region.
 1981 The sum of the energies in these clusters provide the final energy measurement
 1982 for the electron or photon.

1983 7.2.1 PHOTON IDENTIFICATION

1984 The original requirement for constructing a photon cluster, a significant energy
 1985 deposit in the electromagnetic calorimeter without a corresponding track or en-
 1986 ergy deposits in the hadronic calorimeter, is already effective in identifying pho-
 1987 tons. However, there is a significant background for prompt photon production
 1988 from the decays of pions, $\pi^0 \rightarrow \gamma\gamma$. These can be identified using the shape of
 1989 the cluster in the narrow η granularity in the first layer of the [EM](#) calorimeter.

1990 7.2.2 ELECTRON IDENTIFICATION

1991 Prompt electrons have a number of backgrounds, such as secondary electrons
 1992 from hadron decays or misidentified hadronic jets, that can be rejected using ad-
 1993 ditional information from the [EM](#) calorimeter and the inner detector. The most
 1994 basic level of electron identification, referred to as Loose, makes requirements
 1995 on the shower shapes in the high granularity first layer of the [EM](#) calorimeter
 1996 as well as the quality of the inner detector track. It also requires a good match
 1997 between the track and the calorimeter energy deposits and a small fraction of
 1998 energy in the hadronic calorimeter behind the electromagnetic cluster. [ATLAS](#)
 1999 defines several additional working points, including Medium and Tight, which
 2000 provide progressively lower background rates for electrons by imposing addi-
 2001 tionally strict requirements on the above variables as well as new requirements
 2002 like the impact parameter of the inner detector track or the comparison of the
 2003 cluster energy to the momentum in the inner detector.

2004 7.3 MUONS

2005 Muons produced in [ATLAS](#) first traverse the inner detector and leave behind a
 2006 track as described in Section 7.1. The muon then passes through the calorimeter,
 2007 leaving behind a small, characteristic amount of energy, and then passes through
 2008 the muon spectrometer where it produces hits in the [MDTs](#) or [CSCs](#). Muon tracks
 2009 are formed from local segments of hits in each layer of the [MDTs](#) or [CSCs](#), and
 2010 then the final muon spectrometer track is formed by combining the two local
 2011 segments. When a track is reconstructed in both the inner detector and the muon
 2012 spectrometer, they are combined to form a combined muon.

2013 In a few regions of the detector, a muon may fail to leave behind both a com-
 2014 plete inner detector and muon system track. For a very small fraction of the
 2015 acceptance of the muon system, there is only one layer of muon chambers and a
 2016 global muon system track is not formed. In this case, as long as the track in the
 2017 inner detector exists and geometrically matches to a segment, a segment-tagged
 2018 muon is formed using momentum measurements from the inner detector. In
 2019 the region where the muon system has coverage but the inner detector does not,
 2020 $2.5 < |\eta| < 2.7$, a stand-alone muon is formed which uses only information
 2021 from the muon system. And for muons produced within one of the few holes in
 2022 the muon system, including $|\eta| < 0.1$, the characteristic energy deposits in the
 2023 calorimeter can be used to tag an inner detector track as a calo-tag muon. These
 2024 additional categories are used to achieve high efficiency over a larger range of
 2025 acceptance, but the combined muons are the most reliable.

2026 7.3.1 MUON IDENTIFICATION

2027 The various types of muons are incorporated into three working points: Loose,
 2028 Medium, and Tight, which reflect the increasing muon purity for each of the
 2029 selections definitions. Tight muons include only combined muons with a good
 2030 track fit quality and momentum resolution and at least two hits in a precision
 2031 muon system layer. Medium muons include those in tight as well as combined
 2032 muons with one precision hit and one precision hole, where hole is defined in
 2033 the same way as in Section 7.1. The medium working point also includes stand-
 2034 alone muons with $|\eta| > 2.5$ and at least two hits in precision layers. And finally
 2035 the loose working point includes both medium and tight muons, but additional
 2036 includes segment-tagged and calo-tagged muons in the region $|\eta| < 0.1$.

2037 7.4 JETS

2038 A jet does not directly correspond to a physical particle, unlike all of the recon-
 2039 structed objects described above, but instead tries to capture the conical cascade
 2040 of particles produced in the hadronization of a quark or gluon from the proton-
 2041 proton collision. The hadronization process creates a very large number of col-
 2042 limated particles, with a high enough density that individually reconstructing all
 2043 of the produced particles in the calorimeter is not possible within ATLAS. How-
 2044 ever most analyses are interested only in the kinematics of the particle which
 2045 produced the cascade, rather than the individual products. Therefore, jets are
 2046 a useful tool to measure the combined energy and direction of the ensemble of
 2047 products and thus represents the kinematics of the original. Jet algorithms are
 2048 very generic and can be used to group together a number of types of objects to
 2049 form aggregate representations. For example, truth particles in simulation can
 2050 be grouped in truth jets, or tracks from the inner detector can be grouped to-
 2051 gether to form track jets. This section, however, will focus on calorimeter jets
 2052 which take topoclusters of energy deposits in the calorimeter as inputs and pro-
 2053 duce a combined object which represents the energy measured by the calorime-
 2054 ter and the location where it was deposited.

2055 74.1 TOPOLOGICAL CLUSTERING

2056 Hadrons often deposit their energy into multiple individual cells in both the elec-
 2057 tromagnetic and hadronic calorimeters. The purpose of topological clustering is
 2058 to group cells in all three dimensions into clusters that represent a single energy
 2059 deposit. The procedure must be robust enough to reject noise fluctuations in
 2060 the cell energy measurements that can come from both electronic noise and ad-
 2061 dditional low energy particles produced in pileup activity. The background level
 2062 of calorimeter noise is called σ_{noise} , and is an important component of the topo-
 2063 logical clustering.

2064 The topological clusters are formed in a three step process called the 4-2-0
 2065 threshold scheme, which uses three energy thresholds to build up a cluster from
 2066 cells. First, any cells with a measured energy above $4\sigma_{\text{noise}}$ are identified as seed
 2067 cells. The cells adjacent to the seed cells with a measured energy above $2\sigma_{\text{noise}}$ are
 2068 called secondary cells. All of the cells which are adjacent to a secondary cell
 2069 with $E_{\text{cell}} > 2\sigma_{\text{noise}}$ are also labelled secondary cells. Tertiary cells are those
 2070 immediately adjacent to a seed or secondary cell with a measured energy above
 2071 zero. Adjacency in this sense is defined in three dimensions, cells are adjacent if
 2072 they are neighbors within a layer but also if they have the same $\eta - \phi$ coordinates
 2073 but are in adjacent layers or even in an adjacent layer in another calorimeter.

2074 From these definitions, clusters are built by resolving the seeds in order of
 2075 significance, the ratio $E_{\text{cell}}/\sigma_{\text{noise}}$. All adjacent secondary cells to the highest
 2076 significance seed are added to that seed's topocluster, and any of those cells which
 2077 would also have qualified as seeds are removed from the list of seeds. Once all
 2078 of the secondary cells have been added, the tertiary cells are then added to that
 2079 cluster as well. This procedure is then iterated until no seeds remain, forming
 2080 the first round of topoclusters.

2081 It is also useful to split topoclusters into multiples if local maxima are present
 2082 within the topocluster, as clusters produced by multiple nearby particles can
 2083 merge. The splitting process begins by finding local maxima cells in the middle
 2084 layer of the calorimeters with a minimum energy of 500 MeV and at least four
 2085 neighboring secondary cells. These requirements reduce the likelihood to split
 2086 a cluster due to random fluctuations, as the middle layers provide the most reli-
 2087 able energy measurements. Cells between two local maxima can then be shared
 2088 between two clusters to account for overlapping contributions from two parti-
 2089 cles. The energy sharing is weighted by the energy of each cluster as well as the
 2090 distance of the cell to the centroid of that cluster.

2091 The energies of all the cells in the cluster are then summed together to form
 2092 the energy of that cluster. The energy needs to be corrected for the various losses
 2093 expected in the calorimeter, as described in Section 6.4. The simplest correction,
 2094 scaling the measured energy by the sampling fraction, brings the cluster energies
 2095 to the EM scale. It is called the EM scale because it accurately describes the energy
 2096 of electromagnetic showers.

2097 Another scale is defined to improve accuracy for hadronic processes, the local
 2098 cluster weighted (LCW) scale, that helps to correct for the expected variations in
 2099 hadronic energy deposits. The LCW correction first determines if the shower is

hadronic or electromagnetic, based on the depth of the shower and the cluster energy density. For hadronic showers, the energy is corrected for calorimeter non-compensation, an effect which reduces the measured energy of hadronic showers because some of the energy goes into invisible processes like the break up of nuclei. All clusters are then corrected for energy that may be deposited in uninstrumented regions in that cluster's location in the calorimeter, and they are also corrected with an estimate of how much energy falls outside the extent of the cluster based on its shape and the deposit type.

7.4.2 JET ALGORITHMS

Using the topological clusters as inputs, a jet algorithm groups them together into a collection of adjacent energy deposits that is intended to correspond to a single process. Jet algorithms need a few key characteristics to be usable for physics analysis. First, the jets produced by the algorithm should have little dependence on the addition of soft particles to the event (infrared safety), as a negligible addition of energy should not significantly modify the event topology. Similarly, the jets produced by the algorithm should also not significantly depend on mostly collinear splitting of an input particle (collinear safety); that is, a single quark splitting into two nearly parallel quarks should not change the resulting jets, which are intended to capture only the properties of the aggregate and not those of individual particles. And finally the algorithm needs to be sufficiently simple and fast to be used for the large rate of collected proton-proton collisions on [ATLAS](#).

The most commonly used algorithm on [ATLAS](#) that satisfies these requirements is called the anti- k_t algorithm, and is discussed in further detail in Reference [16]. The anti- k_t , in brief, relies on iteratively combining the input objects that are closest together, where closest is defined by a particular distance metric, d_{ij} . The combinations stop when the closest remaining object is the beam itself, where the distance to the beam is called $d_{i,B}$. An entire class of algorithms follows this procedure with the following distance metrics

$$d_{ij} = \min(k_{ti}^{2p}, k_{tj}^{2p}) \frac{\Delta_{ij}^2}{R^2} \quad (18)$$

$$d_{i,B} = k_{ti}^{2p} \quad (19)$$

where $\Delta_{ij} = (y_i - y_j)^2 + (\phi_i - \phi_j)^2$, k_{ti} is the transverse momentum of the object, y is the rapidity, and p is a parameter of the algorithm. Anti- k_t is the particular case where $p = -1$, and is a choice that results in an algorithm that is both infrared and collinear safe.

The algorithm is repeated until there are no input objects remaining, which results in a series of jets. Each jet has a complete four momentum from the combination of its input clusters. The jet energies then need to be calibrated to attempt to match the energy of the object which produced the jet.

2137 74.3 JET ENERGY SCALE

2138 Though the [LCW](#) scheme attempts to correct the topoclusters to reflect the true
 2139 deposited energy, the correction does not fully account for energy lost within
 2140 the calorimeters. Because of these effects, the original reconstructed jet energy
 2141 does not reflect the true energy of the particle which initiated the jet. Therefore
 2142 it is necessary to additionally correct the reconstructed jet itself, in addition to
 2143 the corrections on the inputs. This correction is referred to as the [JES](#), which
 2144 combines several individual steps of calibration.

2145 The first calibration step corrections the direction of the jet to ensure that it
 2146 points back to the primary vertex. Next, the energy of the jet is corrected for
 2147 pileup by subtracting the expected contribution from pileup (measured in simu-
 2148 lation) based on the momentum, η , and area of the jet as well as the number of
 2149 reconstructed vertices and expected number of interactions per crossing. The
 2150 largest single correction is the absolute η and [JES](#) correction, where the jet energy
 2151 and pseudorapidity is corrected to attempt to match the energy and pseudorapid-
 2152 ity of the parton which produced it. This correction is measured in simulation
 2153 by comparing the reconstructed jet energies to the energy of the truth particle
 2154 which produced it. However the simulation is not relied on alone to estimate
 2155 this correction, and an additional step applies an additional energy correction
 2156 based on in-situ measurements in data. These corrections come from various
 2157 techniques which measure jet energies indirectly by balancing them with other,
 2158 well-measured objects. In the central region ($|\eta| < 1.2$), jets are balanced against
 2159 photons and the leptonic decays of Z bosons and high momentum jets ($p_T > 210$
 2160 GeV) are also balanced against multiple smaller jets in multijet events. Jets at
 2161 larger pseudorapidities, above $|\eta| = 1.2$, are calibrated by balancing with lower
 2162 pseudorapidity jets.

2163 These steps introduce a number of systematic uncertainties, referred to as
 2164 the [JES](#) uncertainty. The largest of these comes from the in-situ measurements,
 2165 which are statistically limited in measuring high momentum and high pseudora-
 2166 pidity jets. The total, fractional [JES](#) uncertainty is shown as a function of p_T in
 2167 Figure 42. The uncertainty falls to a minimum value of just over 1.0% around a
 2168 few hundred GeV, and rises again at high momentum because of the difficulty of
 2169 measuring jet balance in data above 2-3 TeV. The uncertainty is also minimized
 2170 at low $|\eta|$, and grows at large $|\eta|$ again where making in-situ measurements is
 2171 difficult. This technique does not actually provide a measurement of the uncer-
 2172 tainty for the highest energy jets, above 3 TeV, because there are not enough
 2173 measured data events to provide them. An alternative method for deriving the
 2174 [JES](#) and [JES](#) uncertainty that can be used even for very high p_T jets will be dis-
 2175 cussed in Chapter 9.

2176 7.5 MISSING TRANSVERSE ENERGY

2177 Among [SM](#) particles, only the neutrino cannot be directly measured in the [ATLAS](#)
 2178 detector. Because the neutrino carries neither electric nor color charge, it is very
 2179 unlikely to interact with the tracking detectors or the calorimeters, and instead

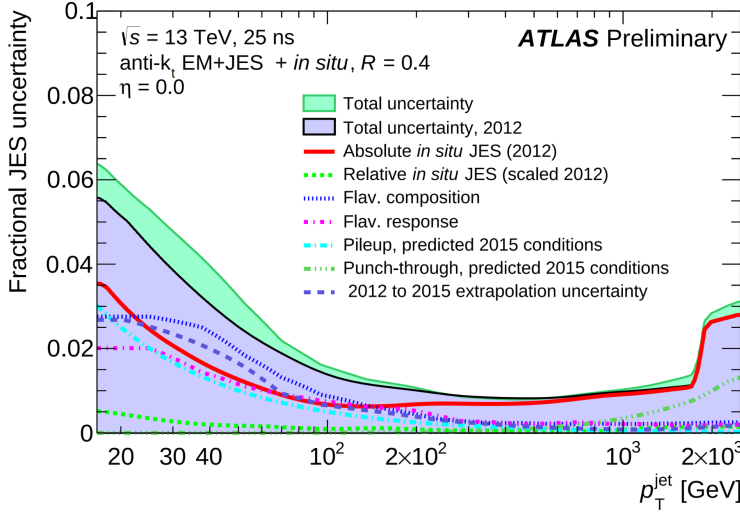


Figure 42: The total, fractional JES uncertainties estimated for 2015 data as a function of jet p_T .

passes through the detector completely unobserved. Some particles which have been conjectured to exist, like the LSP in many SUSY models, would also have the same behavior. Therefore, it is important for ATLAS to provide some way to assess the momentum carried away by a neutral, colorless particle. This can be accomplished through a measurement of missing energy in the transverse direction, or E_T^{miss} , which quantifies the momentum imbalance of the observed particles. From the conservation of momentum and the lack of the initial momentum in the transverse plane in the proton-proton collisions, any imbalance of momentum can be inferred to be carried away by an unmeasured particle.

E_T^{miss} is more precisely defined as the magnitude of the vector sum of the (p_x, p_y) components of each observed object's momentum. The definition is simple, but there can be significant complexity in defining the inputs. As of Run 2, ATLAS uses a common algorithmic approach to carefully calculate missing energy, but each analysis is free to define its own inputs. For the analysis discussed throughout this thesis, the missing energy inputs consist of the electrons, photons, muons, and jets discussed in the previous sections, in addition to a track-based soft term.

To produce the most precise measurement of E_T^{miss} , it is important to use the best representation of the momentum of each of the input objects, which can often be reconstructed as multiple different types in a single event. For example, an electron can be reconstructed separately as an electron (Section 7.2) and a jet (Section 7.4), but the electron representation has the highest precision for reconstructing the true electron momentum. To ensure no duplications in the E_T^{miss} definition, the inputs are collectively considered for overlap removal. Only the most precise object type is kept for objects that fall within a cone of $\Delta R < 0.2$ for pairs of electrons and jets and a cone of $\Delta R < 0.4$ for other pair types.

The fully reconstructed objects do not include all of the energy within the events, as some clusters do not enter into a jet and some tracks are not classified as electrons or muons. These momentum carried by these objects is accounted

2209 for in a soft-term, which tallies all of the energy carried by the particles too soft
2210 to form separate objects. The track soft term uses only tracking information to
2211 estimate the contribution of soft objects, and does so by vectorially summing the
2212 momentum of all well-reconstructed tracks with momentum above 400 MeV.

2213 All of these contributions together give a single E_T^{miss} value for a given event.
2214 The direction of that missing energy is taken as opposite the vector sum of all the
2215 constituents, to correspond to the momentum an invisible particle would have to
2216 have to make the event balanced. Depending on the context, this missing energy
2217 can be considered the energy of a neutrino or an LSP, with a large missing energy
2218 being a common signal criteria for searches for new physics.

2219

PART IV

2220

CALORIMETER RESPONSE

2221

You can put some informational part preamble text here.

8

2222

2223 RESPONSE MEASUREMENT WITH SINGLE HADRONS

2224 As discussed in Section 7.4, colored particles produced in collisions hadronize
2225 into jets of multiple hadrons. One approach to understanding jet energy mea-
2226 surements in the ATLAS calorimeters is to evaluate the calorimeter response to
2227 those individual hadrons; measurements of individual hadrons can be used to
2228 build up an understanding of the jets that they form. The redundancy of the
2229 momentum provided by the tracking system and the energy provided by the
2230 calorimeter provides an opportunity to study calorimeter response using real
2231 collisions, as described further in Section 8.2.

2232 Calorimeter response includes a number of physical effects that can be ex-
2233 tracted to provide insight into many aspects of jet modeling. First, many charged
2234 hadrons interact with the material of the detector prior to reaching the calorime-
2235 ters and thus do not deposit any energy. Comparing this effect in data and simu-
2236 lation is a powerful tool in validating the interactions of particles with the mate-
2237 rial of the detector and the model of the detector geometry in simulation, see Sec-
2238 tion 8.2.2. The particles which do reach the calorimeter deposit their energy into
2239 several adjacent cells, which are then clustered together. The energy of the clus-
2240 ter is then the total energy deposited by that particle. Comparing the response of
2241 hadrons in data to that of simulated hadrons provides a direct evaluation of the
2242 showering of hadronic particles and the energy deposited by particles in matter
2243 (Section 8.2.4).

2244 The above studies all use an inclusive selection of charged particles, which are
2245 comprised predominantly of pions, kaons, and (anti)protons. It is also possible to
2246 measure the response to various identified particle types separately to evaluate
2247 the simulated interactions of each particle, particularly at low energies where
2248 differences between species are very relevant. Pions and (anti)protons can be
2249 identified through decays of long-lived particles, in particular Λ , $\bar{\Lambda}$, and K_S^0 , and
2250 then used to measure response as described above. This is discussed in detail in
2251 Section 8.3.

2252 The results in this chapter use data collected at 7 and 8 TeV collected in 2010
2253 and 2012, respectively. Both are included as the calorimeter was repaired and
2254 recalibrated between those two data-taking periods. Both sets of data are com-
2255 pared to an updated simulation that includes new physics models provided by
2256 Geant4 [17] and improvements in the detector description [18, 19]. The present
2257 results are published in European Physical Journal C (EPJC) [20] and can be com-
2258 compared to a similar measurement performed in 2009 and 2010 [21], which used
2259 the previous version of the simulation framework [22].

2260 8.1 DATASET AND SIMULATION

2261 8.1.1 DATA SAMPLES

2262 The two datasets used in this chapter are taken from dedicated low-pileup runs
 2263 where the fraction of events with multiple interactions was negligible. These
 2264 datasets are used rather than those containing full-pileup events to facilitate mea-
 2265 surement of isolated hadrons. The 2012 dataset at $\sqrt{s} = 8$ TeV contains 8 mil-
 2266 lion events and corresponds to an integrated luminosity of 0.1 nb^{-1} . The 2010
 2267 dataset at $\sqrt{s} = 7$ TeV contains 3 million events and corresponds to an inte-
 2268 grated luminosity of 3.2 nb^{-1} . The latter dataset was also used for the 2010 re-
 2269 sults [21], but it has since been reanalyzed with an updated reconstruction in-
 2270 cluding the final, best understanding of the detector description for the material
 2271 and alignment from Run 1.

2272 8.1.2 SIMULATED SAMPLES

2273 The two datasets above are compared to simulated single-, double-, and non-
 2274 diffractive events generated with Pythia8 [23] using the A2 configuration of
 2275 hadronization [24] and the MSTW 2008 parton-distribution function set [25,
 2276 26]. The admixture of the single-, double-, and non-diffractive events uses the
 2277 default relative contributions from Pythia8. The conditions and energies for
 2278 the two simulations are chosen so that they match those of the corresponding
 2279 dataset.

2280 To evaluate the interaction of hadrons with detector material, the simulation
 2281 uses two different collections of hadronic physics models, called physics lists, in
 2282 Geant4 9.4 [27]. The first, QGSP_BERT, combines the Bertini intra-nuclear
 2283 cascade [28–30] below 9.9 GeV, a parametrized proton inelastic model from 9.5
 2284 to 25 GeV [31], and a quark-gluon string model above 12 GeV [32–36]. The
 2285 second, FTFP_BERT, combines the Bertini intra-nuclear cascade [28–30] below
 2286 5 GeV and the Fritiof model [37–40] above 4 GeV. In either list, Geant4 en-
 2287 forces a smooth transition between models where multiple models overlap.

2288 8.1.3 EVENT SELECTION

2289 The event selection for this study is minimal, as the only requirement is selecting
 2290 good-quality events with an isolated track. Such events are triggered by requir-
 2291 ing at least two hits in the minimum-bias trigger scintillators. After trigger, each
 2292 event is required to have exactly one reconstructed vertex, and that vertex is re-
 2293 quired to have four or more associated tracks.

2294 The particles which are selected for the response measurements are first iden-
 2295 tified as tracks in the inner detector. The tracks are required to have at least 500
 2296 MeV of transverse momentum. To ensure a reliable momentum measurement,
 2297 these tracks are required to have at least one hit in the pixel detector, six hits in
 2298 the SCT, and small longitudinal and transverse impact parameters with respect
 2299 to the primary vertex [21]. For the majority of the measurements in this chapter,

the track is additionally required to have 20 hits in the TRT, which significantly reduces the contribution from tracks which undergo nuclear interactions. This requirement and its effect is discussed in more detail in Section 8.2.5. In addition, tracks are rejected if there is any other reconstructed track which extrapolates to the calorimeter within a cone of $\Delta R = \sqrt{(\Delta\phi)^2 + (\Delta\eta)^2} < 0.4$. This requirement guarantees that the contamination of energy from nearby charged particles is negligible [21].

8.2 INCLUSIVE HADRON RESPONSE

The calorimeter response is more precisely defined as the ratio of the measured calorimeter energy to the true energy carried by the particle, although this true energy is unknown. For charged particles, however, the inner detector provides a very precise measurement of momentum (with uncertainty less than 1%) that can be used as a proxy for true energy. The ratio of the energy deposited by the charged particle in the calorimeter, E , to its momentum measured in the inner detector p , forms the calorimeter response measure called E/p . Though the distribution of E/p contains a number of physical features, this study focuses on the trends in two aggregated quantities: $\langle E/p \rangle$, the average of E/p for the selected tracks, and the zero fraction, the fraction of tracks with no associated energy in the calorimeter for those tracks.

The calorimeter energy assigned to a track is defined using clusters. The clusters are formed using a 4–2–0 algorithm [41] that begins with seeds requiring at least 4 times the average calorimeter cell noise. The neighboring cells with at least twice that noise threshold are then added to the cluster, and all bounding cells are then added with no requirement. This algorithm minimizes noise contributions through its seeding process, and including the bounding cells improves the energy resolution [42]. The clusters are associated to a given track if they fall within a cone of $\Delta R = 0.2$ of the extrapolated position of the track, which includes about 90% of the energy on average [21]. This construction is illustrated in Figure 43.

8.2.1 E/P DISTRIBUTION

The E/p distributions measured in both data and simulation are shown in Figure 44 for two example bins of track momentum and for tracks in the central region of the detector. These distributions show several important features of the E/p observable. The large content in the bin at $E = 0$ comes from tracks that have no associated cluster, which occurs due to interactions with detector material prior to reaching the calorimeter or the energy deposit being insufficiently large to generate a seed, and are discussed in Section 8.2.2. The small negative tail also comes from tracks that do not deposit any energy in the calorimeter but are randomly associated to a cluster with an energy below the noise threshold. The long positive tail above 1.0 comes from the contribution of neutral particles. Nearby neutral particles deposit (sometimes large) additional energy in the calorimeter but do not produce tracks in the inner detector, so they cannot be

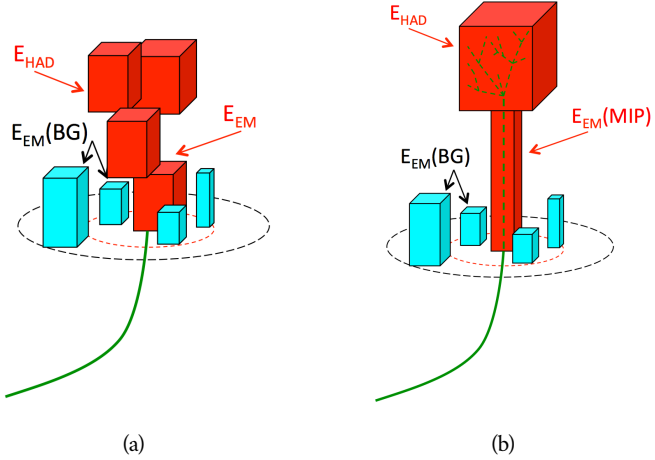


Figure 43: An illustration (a) of the E/p variable used throughout this paper. The red energy deposits come from the charged particle targeted for measurement, while the blue energy deposits are from nearby neutral particles and must be subtracted. The same diagram (b) for the neutral-background selection, described in Section 8.2.3.

2342 rejected by the track isolation requirement. Additionally the peak and mean of
 2343 the distribution falls below 1.0 because of the loss of energy not found within
 2344 the cone as well as the non-compensation of the calorimeter.

2345 The data and simulation share the same features, but the high and low tails
 2346 are significantly different. The simulated events tend to overestimate the con-
 2347 tribution of neutral particles to the long tail, an effect which can be isolated and
 2348 removed as discussed in Section 8.2.3. Additionally, the simulated clusters have
 2349 less noise on average, although this is a small effect on the overall response.

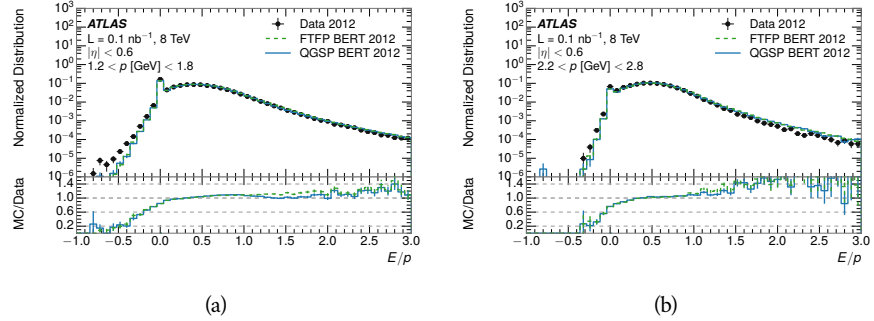


Figure 44: The E/p distribution and ratio of simulation to data for isolated tracks with
 (a) $|\eta| < 0.6$ and $1.2 < p/\text{GeV} < 1.8$ and (b) $|\eta| < 0.6$ and $2.2 < p/\text{GeV} < 2.8$.

2350 8.2.2 ZERO FRACTION

2351 The fraction of particles with no associated clusters, or similarly those with $E \leq$
 2352 0, reflects the modeling of both the detector geometry and hadronic interactions.

The zero fraction is expected to rise as the amount of material a particle traverses increases, while it is expected to decrease as the particle energy increases. This dependence can be seen in Figure 45, where the zero fraction in data and simulation is shown as a function of momentum and the amount of material measured in interaction lengths. The trends are similar between 2010 and 2012 and for positively and negatively charged particles. The zero fraction decreases with energy as expected. The absolute discrepancy in zero fraction decreases with momentum from 5% to less than 1%, but this becomes more pronounced in the ratio as the zero fraction shrinks quickly with increasing momentum. There is a small constant difference between the data and simulation in both interaction models that becomes more pronounced. The amount of material in the detector increases with η , which is used to obtain results for interaction lengths ranging between 0.1 and 0.65 λ . As the data and simulation have significant disagreement in the zero fraction over a number of interaction lengths, the difference must be primarily from the modeling of hadronic interactions with detector material and not just the detector geometry. Although two different hadronic interaction models are shown in the figure, they have very similar discrepancies to data because both use the same description (the BERT model) at low momentum.

8.2.3 NEUTRAL BACKGROUND SUBTRACTION

The isolation requirement on hadrons is only effective in removing an energy contribution from nearby charged particles. Nearby neutral particles, predominantly photons from π^0 decays, also add their energy to the calorimeter clusters, but mostly in the electromagnetic calorimeter. It is possible to measure this contribution, on average, using late-showering hadrons that minimally ionize in the electromagnetic calorimeter. Such particles are selected by requiring that they deposit less than 1.1 GeV in the EM calorimeter within a cone of $\Delta R < 0.1$ around the track. To ensure that these particles are well measured, they are additionally required to deposit between 40% and 90% of their energy in the hadronic calorimeter within the same cone.

These particles provide a clean sample to measure the nearby neutral background because they do not deposit energy in the area immediately surrounding them in the EM calorimeter, as shown in Figure 43. So, the energy deposits in the region $0.1 < \Delta R < 0.2$ can be attributed to neutral particles alone. To estimate the contribution to the whole cone considered for the response measurement, that energy is scaled by a geometric factor of 4/3. This quantity, $\langle E/p \rangle_{BG}$, measured in aggregate over a number of particles, gives the contribution to $\langle E/p \rangle$ from neutral particles in the EM calorimeter. Similar techniques were used in the individual layers of the hadronic calorimeters to show that the background from neutrals is negligible in those layers [21].

The distribution of this background estimate is shown in Figure 46 for data and simulation with the two different physics lists. The contribution from neutral particles falls from 0.1 at low momentum to around 0.03 for particles above 7 GeV. Although the simulation captures the overall trend, it significantly overestimates the neutral contribution for tracks with momentum between 2 and 8

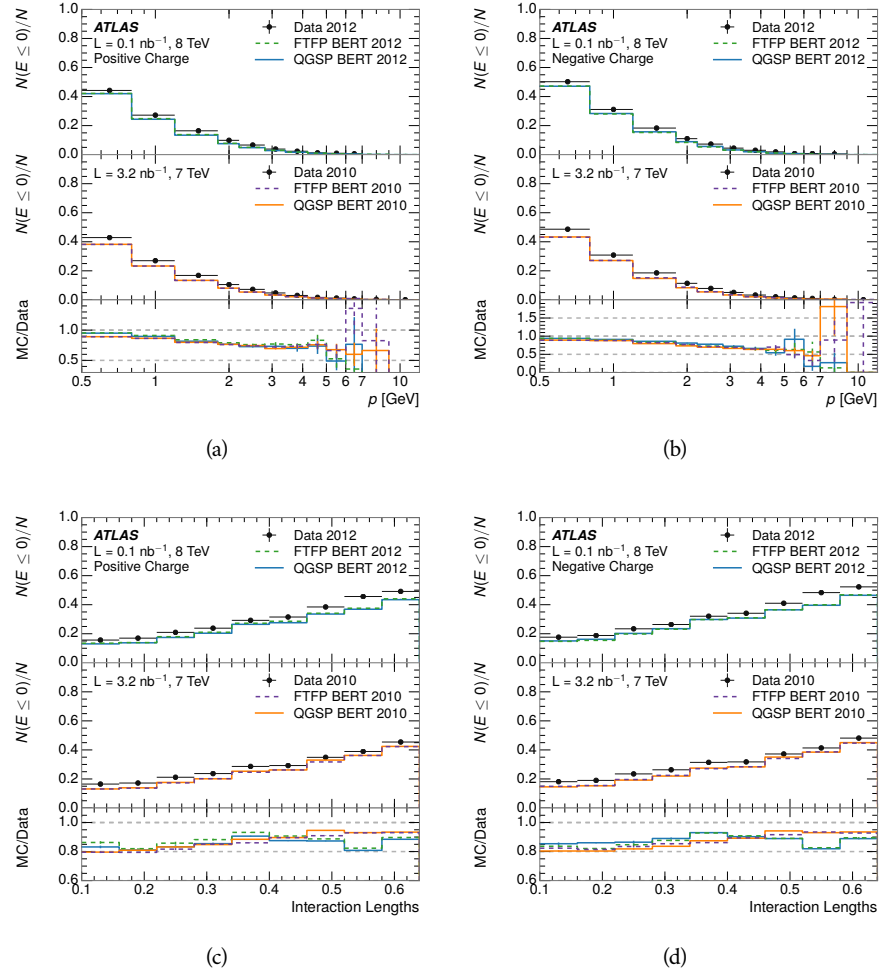


Figure 45: The fraction of tracks as a function (a, b) of momentum, (c, d) of interaction lengths with $E \leq 0$ for tracks with positive (on the left) and negative (on the right) charge.

2397 GeV. This effect was also seen in the tails of the E/p distributions in Figure 44.
 2398 This difference is likely due to modeling of coherent neutral particle radiation
 2399 in Pythia8 that overestimates the production of π^0 near the production of the
 2400 charged particles. The discrepancy does not depend on η and thus is unlikely to
 2401 be a mismodeling of the detector. This difference can be subtracted to form a
 2402 corrected average E/p , as in Section 8.2.4.

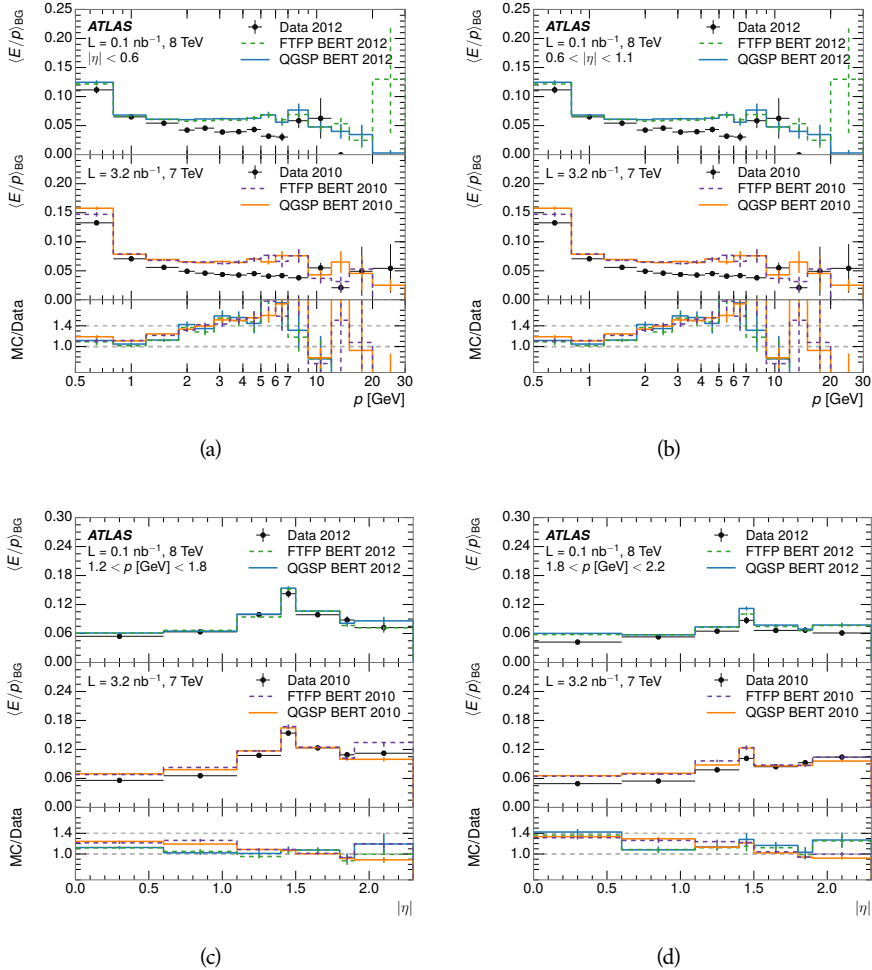


Figure 46: $\langle E/p \rangle_{BG}$ as a function of the track momentum for tracks with (a) $|\eta| < 0.6$,
 (b) $0.6 < |\eta| < 1.1$, and as a function of the track pseudorapidity for tracks
 with (c) $1.2 < p/\text{GeV} < 1.8$, (d) $1.8 < p/\text{GeV} < 2.2$.

2403 8.2.4 CORRECTED RESPONSE

2404 Figure 47 shows $\langle E/p \rangle_{COR}$ as a function of momentum for several bins of pseudo-
 2405 rapidity. This corrected $\langle E/p \rangle_{COR} \equiv \langle E/p \rangle - \langle E/p \rangle_{BG}$ measures the average
 2406 calorimeter response without the contamination of neutral particles. It is the
 2407 most direct measurement of calorimeter response in that it is the energy mea-
 2408 sured for fully isolated hadrons. The correction is performed separately in data
 2409 and simulation, so that the mismodeling of the neutral background in simulation

2410 is removed from the comparison of response. The simulation overestimates the
 2411 response at low momentum by about 5%, an effect that can be mostly attributed
 2412 to the underestimation of the zero fraction mentioned previously. For $|\eta| < 0.6$,
 2413 the data-simulation agreement has a larger discrepancy by about 5% for 2010
 2414 than 2012, although this is not reproduced in at higher pseudorapidity.

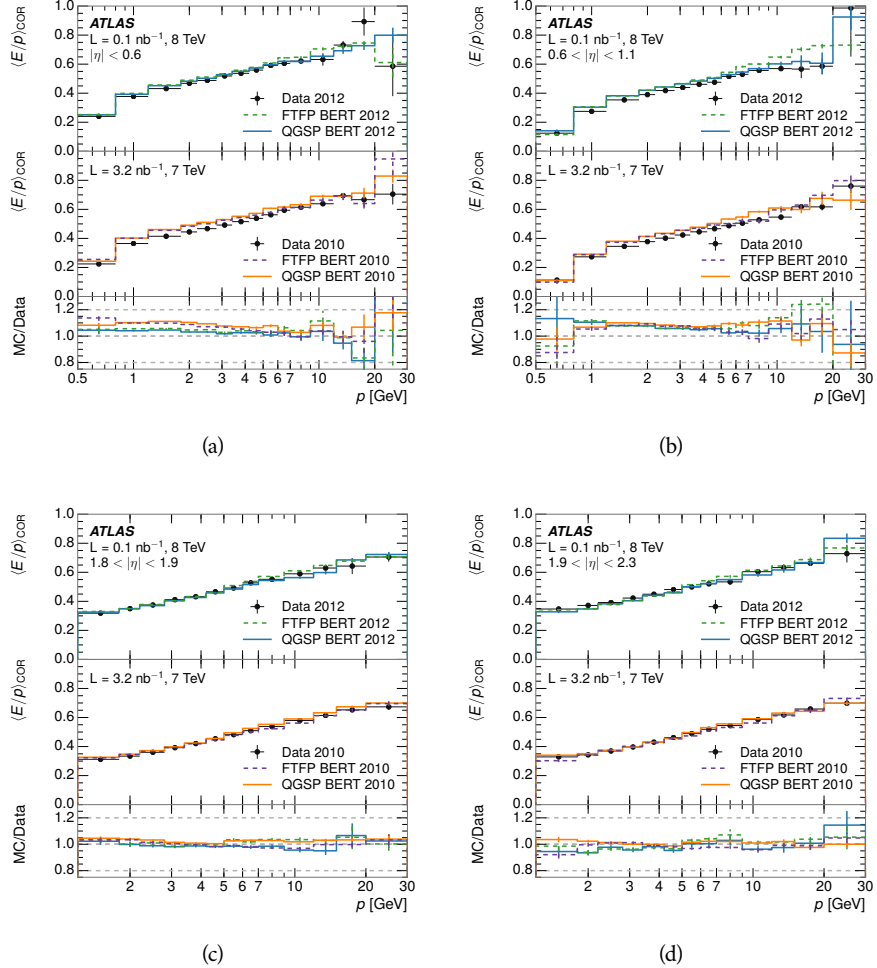


Figure 47: $\langle E/p \rangle_{\text{COR}}$ as a function of track momentum, for tracks with (a) $|\eta| < 0.6$, (b) $0.6 < |\eta| < 1.1$, (c) $1.8 < |\eta| < 1.9$, and (d) $1.9 < |\eta| < 2.3$.

2415 The response measurement above used topological clustering at the EM scale,
 2416 that is clusters were formed to measure energy but no corrections were applied
 2417 to correct for expected effects like energy lost outside of the cluster or in unin-
 2418 strumented material. It is also interesting to measure $\langle E/p \rangle_{\text{COR}}$ using LCW en-
 2419 ergies, which accounts for those effects by calibrating the energy based on the
 2420 properties of the cluster such as energy density and depth in the calorimeter.
 2421 Figure 48 shows these distributions for tracks with zero or more clusters and
 2422 separately for tracks with one or more clusters. The calibration moves the mean
 2423 value of $\langle E/p \rangle_{\text{COR}}$ significantly closer to 1.0 as desired. The agreement between
 2424 data and simulation improves noticeably when at least one cluster is required, as
 2425 this removes the contribution from the mismodeling of the zero fraction. The

good agreement in that case again demonstrates that the difference in $\langle E/p \rangle_{\text{COR}}$ between data and simulation is caused predominantly by the difference in zero fraction.

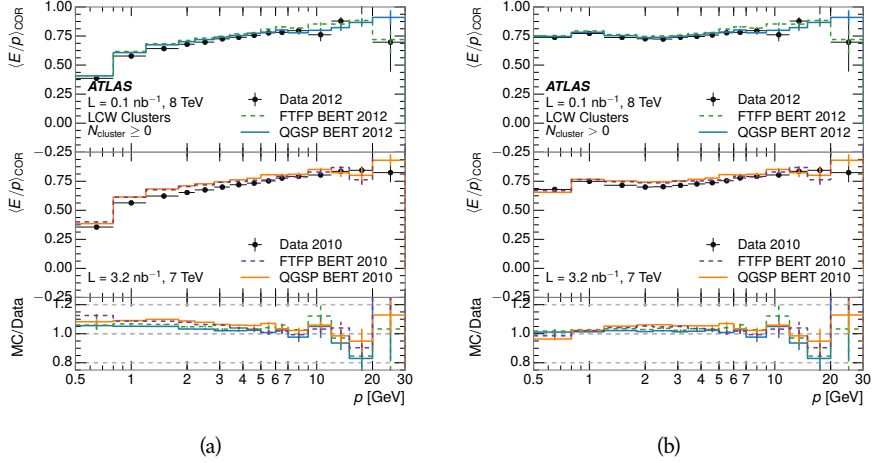


Figure 48: $\langle E/p \rangle_{\text{COR}}$ calculated using LCW-calibrated topological clusters as a function of track momentum for tracks with (a) zero or more associated topological clusters or (b) one or more associated topological clusters.

8.2.5 ADDITIONAL STUDIES

As has been seen in several measurements in previous sections, the simulation does not correctly model the chance of a low momentum hadron to reach the calorimeter. Because of the consistent discrepancy across pseudorapidity and interaction lengths, this can be best explained by incomplete understanding of hadronic interactions with the detector [20]. For example, a hadron that scatters off of a nucleus in the inner detector can be deflected through a significant angle and not reach the expected location in the calorimeter. In addition, these interactions can produce secondary particles that are difficult to model.

The requirement used throughout the previous sections on the number of hits in the TRT reduces these effects by preferentially selecting tracks that do not undergo nuclear interactions. It is interesting to check how well the simulation models tracks with low numbers of TRT hits, which selects tracks that are more likely to have undergone a hadronic interaction. Figure 49 compares the distributions with $N_{\text{TRT}} < 20$ to $N_{\text{TRT}} > 20$ for real and simulated particles. As expected, the tracks with fewer hits are poorly modeled in the simulation as $\langle E/p \rangle_{\text{COR}}$ differs by as much as 25% at low momentum.

Another interesting aspect of the simulation is the description of antiprotons at low momentum, where QGSP_BERT and FTFP_BERT have significant differences. This can be seen to have an effect in the inclusive response measurement when separated into positive and negative charge. The $\langle E/p \rangle_{\text{COR}}$ distributions for positive and negative particles are shown in Figure 50, where a small difference between QGSP_BERT and FTFP_BERT can be seen in the distribution for

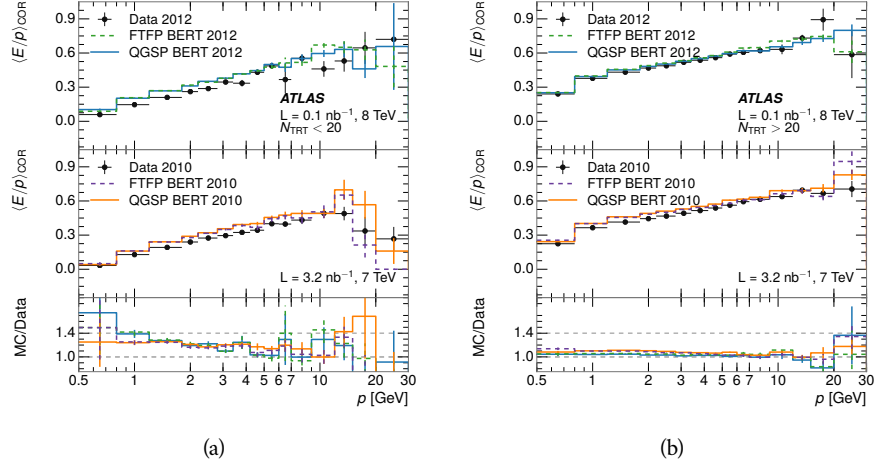


Figure 49: Comparison of the $\langle E/p \rangle_{\text{COR}}$ for tracks with (a) less than and (b) greater than 20 hits in the TRT.

negative tracks. This is demonstrated more clearly in Figure 51, which shows the E/p distribution in the two simulations separated by charge. There is a clear difference around $E/p > 1.0$, which can be explained by the additional energy deposited by the annihilation of the antiproton in the calorimeter that is modeled well only in FTFP_BERT. This is also explored with data using identified antiprotons in Section 8.3.

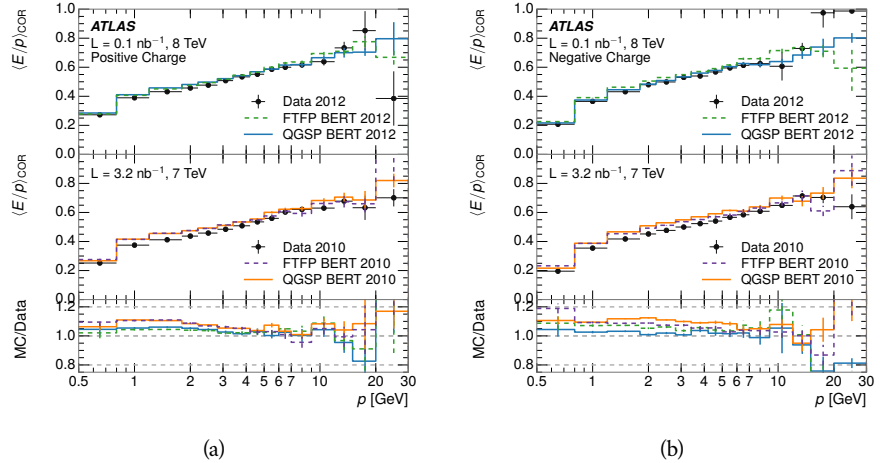


Figure 50: Comparison of the $\langle E/p \rangle_{\text{COR}}$ for (a) positive and (b) negative tracks as a function of track momentum for tracks with $|\eta| < 0.6$.

The $\langle E/p \rangle$ results in previous sections have considered the electromagnetic and hadronic calorimeters together as a single energy measurement, to emphasize the total energy deposited for a given particle. However, the deposits in each calorimeter are available separately and $\langle E/p \rangle$ can be constructed for each layer. As the layers are composed of different materials and are modeled separately in the detector geometry, confirmation that the simulation matches the data well

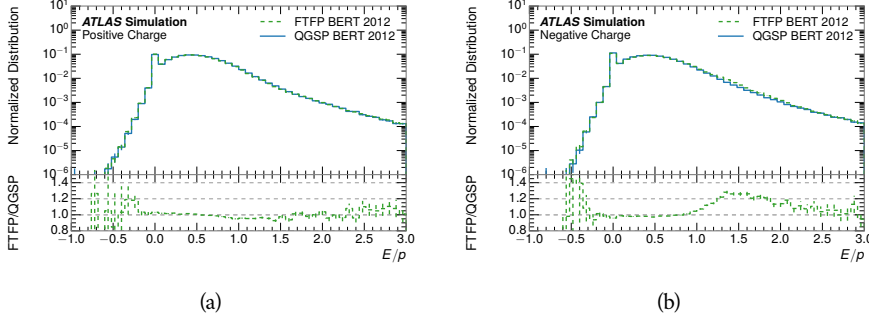


Figure 51: Comparison of the E/p distributions for (a) positive and (b) negative tracks with $0.8 < p/\text{GeV} < 1.2$ and $|\eta| < 0.6$, in simulation with the FTFP_BERT and QGSP_BERT physics lists.

in each layer adds confidence in both the description of hadronic interactions with the two different materials and also the geometric description of each.

The technique discussed in Section 8.2.3 for selecting MIPs in the electromagnetic calorimeter is also useful in studying deposits in the hadronic calorimeter. Those MIPs deposit almost all of their energy exclusively in the hadronic calorimeter. Figure 52 shows $\langle E/p \rangle_{\text{RAW}}^{\text{Had}}$, where RAW indicates that no correction has been applied for neutral backgrounds and Had indicates that only clusters for the hadronic calorimeter are included. The RAW and COR versions of $\langle E/p \rangle$ in this case are the same, as the neutral background is negligible in that calorimeter layer. The distributions are shown both for the original EM scale calibration and after LCW calibration. The data and simulation agree very well in this comparison, except in the lowest momentum bin which has 5% discrepancy that has already been seen in similar measurements.

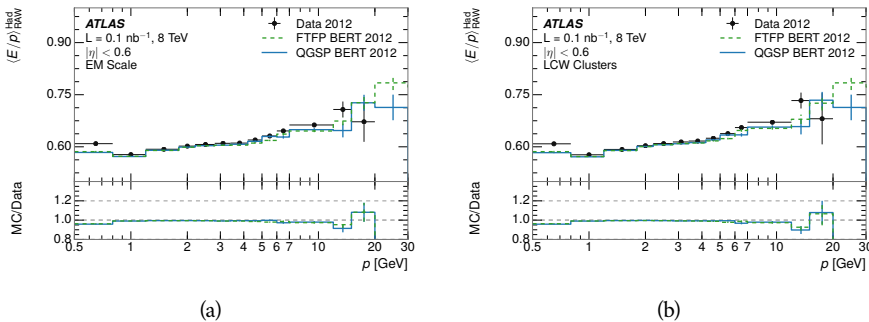


Figure 52: Comparison of the response of the hadronic calorimeter as a function of track momentum (a) at the EM-scale and (b) after the LCW calibration.

A similar comparison can be made in the electromagnetic calorimeter by selecting particles which have no associated energy in the hadronic calorimeter. These results are measured in terms of $\langle E/p \rangle_{\text{COR}}^{\text{EM}}$, where EM designates that only clusters in the electromagnetic calorimeter are included and COR designates that the neutral background is subtracted as the neutral background is present in this case. Figure 53 shows the analogous comparisons to Figure 52 in

2483 the electromagnetic calorimeter. In this case the disagreement between data and
 2484 simulation is more pronounced, with discrepancies as high as 5% over a larger
 2485 range of momenta. This level of discrepancy indicates that the description of
 2486 the electromagnetic calorimeter is actually the dominant source of discrepancy
 2487 in the combined distributions in Section 8.2.4.

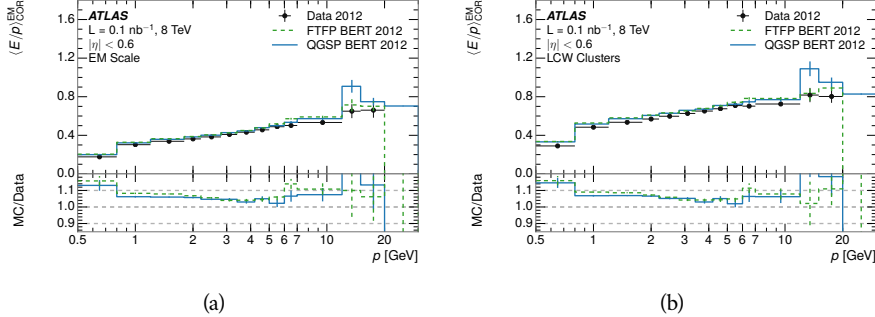


Figure 53: Comparison of the response of the EM calorimeter as a function of track momentum (a) at the EM-scale and (b) with the LCW calibration.

2488 **NOTE: There are more studies that I skipped for brevity that could be in-**
 2489 **cluded if interesting. E/p at different cluster threshold settings, E/p with**
 2490 **pileup, E/p with cells. I also left out a lot of eta bins that appear in the**
 2491 **paper so that this section didn't turn into 20 pages of plots.**

2492 8.3 IDENTIFIED PARTICLE RESPONSE

2493 The inclusive response measurement for hadrons can be augmented by measur-
 2494 ing the response for specific particle species. The simulation models each parti-
 2495 cle type separately, and understanding the properties of each is important in con-
 2496 straining the uncertainty on jets. In order to select and measure specific hadrons,
 2497 this section relies on the displaced decays of long-lived particles. Such decays
 2498 can be identified by reconstructing secondary vertices with a requirement on
 2499 mass. In particular, Λ , $\bar{\Lambda}$, and K_S^0 can be used to select a pure sample of protons,
 2500 antiprotons, and pions, respectively.

2501 8.3.1 DECAY RECONSTRUCTION

2502 The measurement of response for identified particles uses the same selection as
 2503 for inclusive particles (Section 8.1.3) with a few additions. Each event used is
 2504 required to have at least one secondary vertex, and the tracks are required to
 2505 match to that vertex rather than the primary vertex. Pions are selected from
 2506 decays of $K_S^0 \rightarrow \pi^+ \pi^-$, which is the dominant decay for K_S^0 to charged particles.
 2507 Protons are selected from decays of $\Lambda \rightarrow \pi^- p$ and antiprotons from $\bar{\Lambda} \rightarrow \pi^+ \bar{p}$,
 2508 which are similarly the dominant decays of Λ and $\bar{\Lambda}$ to charged particles. The
 2509 species of parent hadron in these decays is determined by reconstructing the
 2510 mass of the tracks associated to the secondary vertex. The sign of the higher

momentum decay particle can distinguish between Λ and $\bar{\Lambda}$, which of course have the same mass, as the proton or antiproton is kinematically favored to have higher momentum. Examples of the reconstructed masses used to select these decays are shown in Figure 54.

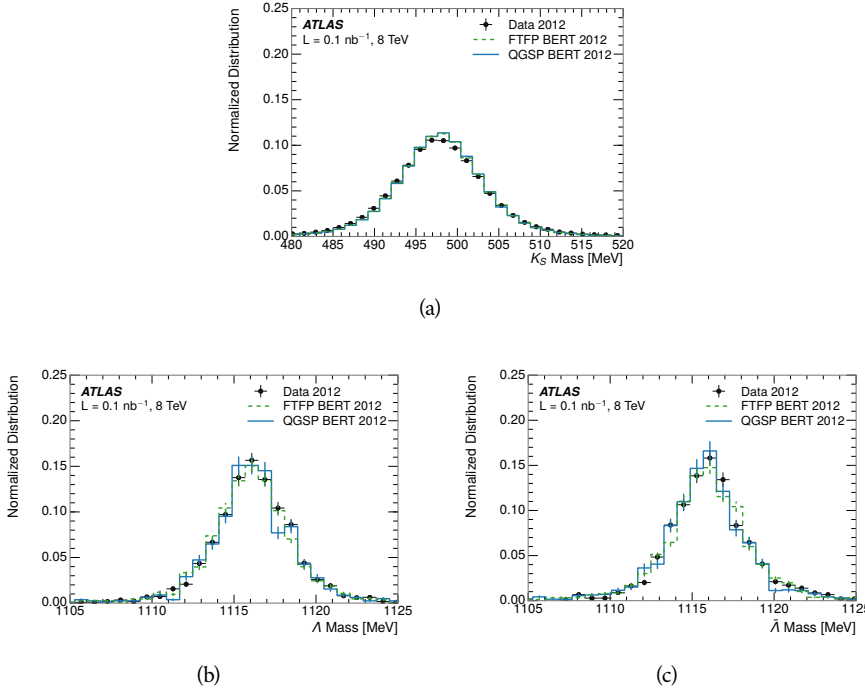


Figure 54: The reconstructed mass peaks of (a) K_S^0 , (b) Λ , and (c) $\bar{\Lambda}$ candidates.

The dominant backgrounds for the identified particle decays are nuclear interactions and combinatoric sources. These are suppressed by the kinematic requirements on the tracks as well as an additional veto which removes candidates that are consistent with both a Λ or $\bar{\Lambda}$ and a K_S^0 hypothesis, which is possible because of the different assumptions on particle mass in each case [21]. After these requirements, the backgrounds are found to be negligible compared to the statistical errors on these measurements.

8.3.2 IDENTIFIED RESPONSE

With these techniques the E/p distributions are extracted in data and simulation for each particle species and shown in Figure 55. These distributions are shown for a particular bin of E_a ($2.2 < E_a/\text{GeV} < 2.8$), rather than p . E_a is the energy available to be deposited in the calorimeter: for pions $E_a = \sqrt{p^2 + m^2}$, for protons $E_a = \sqrt{p^2 + m^2} - m$, and for antiprotons $E_a = \sqrt{p^2 + m^2} + m$. The features of the E/p distributions are similar to the inclusive case. There is a small negative tail from noise and a large fraction of tracks with zero energy from particles which do not reach the calorimeter. The long positive tail is noticeably more pronounced for antiprotons because of the additional energy generated by the annihilation in addition to the neutral background.

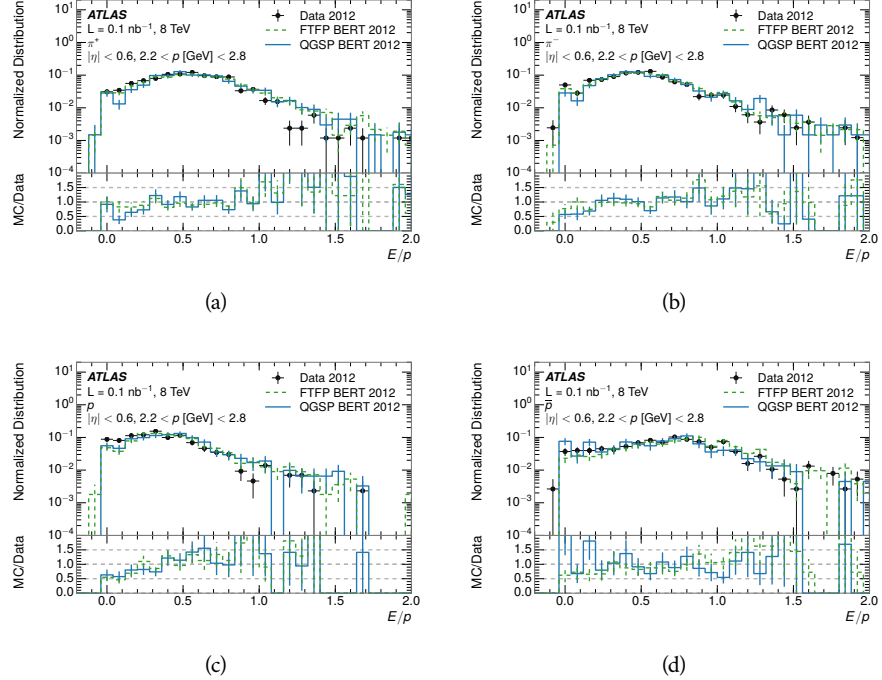


Figure 55: The E/p distribution for isolated (a) π^+ , (b) π^- , (c) proton, and (d) anti-proton tracks.

2533 The zero fraction is further explored in Figure 56 for pions and protons in data
 2534 and simulation. The simulation consistently underestimates the zero fraction
 2535 independent of particle species, which implies that this discrepancy is not caused
 2536 by the model of a particular species but rather a feature common to all.

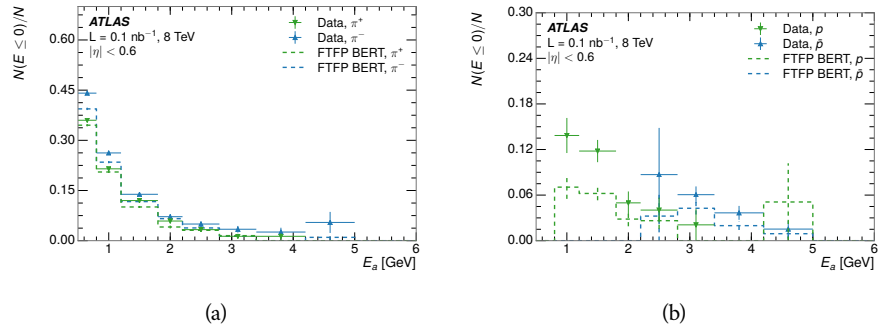


Figure 56: The fraction of tracks with $E \leq 0$ for identified (a) π^+ and π^- , and (b) proton and anti-proton tracks

2537 It is also interesting to compare the response between the different particle
 2538 species. One approach to do this is to measure the difference in $\langle E/p \rangle$ between
 2539 two types, which has the advantage of removing the neutral background. These
 2540 differences are shown in various combinations in Figure 57. The response for
 2541 π^+ is greater on average than the response to π^- because of a charge-exchange
 2542 effect which causes the production of additional neutral pions in the showers of

2543 π^+ [43]. The response for π^+ is also greater on average than the response to p ,
 2544 because a large fraction of the energy of π^+ hadrons is converted to an electro-
 2545 magnetic shower [44, 45]. However, the \bar{p} response is significantly higher than
 2546 the response to π^- because of the annihilation of the antiproton. FTFP_BERT
 2547 does a better job of modeling this effect than QGSP_BERT because of their differ-
 2548 ent descriptions of \bar{p} interactions with material.

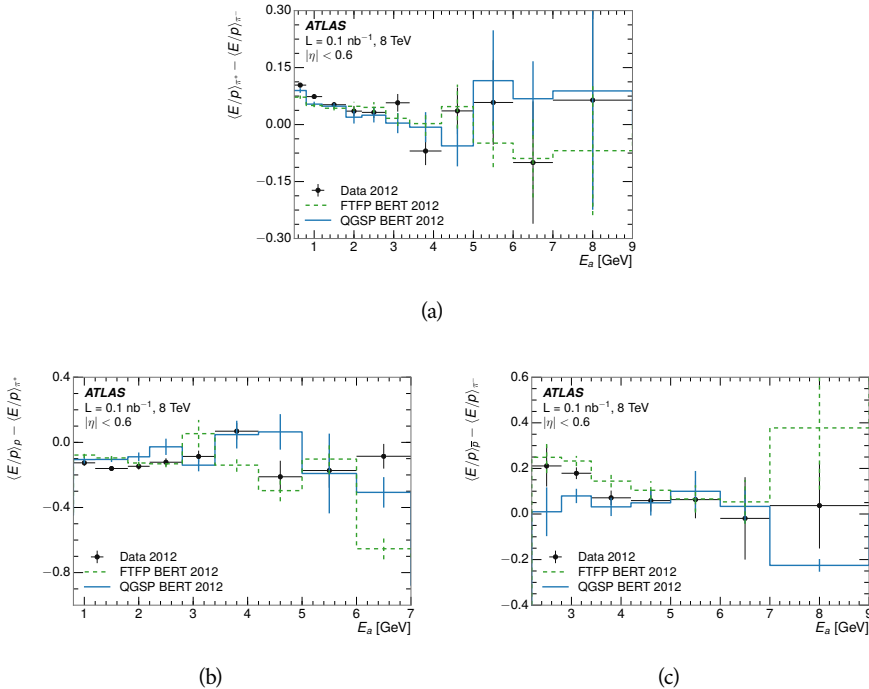


Figure 57: The difference in $\langle E/p \rangle$ between (a) π^+ and π^- (b) p and π^+ , and (c) \bar{p} and π^- .

2549 It is also possible to remove the neutral background from these response dis-
 2550 tributions using the same technique as in Section 8.2.3. The technique is largely
 2551 independent of the particle species and so can be directly applied to $\langle E/p \rangle$ for
 2552 pions. The $\langle E/p \rangle_{\text{COR}}$ distributions for pions are shown in Figure 58, which are
 2553 very similar to the inclusive results. The inclusive hadrons are comprised mostly
 2554 of pions, so this similarity is not surprising. It is also possible to see the small
 2555 differences between π^+ and π^- response here, where $\langle E/p \rangle_{\text{COR}}$ is higher on av-
 2556 erage for π^+ . The agreement between data and simulation is significantly worse
 2557 for the π^- distributions than for the π^+ , with a discrepancy greater than 10%
 2558 below 2-3 GeV.

2559 8.3.3 ADDITIONAL SPECIES IN SIMULATION

2560 The techniques above provide a method to measure the response separately for
 2561 only pions and protons. However the hadrons which forms jets include a num-
 2562 ber of additional species such as kaons and neutrons. The charged kaons are
 2563 an important component of the inclusive charged hadron distribution, which is
 2564 comprised of roughly 60-70% pions, 15-20% kaons, and 5-15% protons. These

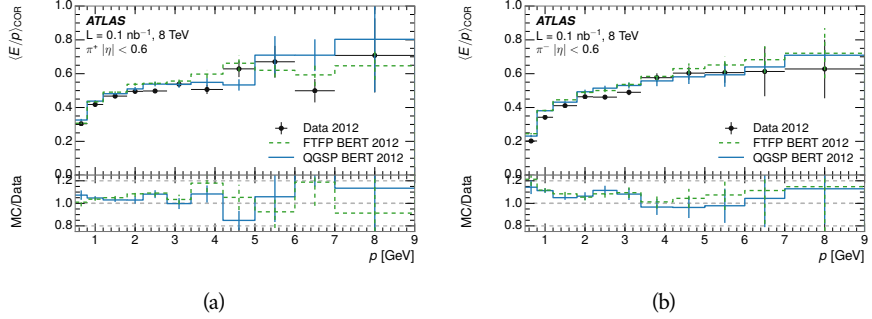


Figure 58: $\langle E/p \rangle_{\text{COR}}$ as a function of track momentum for (a) π^+ tracks and (b) π^- tracks.

are difficult to measure in data at the ATLAS detector, although a template subtraction technique has been proposed which may be effective with larger sample sizes [20]. The simulation of these particles includes noticeable differences in response at low energies, which are shown in Figure 59 for FTFP_BERT. The significant differences in response between low energy protons and antiprotons are accounted for above in the definitions of E_a .

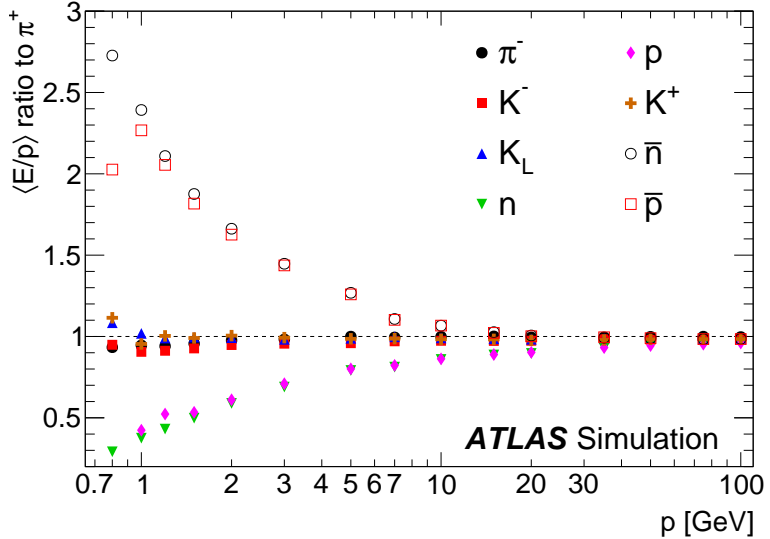


Figure 59: The ratio of the calorimeter response to single particles of various species to the calorimeter response to π^+ with the physics list FTFP_BERT.

2571 8.4 SUMMARY

2572 These various measurements of calorimeter response shown above for data and
 2573 simulation illuminate the accuracy of the simulation of hadronic interactions at
 2574 the ATLAS detector. The results were done using 2010 and 2012 data at 7 and 8
 2575 TeV, but reflect the most current understanding of the detector alignment and
 2576 geometry. A number of measurements focusing on a comparison between pro-

2577 tons and antiprotons suggest that FTFP_BERT models those interaction more
2578 accurately than QGSP_BERT. These measurements, among others, were the moti-
2579 vation to switch the default Geant4 simulation from FTFP_BERT to QGSP_BERT
2580 for all ATLAS samples.

2581 Even with these updates, there are a number of small, approximately 5%, dis-
2582 crepancies in response between the data and simulation at low energies. At
2583 higher energies the simulation of hadronic interactions is very consistent with
2584 data. Chapter 9 discusses how to use these observed differences to constrain the
2585 jet energy scale and its associated uncertainties.

2586

2587 JET ENERGY RESPONSE AND UNCERTAINTY

2588 9.1 MOTIVATION

2589 As jets form a major component of many physics analyses at ATLAS, it is crucial
 2590 to carefully calibrate the measurement of jet energies and to derive an uncer-
 2591 tainty on that measurement. These uncertainties have often been the dominant
 2592 systematic uncertainty in high-energy analyses at the LHC. Dijet and multijet
 2593 balance techniques provide a method to constrain the JES and its uncertainty in
 2594 data, and provide the default values used for ATLAS jet measurements at most
 2595 energies [46]. These techniques are limited by their reliance on measuring jets
 2596 in data, so they are statistically limited in estimating the jet energy scale at the
 2597 highest jet energies. This chapter presents another method for estimating the jet
 2598 energy scale and its uncertainty which builds up a jet from its components and
 2599 thus can be naturally extended to high jet momentum. Throughout this chapter
 2600 the jets studied are simulated using Pythia8 with the CT10 parton distribution
 2601 set [47] and the AU2 tune [24], and corrections are taken from the studies includ-
 2602 ing data and simulation in Chapter 8.

2603 As described in Section 7.4, jets are formed from topological clusters of energy
 2604 in the calorimeters using the anti- k_t algorithm. These clusters originate from a
 2605 diverse spectrum of particles, in terms of both species and momentum, leading to
 2606 significantly varied jet properties and response between jets of similar produced
 2607 momentum. Figure 60 shows the simulated distribution of particles within jets
 2608 at a few examples energies. The E/p measurements provide a thorough under-
 2609 standing of the dominant particle content of jets, the charged hadrons.

2610 9.2 UNCERTAINTY ESTIMATE

2611 Simulated jets are not necessarily expected to correctly model the energy de-
 2612 posits in the calorimeters, because of the various discrepancies discussed in Chap-
 2613 ter 8. To evaluate a jet energy response, the simulated jet energies are compared
 2614 to a corrected jet built up at the particle level. Each cluster in a jet is associated
 2615 to the truth particle which deposited it, and the energy in that cluster is then
 2616 corrected for a number of effects based on measurements in data. The primary
 2617 corrections come from the single hadron response measurements in addition to
 2618 response measured using the combined test beam which covers higher momen-
 2619 tum particles [48]. These corrections include both a shift (Δ), in order to make
 2620 the simulation match the average response in data, and an uncertainty (σ) asso-
 2621 ciated with the ability to constrain the difference between data and simulation.
 2622 Some of the dominant sources of uncertainty are itemized in Table 8 with typi-
 2623 cal values, and the full list considered is described in detail in the associated pa-

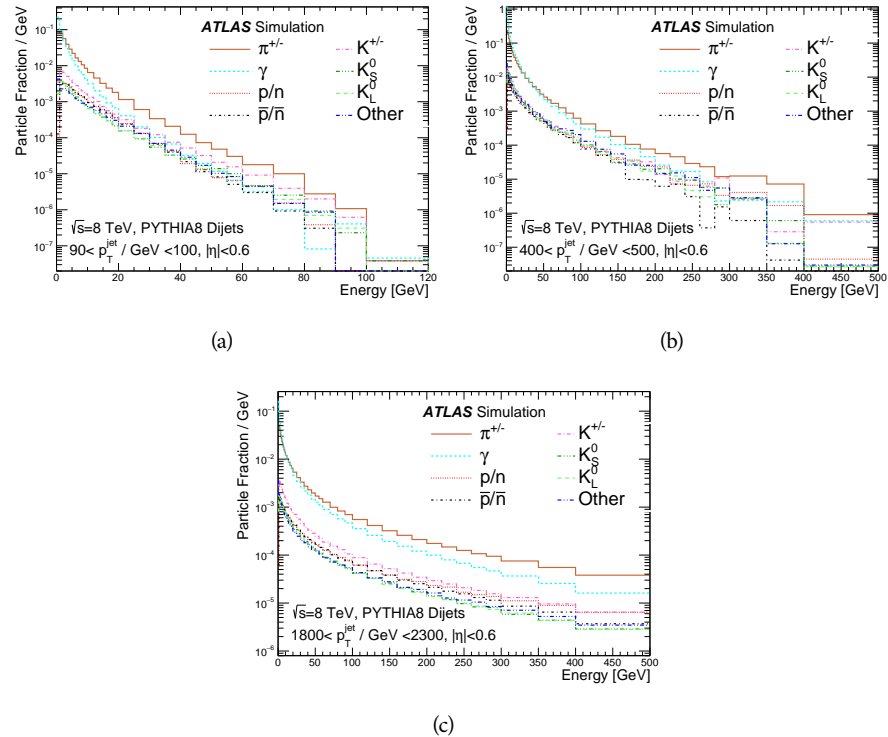


Figure 60: The spectra of true particles inside anti- k_t , $R = 0.4$ jets with (a) $90 < p_T/\text{GeV} < 100$, (b) $400 < p_T/\text{GeV} < 500$, and (c) $1800 < p_T/\text{GeV} < 2300$.

2624 per [20]. These uncertainties cover differences between the data and simulation
 2625 in the modeling of calorimeter response to a given particle. No uncertainties are
 2626 added for the difference between particle composition of jets in data and simu-
 2627 lation.

2628 From these terms, the jet energy scale and uncertainty is built up from indi-
 2629 vidual energy deposits in simulation. Each uncertainty term is treated indepen-
 2630 dently, and are taken to be gaussian distributed. The resulting scale and uncer-
 2631 tainty is shown in Figure 61, where the mean response is measured relative to
 2632 the calibrated energy reported by simulation. The dominant uncertainties come
 2633 from the statistical uncertainties on the E/p measurements at lower energies and
 2634 the additional uncertainty for out of range measurements at higher energies. The
 2635 total uncertainty from this method at intermediate jet energies is comparable to
 2636 other simulation-based methods [49] and is about twice as large as in-situ meth-
 2637 ods using data [46]. This method is the only one which provides an estimation
 2638 above 1.8 TeV, however, and so is still a crucial technique in analyses that search
 2639 for very energetic jets.

2640 These techniques can also be used to measure the correlation between bins of
 2641 average reconstructed jet momentum across a range of p_T and $|\eta|$, where cor-
 2642 relations are expected because of a similarity in particle composition at similar
 2643 energies. Figure 62 shows these correlations, where the uncertainties on jets in
 2644 neighboring bins are typically between 30% and 60% correlated. The uncertainty
 2645 on all jets becomes significantly correlated at high energies and larger pseudora-

Abbrev.	Description	Δ (%)	σ (%)
In situ E/p	The comparison of $\langle E/p \rangle_{\text{COR}}$ as described in Chapter 8 with statistical uncertainties from 500 MeV to 20 GeV.	0-3	1-5
CTB	The main $\langle E/p \rangle$ comparison uncertainties, binned in p and $ \eta $, as derived from the combined test beam results, from 20 to 350 GeV [48].	0-3	1-5
E/p Zero Fraction	The difference in the zero-fraction between data and MC simulation from 500 MeV to 20 GeV.	5-25	1-5
E/p Threshold	The uncertainty in the EM calorimeter response from the potential mismodeling of threshold effects in topological clustering.	0	0-10
Neutral	The uncertainty in the calorimeter response to neutral hadrons based on studies of physics model variations.	0	5-10
K_L	An additional uncertainty in the response to neutral K_L in the calorimeter based on studies of physics model variations.	0	20
E/p Misalignment	The uncertainty in the p measurement from misalignment of the ID.	0	1
Hadrons, $p > 350$ GeV	A flat uncertainty for all particles above the energy range or outside the longitudinal range probed with the combined test beam.	0	10

Table 8: The dominant sources of corrections and systematic uncertainties in the [JES](#) estimation technique, including typical values for the correcting shift (Δ) and the associated uncertainty (σ).

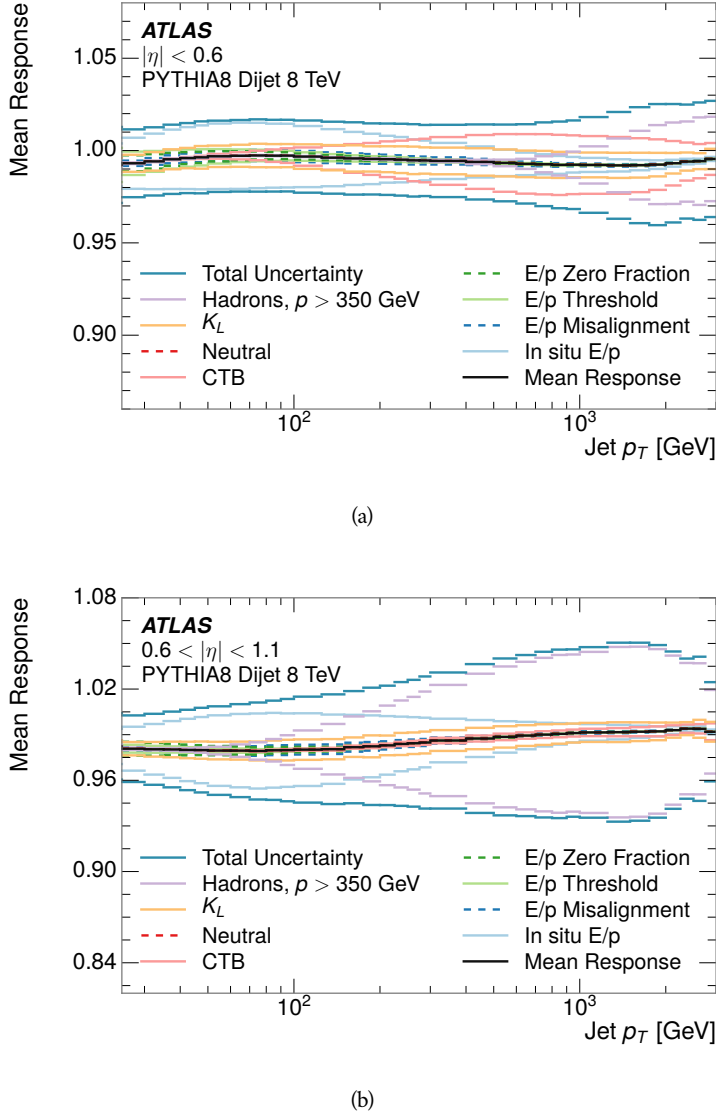


Figure 61: The [JES](#) uncertainty contributions, as well as the total [JES](#) uncertainty, as a function of jet p_T for (a) $|\eta| < 0.6$ and (b) $0.6 < |\eta| < 1.1$.

2646 pilities, when the uncertainty becomes dominated by the single term reflecting
 2647 out of range particles.

2648 9.3 SUMMARY

2649 The technique described above provides a jet energy scale and uncertainty by
 2650 building up jet corrections from the energy deposits of constituent particles. The
 2651 E/p measurements are crucial in providing corrections for the majority of parti-
 2652 cles in the jets. The uncertainty derived this way is between 2 and 5% and is about
 2653 twice as large at corresponding momentum than jet balance methods. However
 2654 this is the only uncertainty available for very energetic jets using 2012 data and
 2655 simulation, and repeating this method with Run 2 data and simulation will be

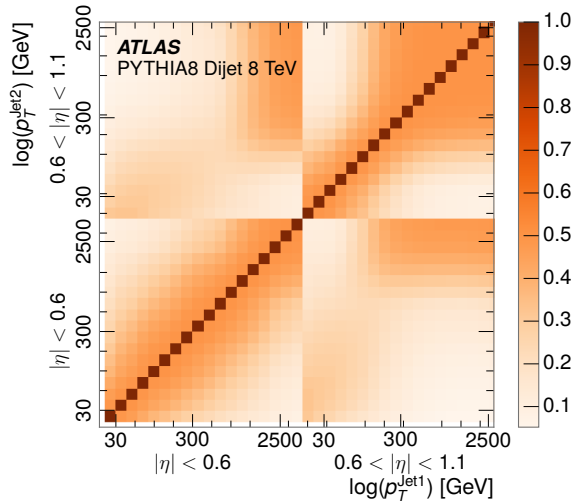


Figure 62: The JES correlations as a function of jet p_T and $|\eta|$ for jets in the central region of the detector.

2656 important in providing an uncertainty for the most energetic jets in 13 TeV col-
2657 lisions.

2658

PART V

2659

SEARCH FOR LONG-LIVED PARTICLES

2660

You can put some informational part preamble text here.

2661

2662 LONG-LIVED PARTICLES IN ATLAS

2663 As discussed in Section 2.6, various limitations in the SM suggest a need for new
 2664 particles at the TeV scale. A wide range of extensions to the Standard Model
 2665 predict that these new particles can have lifetimes greater than approximately
 2666 one-hundredth of a nanosecond. These include theories with universal extra-
 2667 dimensions [50, 51], with new fermions [52], and with leptoquarks [53]. Many
 2668 SUSY theories also produce these Long-Lived Particles (LLPs), in both R-Parity
 2669 violating [54–56] and R-Parity conserving [57–60] formulations. Split super-
 2670 symmetry [61, 62], for example, predicts long-lived gluinos with O(TeV) masses.
 2671 This search focuses specifically on the SUSY case, but many of the results are
 2672 generic to any model with LLPs.

2673 Long-lived gluinos or squarks carry color-charge and will thus hadronize into
 2674 color neutral bound states called R-Hadrons. These are composit particles like
 2675 the usual hadrons but with one supersymmetric constituent, for example $\tilde{g}q\bar{q}$
 2676 and $\tilde{q}\bar{q}$. Through this hadronization process, the neutral gluino can acquire a
 2677 charge. Gluino pair production, $pp \rightarrow \tilde{g}\tilde{g}$ has the largest cross sectional increase
 2678 with the increase in energy to 13 TeV, and so this search focuses on gluino R-
 2679 Hadrons. Planned future updates will extend the case to explicitly include squark
 2680 and chargino models, but the method covers any long-lived, charged, massive
 2681 particle.

2682 10.1 EVENT TOPOLOGY

2683 The majority of SUSY models predict that gluinos will be produced in pairs at
 2684 the LHC, through processes like $pp \rightarrow q\bar{q} \rightarrow \tilde{g}\tilde{g}$ and $pp \rightarrow gg \rightarrow \tilde{g}\tilde{g}$, where the
 2685 gluon mode dominates for the collision energy and gluino masses considered
 2686 for this search. During their production, the long-lived gluinos hadronize into
 2687 color singlet bound states including $\tilde{g}q\bar{q}$, $\tilde{g}qqq$, and even $\tilde{g}g$ [63]. The probability
 2688 to form the gluon-only bound states is a free parameter usually taken to be 0.1,
 2689 while the meson states are favored among the R-Hadrons [64]. The charged and
 2690 neutral states are approximately equally likely for mesons, so the R-Hadrons will
 2691 be charged roughly 50% of the time.

2692 These channels produce R-Hadrons with large p_T , comparable to their mass,
 2693 so that they typically propagate with $0.2 < \beta < 0.9$ [64]. The fragmentation that
 2694 produces that hadrons is very hard, so the jet structure around the R-Hadron
 2695 is minimal, with less than 5 GeV of summed particle momentum expected in a
 2696 cone of $\Delta R < 0.25$ around the R-Hadron [64]. After hadronization, depending
 2697 on the gluino lifetime, the R-Hadrons then decay into hadrons and a LSP [63].

2698 In summary, the expected event for pair-produced long-lived gluinos is very
 2699 simple: two isolated, high-momentum R-Hadrons that propagate through the
 2700 detector before decaying into jets. The observable features of such events depend

2701 strongly on the interaction of the R-Hadron with the material of the detector and
 2702 also its lifetime. Section 10.1.1 describes the interactions of R-Hadrons which
 2703 reach the various detector elements in ATLAS and Section 10.1.2 provides a sum-
 2704 mary of the observable event descriptions for R-Hadrons of various lifetimes.

2705 10.11 DETECTOR INTERACTIONS

2706 After approximately 0.2 ns, the R-Hadron reaches the pixel detector. If charged,
 2707 it deposits energy into the material through repeated single collisions that result
 2708 in ionization of the silicon substrate [9]. Because of its comparatively low β , the
 2709 ionization energy can be significantly greater than expected for SM particles be-
 2710 cause the most-probable energy loss grows significantly as β decreases [9]. This
 2711 large ionization can be measured through the ToT read out from the pixel detec-
 2712 tor as described in Section 7.1.2. Large ionization in the inner detector is one of
 2713 the major characteristic features of LLPs.

2714 Throughout the next few nanoseconds, the R-Hadron propagates through the
 2715 remainder of the inner detector. A charged R-Hadron will provide hits in each
 2716 of these systems as would any other charged particle, and can be reconstructed
 2717 as a track. The track reconstruction provides a measurement of its trajectory
 2718 and thus its momentum as described in Section 7.1. The large momentum is
 2719 another characteristic feature of massive particles produced at the LHC. **Note: At**
 2720 **this point I am failing to mention that the TRT provides a possible dE/dx**
 2721 **measurement, because no one uses it as far as I know.**

2722 As of roughly 20 ns, the R-Hadron enters the calorimeter where it interacts
 2723 hadronically with the material. Because of its large mass and momentum, the
 2724 R-Hadron does not typically stop in the calorimeter, but rather deposits a small
 2725 fraction of its energy through repeated interactions with nucleons. The proba-
 2726 bility of interaction between the gluino itself and a nucleon is low because the
 2727 cross section drops off with the inverse square of its mass, so the interactions are
 2728 primarily governed by the light constituents [65]. Each of these interactions can
 2729 potentially change that quark content and thus change the sign of the R-Hadron,
 2730 so that the charge at exit is typically uncorrelated with the charge at entry [64].
 2731 The total energy deposited in the calorimeters during the propagation is small
 2732 compared to the kinetic energy of the R-Hadron, around 20-40 GeV, so that
 2733 E/p is typically less than 0.1 [64].

2734 Then, 30 ns after the collision, it reaches the muon system, where it again
 2735 ionizes in the material if charged and can be reconstructed as a muon track. Be-
 2736 cause of the charge-flipping interactions in the calorimeter, this track may have
 2737 the opposite sign of the track reconstructed in the inner detector, or there may
 2738 be a track present when there was none in the inner detector and vice-versa. The
 2739 propagation time at the typically lower β results in a significant delay compared
 2740 to muons, and that delay can be assessed in terms of a time-of-flight measure-
 2741 ment. Because of the probability of charge-flip and late arrival, there is a signif-
 2742 icant chance that an R-Hadron which was produced with a charge will not be
 2743 identified as a muon. The long time-of-flight is another characteristic feature of
 2744 R-Hadrons which are reconstructed as muons.

2745 10.1.2 LIFETIME DEPENDENCE

2746 The above description assumed a lifetime long enough for the R-Hadron to exit
 2747 the detector, which through this search is referred to as “stable”, even though
 2748 the particle may decay after exiting the detector. There are several unique sig-
 2749 natures at shorter lifetimes where the R-Hadron decays in various parts of the
 2750 inner detector; these lifetimes are referred to as “metastable”.

2751 The shortest case where the R-Hadron is considered metastable is for life-
 2752 times around 0.01 ns, where the particle decays before reaching any of the de-
 2753 tector elements. Although the R-Hadrons are produced opposite each other in
 2754 the transverse plane, each R-Hadron decays to a jet and an LSP. The LSPs are not
 2755 measured, so the produced jets can be significantly imbalanced in the transverse
 2756 plane which results in large missing energy. That missing energy can be used
 2757 to trigger candidate events, and provides the most efficient trigger option for
 2758 shorter lifetimes. Additionally, the precision of the tracking system allows the
 2759 displaced vertex of the R-Hadron decay to be reconstructed from the charged
 2760 particles in the jet. The distance of that vertex from the interaction point can
 2761 be used to distinguish R-Hadron decays from other processes. Figure 63 shows
 2762 a schematic diagram of an example R-Hadron event with such a lifetime. The
 2763 diagram is not to scale, but instead illustrates the detector interactions in the
 2764 pixel detector, calorimeters, and muon system. It includes a representation of
 2765 the charged R-Hadron and the neutral R-Hadron, as well as the LSPs and jets
 2766 (shown as charged hadrons) produced in the decay. Neutral hadrons may also
 2767 be produced in the decay but are not depicted. Previous searches on ATLAS have
 2768 used the displaced vertex to target LLP decays [66].

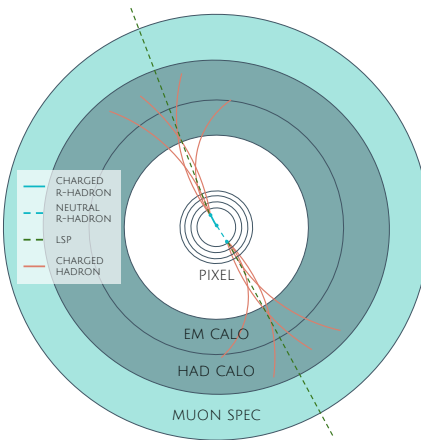


Figure 63: A schematic diagram of an R-Hadron event with a lifetime around 0.01 ns.
 The diagram includes one charged R-Hadron (solid blue), one neutral R-Hadron (dashed blue), LSPs (dashed green) and charged hadrons (solid orange). The pixel detector, calorimeters, and muon system are illustrated but not to scale.

2769 The next distinguishable case occurs at lifetimes greater than 0.1 ns, where
 2770 the R-Hadron forms a partial track in the inner detector. If the decay products
 2771 are sufficiently soft, they may not be reconstructed, and this forms a unique sig-

2772 nature of a disappearing track. An example of such an event is illustrated in
 2773 Figure 64, which shows the short track in the inner detector and the undetected
 2774 soft charged hadron and LSP that are produced. A dedicated search on ATLAS used
 2775 the disappearing track signature to search for LLP in Run 1 [67]. **zNote: might**
 2776 **not be worth mentioning the disappearing track here since it is actually a**
 2777 **chargino search, the soft pion is pretty unique to charginos.**

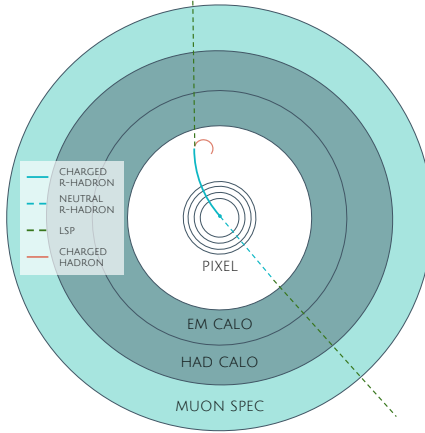


Figure 64: A schematic diagram of an R-Hadron event with a lifetime around 4 ns. The diagram includes one charged R-Hadron (solid blue), one neutral R-Hadron (dashed blue), LSPs (dashed green) and a charged hadron (solid orange). The pixel detector, calorimeters, and muon system are illustrated but not to scale.

2778 If the decay products are not soft, the R-Hadron daughters form jets, resulting
 2779 in an event-level signature of up to two high-momentum tracks, jets, and signif-
 2780 icant missing energy. The missing energy has the same origin as in the case of
 2781 0.01 ns lifetimes, from the decay to unmeasured particles, and again can be large.
 2782 The high-momentum tracks will also have the characteristically high-ionization
 2783 of massive, long-lived particles in the inner detector. Figure 65 illustrates an ex-
 2784 ample event with one charged R-Hadron which decays after approximately 10 ns,
 2785 and shows how the jets from the decay can still be reconstructed in the calorime-
 2786 ter. Several previous searches on ATLAS from Run 1 have used this signature to
 2787 search for R-Hadrons [68, 69], including a dedicated search for metastable parti-
 2788 cles [70].

2789 If the lifetime is longer than several nanoseconds, in the range of 15-30 ns,
 2790 the R-Hadron decay can occur in or after the calorimeters, but prior to reaching
 2791 the muon system. This case is similar to the above, although the jets may not be
 2792 reconstructed, and is covered by many of the same search strategies. The events
 2793 still often have large missing energy, although it is generated through different
 2794 mechanisms. The R-Hadrons do not deposit much energy in the calorimeters, so
 2795 a neutral R-Hadron will not enter into the missing energy calculation. A charged
 2796 R-Hadron opposite a neutral R-Hadron will thus generate significant missing en-
 2797 ergy, and close to 50% of pair-produced R-Hadron events fall into this category.
 2798 If both R-Hadrons are neutral then the missing energy will be low because nei-
 2799 ther is detected. Two charged R-Hadrons will also result in low missing energy
 2800 because both are reconstructed as tracks and will balance each other in the trans-

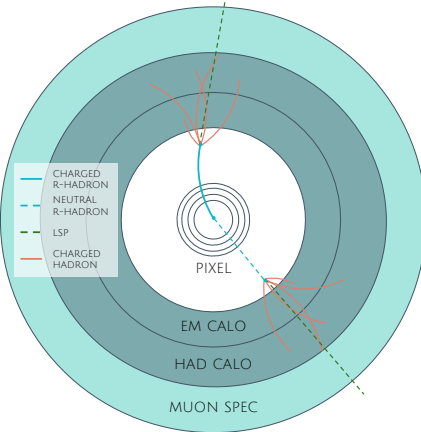


Figure 65: A schematic diagram of an R-Hadron event with a lifetime around 5 ns. The diagram includes one charged R-Hadron (solid blue), one neutral R-Hadron (dashed blue), LSPs (dashed green) and charged hadrons (solid orange). The pixel detector, calorimeters, and muon system are illustrated but not to scale.

verse plane. A small fraction of the time, one of the charged R-Hadron tracks may fail quality requirements and thus be excluded from the missing energy calculation and again result in significant missing energy. Figure 66 illustrates another example event with one charged R-Hadron which decays after approximately 20 ns, and shows how the jets from the decay might not be reconstructed.

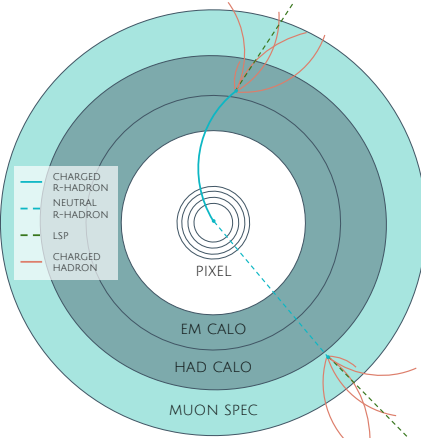


Figure 66: A schematic diagram of an R-Hadron event with a lifetime around 20 ns. The diagram includes one charged R-Hadron (solid blue), one neutral R-Hadron (dashed blue), LSPs (dashed green) and charged hadrons (solid orange). The pixel detector, calorimeters, and muon system are illustrated but not to scale.

The longest lifetimes, the stable case, has all of the features of the 30-50 ns case but with the addition of muon tracks for any R-Hadrons that exit the calorimeter with a charge. That muon track can provide additional information from time-of-flight measurements to help identify LSPs. An example of the event topology for one charged and one neutral stable R-Hadron is shown in Figure 67. Some searches on ATLAS have included this information to improve the search reach for stable particles [69, 71].

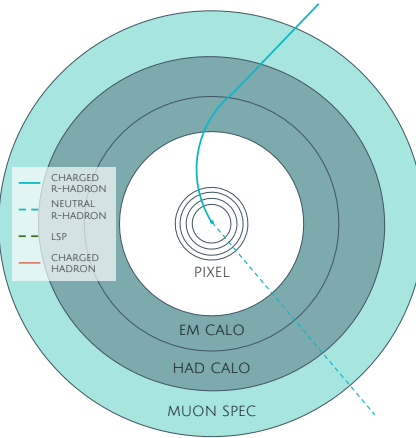


Figure 67: A schematic diagram of an R-Hadron event with a lifetime around 20 ns. The diagram includes one charged R-Hadron (solid blue) and one neutral R-Hadron (dashed blue). The pixel detector, calorimeters, and muon system are illustrated but not to scale.

2813 10.2 SIMULATION

2814 All of the event topologies discussed above are explored by simulations of R-
 2815 Hadron events in the [ATLAS](#) detector. A large number of such samples are gen-
 2816 erated to determine signal efficiencies, to measure expected yields, and to esti-
 2817 mate uncertainties. The primary interaction, pair production of gluinos with
 2818 masses between 400 and 3000 GeV, is simulated using [Pythia 6.4.27](#) [72]
 2819 with the AUET2B [73] set of tuned parameters for the underlying event and the
 2820 [CTEQ6L1](#) [47] PDF set. The simulated interactions include a modeling of pileup
 2821 by adding secondary, minimum bias interactions from both the same (in-time
 2822 pileup) and nearby (out-of-time pileup) bunch crossings. This event generation
 2823 is then augmented with a dedicated hadronization routine to hadronize the long-
 2824 lived gluinos into final states with R-Hadrons [74], with the probability to form
 2825 a gluon-gluino bound set at 10% [75].

2826 The cross sections used for these processes are calculated at next-to-leading
 2827 order ([NLO](#)) in the strong coupling constant with a resummation of soft-gluon
 2828 emmission at next-to-leading logarithmic ([NLL](#)) [76–80]. The nominal predic-
 2829 tions and the uncertainties for each mass point are taken from an envelope of
 2830 cross-section predictions using different PDF sets and factorization and renor-
 2831 malization scales [81].

2832 The R-Hadrons then undergo a full detector simulation [], where the interac-
 2833 tions of the R-Hadrons with the material of the detector are described by dedi-
 2834 cated [Geant4](#) [17] routines. These routines model the interactions described in
 2835 Section 10.1.1, including the ionizing interactions in the silicon modules of the
 2836 inner detector and the R-Hadron-nucleon interactions in the calorimeters [82,
 2837 83]. The specific routine chosen to describe the interactions of the R-Hadrons
 2838 with nucleons, the “generic model”, uses a pragmatic approach where the scatter-
 2839 ing cross section is taken to be a constant 12 mb per light quark. In this model

2840 the gluino itself does not interact at all except through its role as a reservoir of
2841 kinetic energy.

2842 The lifetimes of these R-Hadrons are then simulated at several working points,
2843 $\tau = 0.1, 1.0, 3.0, 10, 30, 50$ and detector stable, where the particle is required to
2844 decay after propagating for a time compatible with its lifetime. Only one decay
2845 mode is simulated for these samples, $\tilde{g} \rightarrow q\bar{q}\tilde{\chi}_1^0$ with the neutralino mass set to
2846 100 GeV, which is chosen because it has the highest sensitivity among all of the
2847 modes studied in previous searches [70]. Heavier neutralinos have similar results
2848 but generate less missing energy which reduces the efficiency of triggering.

2849 All of the simulated events are then reconstructed using the same software
2850 used for collision data. The fully reconstructed events are then reweighted to
2851 match the distribution of initial state radiation in an alternative sample of events,
2852 generated with MG5_aMC@NLO [84], which has a more accurate description of ra-
2853 diate effects than Pythia6. This reweighting provides a more accurate descrip-
2854 tion of the momentum of the gluino-gluino system and is important in modeling
2855 the efficiency of triggering and offline event selection.

2856

2857 EVENT SELECTION

2858 The [LLPs](#) targeted by this search differ in their interactions with the detector from
 2859 [SM](#) particles primarily because of their large mass. When produced at the ener-
 2860 gies available at the [LHC](#), that large mass results in a low β (typically $0.2 < \beta <$
 2861 0.9). Such slow-moving particles heavily ionize in detector material. Each layer
 2862 of the pixel detector provides a measurement of that ionization, through [ToT](#), as
 2863 discussed in Section 7.1.2. The ionization in the pixel detector, quantified in
 2864 terms of dE/dx , provides the major focus for this search technique, along with
 2865 the momentum measured in the entire inner detector. It is effective both for its
 2866 discriminating power and its use in reconstructing a particle's mass, and it can
 2867 be used for a wide range of masses and lifetimes as discussed in Section 10.1.2.
 2868 However dE/dx needs to be augmented with a few additional selection require-
 2869 ments to provide a mechanism for triggering and to further reduce backgrounds.

2870 Ionization itself is not currently accessible for triggering, so this search in-
 2871 stead relies on E_T^{miss} to trigger signal events. Although triggering on E_T^{miss} can
 2872 be inefficient, E_T^{miss} is often large for many production mechanisms of [LLPs](#), as
 2873 discussed in Section 10.1.

2874 The use of ionization to reject [SM](#) backgrounds relies on well-measured, high-
 2875 momentum tracks, so some basic requirements on quality and kinematics are
 2876 placed on the tracks considered in this search. These quality requirements have
 2877 been significantly enhanced in Run 2 by a newly introduced tracking variable
 2878 that is very effective in removing highly-ionizing backgrounds caused by over-
 2879 lapping tracks. A few additional requirements are placed on the tracks consid-
 2880 ered for [LLP](#) candidates that increase background rejection by targeting specific
 2881 types of [SM](#) particles. These techniques provide a significant analysis improve-
 2882 ment over previous iterations of ionization-based searches on ATLAS by provid-
 2883 ing additional background rejection with minimal loss in signal efficiency.

2884 The ionization measurement with the Pixel detector can be calibrated to pro-
 2885 vide an estimator of $\beta\gamma$. That estimate, together with the momentum measure-
 2886 ment provided by tracking, can be used to reconstruct a mass for each track
 2887 which traverses the pixel detector. That mass variable will be peaked at the [LLP](#)
 2888 mass for any signal, and provides an additional tool to search for an excess. In
 2889 addition to an explicit requirement on ionization, this search constructs a mass-
 2890 window for each targeted signal mass in order to evaluate any excess of events
 2891 and to set limits.

2892 The strategy discussed here is optimized for lifetimes of $O(1) - O(10)$ ns.
 2893 Pixel ionization is especially useful in this regime as particles only need to prop-
 2894 agate through the first seven layers of the inner detector, about 37 cm from the
 2895 beam axis. The search is still competitive with other searches for [LLPs](#) at longer
 2896 lifetimes, because the primary discriminating variables are still applicable even
 2897 for particles that do not decay within the detector [71]. Although the majority of

2898 the requirements will be the same for all lifetimes, two signal regions are defined
 2899 to optimize separately for intermediate and long lifetime particles.

2900 11.1 TRIGGER

2901 Triggering remains a significant difficulty in defining an event selection with
 2902 high signal efficiency in a search for LLPs. There are no triggers available in
 2903 the current ATLAS system that can fire directly from a high momentum track
 2904 with large ionization (Section 6.6). Although in some configurations a charged
 2905 LLP can fire muon triggers, this requirement introduces significant model depen-
 2906 dence on both the allowed lifetimes and the interactions in the calorimeter [64],
 2907 as discussed in Section 10.1.1.

2908 For a search targeting particles which may decay prior to reaching the muon
 2909 system, the most efficient available trigger is based on missing energy [64]. As
 2910 discussed in Section 10.1, signal events can produce significant E_T^{miss} by a few
 2911 mechanisms. At the trigger level however, the missing energy is only calculated
 2912 using the calorimeters (Section 6.6) where the R-Hadrons deposit little energy.
 2913 So, at short lifetimes, E_T^{miss} measured in the calorimeter is generated by an im-
 2914 balance between the jets and undetected LSPs produced in R-Hadron decays. At
 2915 longer lifetimes, without the decay products, missing energy is only produced in
 2916 the calorimeters when the R-Hadrons recoil against an initial state radiation (ISR)
 2917 jet.

2918 These features are highlighted in Figure 68, which shows the E_T^{miss} distribu-
 2919 tions for simulated short lifetime (3 ns) and stable R-Hadron events. The figure
 2920 includes both the offline E_T^{miss} , the missing energy calculated with all available
 2921 information, and Calorimeter E_T^{miss} , the missing energy calculated using only
 2922 information available at the calorimeter which approximates the missing energy
 2923 available at the trigger. The short lifetime sample has significantly greater E_T^{miss}
 2924 and Calorimeter E_T^{miss} than the stable sample as expected. For the stable sam-
 2925 ple, a small fraction of events with very large E_T^{miss} (about 5%) migrate into the
 2926 bin with very small Calorimeter E_T^{miss} because the E_T^{miss} produced by a charged
 2927 R-Hadron track opposite a neutral R-Hadron track does not contribute any miss-
 2928 ing energy in the calorimeters.

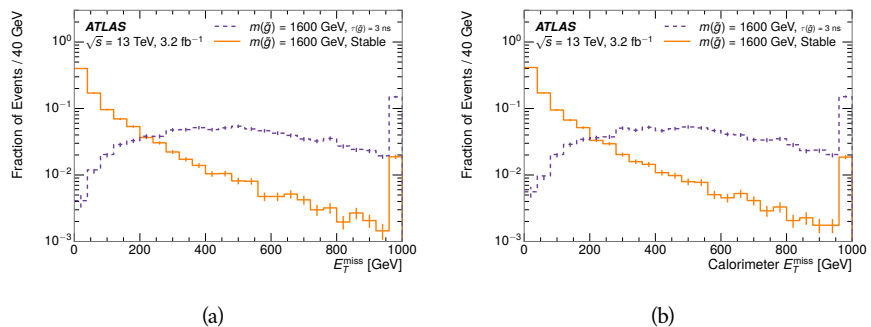


Figure 68: The distribution of (a) E_T^{miss} and (b) Calorimeter E_T^{miss} for simulated signal events before the trigger requirement.

2929 So, either case to some extent relies on kinematic degrees of freedom to pro-
 2930 duce missing energy, as the pair-produced LLPs tend to balance each other in
 2931 the transverse plain. That balance results in a relatively low efficiency for long-
 2932 lifetime particles, roughly 40%, and efficiencies between 65% and 95% for shorter
 2933 lifetimes depending on both the mass and the lifetime. For long lifetimes in par-
 2934 ticular, the presence of ISR is important in providing an imbalance in the trans-
 2935 verse plane, and is an important aspect of modeling the selection efficiency for
 2936 R-Hadron events.

2937 The missing energy trigger with the lowest threshold available is chosen for
 2938 this selection in order to maximize the trigger efficiency. During 2015 data col-
 2939 lection this was the HLT_xe70 trigger, which used a 50 GeV threshold on miss-
 2940 ing energy at LVL1 and a 70 GeV threshold on missing energy at the HLT. These
 2941 formation of the trigger decision for missing energy was discussed in more detail
 2942 in Section 6.6.

2943 11.2 KINEMATICS AND ISOLATION

2944 After the trigger requirement, each event is required to have a primary vertex
 2945 reconstructed from at least two well-measured tracks in the inner detector, each
 2946 with $p_T > 400$ MeV. If more than one such vertex exists, the primary vertex
 2947 is taken to be the one with the largest summed track momentum for all tracks
 2948 associated to that vertex. The offline reconstructed E_T^{miss} is required to be above
 2949 130 GeV to additionally reject SM backgrounds. The transverse missing energy
 2950 is calculated using fully reconstructed and calibrated offline objects, as described
 2951 in Section 7.5. In particular the E_T^{miss} definition in this selection uses jets recon-
 2952 structed with the anti- k_t algorithm with radius $R = 0.4$ from clusters of energy
 2953 in the calorimeter (Section 7.4) and with $p_T > 20$ GeV, as well as reconstructed
 2954 muons, electrons, and tracks not identified as another object type.

2955 The E_T^{miss} distributions are shown for data and a few simulated signals in Fig-
 2956 ure 69, after the trigger requirement. The cut placed at 130 GeV is 95% effi-
 2957 cient for metastable and 90% efficient for stable particles, after the trigger re-
 2958 quirement, because of the missing energy generating mechanisms discussed pre-
 2959 viously. The distribution of data in this figure and subsequent figures in this sec-
 2960 tion can be interpreted as the distribution of backgrounds, as any signal contam-
 2961 ination would be negligible if present at these early stages of the selection (prior
 2962 to the final requirement on ionization). The background falls rapidly with miss-
 2963 ing energy, motivating the direct requirement on E_T^{miss} for the signal region. Al-
 2964 though a tighter requirement than the specified value of 130 GeV would seem to
 2965 increase the search potential from these early distributions, other requirements
 2966 are more optimal when taken as a whole. The specific values for each require-
 2967 ment in signal region were optimized considering the increase in discovery reach
 2968 for tightening the requirement on each discriminating variable. **NOTE: If space**
 2969 **and time permit, I will add a whole section about signal region optimiza-**
 2970 **tion..**

2971 It is typically the practice for searches for new physics on ATLAS to place an
 2972 offline requirement on the triggering variable that is sufficiently tight to guar-

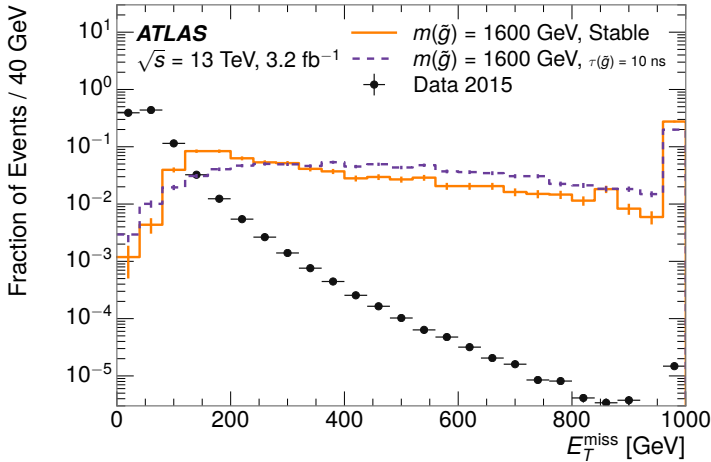


Figure 69: The distribution of E_T^{miss} for data and simulated signal events, after the trigger requirement.

2973 antee that the event would pass the trigger. Such a tight requirement makes the
 2974 uncertainty on the trigger efficiency of the simulation negligible, as modeling the
 2975 regime where the trigger is only partially efficient can be difficult. In this analy-
 2976 sis, however, because of the atypical interactions of R-Hadrons with the tracker
 2977 and the calorimeter, the offline requirement on E_T^{miss} is not sufficient to guar-
 2978 antee a 100% trigger efficiency even at large values, as can be seen in Figure 70.
 2979 This figure shows the efficiency for passing the HLT_xe70 trigger as a function
 2980 of the requirement on E_T^{miss} , which plateaus to roughly 85% even at large values.
 2981 This plateau does not reach 100% because events which have large offline miss-
 2982 ing energy from a neutral R-Hadron produced opposite of a charged R-Hadron
 2983 can have low missing energy in the calorimeters. The Calorimeter E_T^{miss} , on the
 2984 other hand, does not have this effect and reaches 100% efficiency at large values
 2985 because it is the quantity that directly corresponds to the trigger threshold. In
 2986 both cases the efficiency of triggering is greater for the short lifetime sample be-
 2987 cause the late decays to hadrons and LSPs produce an imbalance in the calorime-
 2988 ters even though they may not be reconstructed offline as tracks or jets. For this
 2989 reason, the requirement on E_T^{miss} is determined by optimizing the background
 2990 rejection even though it corresponds to a value of trigger efficiency significantly
 2991 below 1.0.

2992 Potential signal events are then required to have at least one candidate LLP
 2993 track. Although the LLPs are produced in pairs, many models do not consistently
 2994 yield two charged particles. For example, in the R-Hadron model highlighted
 2995 here, only 20% of events have two charged R-Hadrons while 47% of events have
 2996 just one. A signal region requiring two charged candidates could be a powerful
 2997 improvement in background rejection for a larger dataset, but it is not consid-
 2998 ered in this version of the analysis as it was found to be unnecessary to reject the
 2999 majority of backgrounds.

3000 For a track to be selected as a candidate, it must have $p_T > 50 \text{ GeV}$ and pass
 3001 basic quality requirements. The track must be associated to the primary vertex.

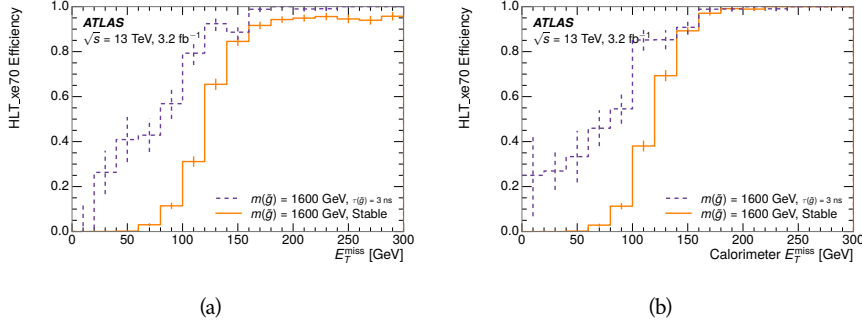


Figure 70: The trigger efficiency for the HLT_xe70 trigger requirement as a function of (a) E_T^{miss} and (b) Calorimeter E_T^{miss} for simulated signal events.

It must also have at least seven clusters in the silicon layers in the inner detector to ensure an accurate measurement of momentum. Those clusters must include one in the innermost layer if the extrapolated track is expected to pass through that layer. And to ensure a reliable measurement of ionization, the track is required to have at least two clusters in the pixel detector that provide a measurement of dE/dx .

At this point in the selection, there is a significant high-ionization background from multiple tracks that significantly overlap in the inner detector. Previous version of this analysis have rejected these overlaps by an explicit overlap rejection between pairs of fully reconstructed tracks, typically by requiring no additional tracks within a cone around the candidate. This technique, however, fails to remove the background from tracks that overlap so precisely that the tracks cannot be separately resolved, which can be produced in very collimated photon conversions or decays of pions.

A new method, added in Run 2, identifies cluster shapes that are likely formed by multiple particles based on a neural network classification algorithm. The number of clusters that are classified this way in the pixel detector for a given track is called N_{split} . As the shape of clusters requires significantly less spatial separation to identify overlaps than it does to reconstruct two fully resolved tracks, this variable is more effective at rejecting backgrounds from overlaps. Figure 71 shows the dependence of ionization on N_{split} ; as N_{split} increases the most probable value of dE/dx grows significantly up to twice the expected value when $N_{\text{split}} = 4$.

This requirement is very successful in reducing the long positive tail of the dE/dx distributions, as can be seen in Figure 72. Comparing the distribution for “baseline tracks”, tracks with only the above requirements on clusters applied and before the requirement on N_{split} , to the distribution with $N_{\text{split}} = 0$, it is clear that the fraction of tracks with large dE/dx is reduced by several orders of magnitude. The tracks without split hits are very close to the dE/dx distribution of identified muons, which are extremely well isolated on average. Figure 72 also includes the distribution of dE/dx in an example signal simulation to demonstrate how effective dE/dx is as a discriminating variable with this isolation applied. The background falls rapidly for $dE/dx > 1.8 \text{ MeVg}^{-1}\text{cm}^2$

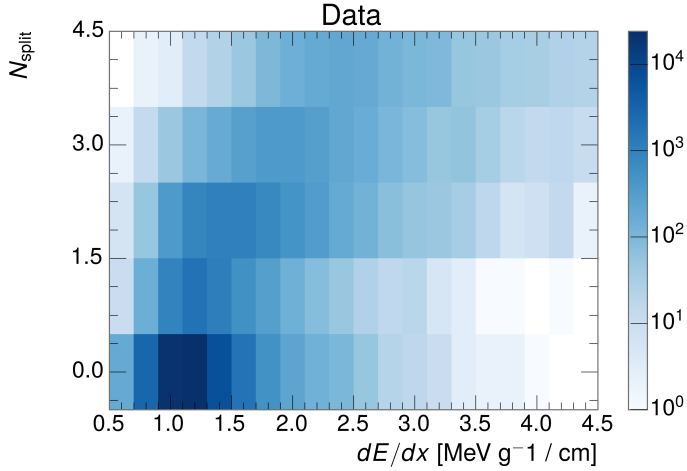


Figure 71: The dependence of dE/dx on N_{split} in data after basic track hit requirements have been applied.

3035 while the majority of the signal, approximately 90% depending on the mass, falls
 3036 above that threshold. Over 90% of [LLP](#) tracks in simulated signal events pass the
 3037 N_{split} -based isolation requirement.

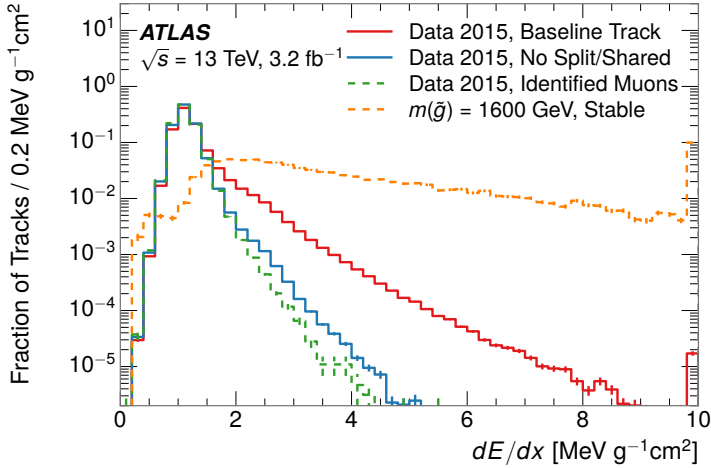


Figure 72: The distribution of dE/dx with various selections applied in data and simulated signal events.

3038 A few additional kinematic requirements are imposed to help reduce [SM](#) back-
 3039 grounds. The momentum of the candidate track must be at least 150 GeV, and
 3040 the uncertainty on that measurement must be less than 50%. The distribution of
 3041 momentum is shown in Figure 73 for tracks in data and simulated signal events
 3042 after the previously discussed requirements on clusters, transverse momentum,
 3043 and isolation have been imposed. The signal particles are much harder on aver-

age than their backgrounds because of the high energy interactions required to produce them. The transverse mass, M_T , defined as

$$M_T = \sqrt{2p_T E_T^{\text{miss}}(1 - \cos(\Delta\phi(E_T^{\text{miss}}, \text{track})))} \quad (20)$$

estimates the mass of a decay of to a single charged particle and an undetected particle and is required to be greater than 130 GeV to reject contributions from the decay of W bosons. Figure 74 shows the distribution of M_T for data and simulated signal events. The signal is distributed over a wide range of M_T , with about 90% above the threshold value of 130 GeV. The data shows a dual-peaked structure, where the first peak comes from W boson decays and the second peak is a kinematic shaping from the requirements on E_T^{miss} and the track p_T in dijet events.

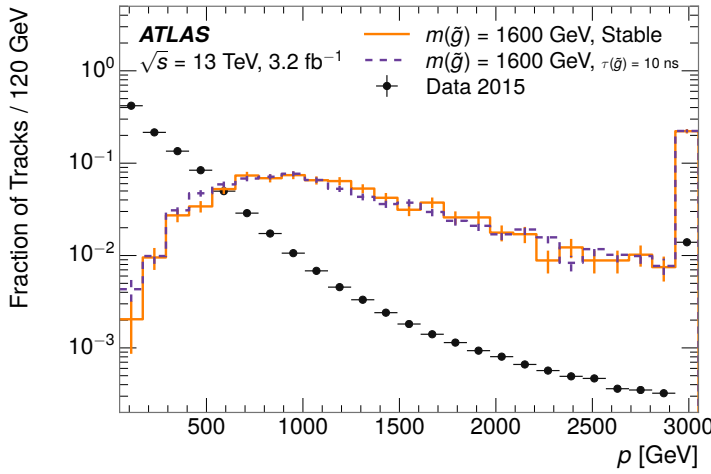


Figure 73: The distribution of track momentum for data and simulated signal events, after previous selection requirements have been applied.

11.3 PARTICLE SPECIES REJECTION

The amount of ionization deposited by particles with low mass and high momentum has a large positive tail [9], so backgrounds can be formed by a wide variety of SM processes when various charged particles have a few randomly large deposits of energy in the pixel detector. Those backgrounds can be additionally reduced by targeting other interactions with the detector where they are expected to have different behavior than R-Hadrons. The interactions with the detector depend on the types of particles produced rather than the processes which produce them, so this search forms a series of rejections to remove backgrounds from individual particle species. These rejections focus on using additional features of the event, other than the kinematics of the candidate track, as they can provide a powerful source of background rejection with very high signal efficiency. However, the lifetime of an R-Hadron can significantly change its

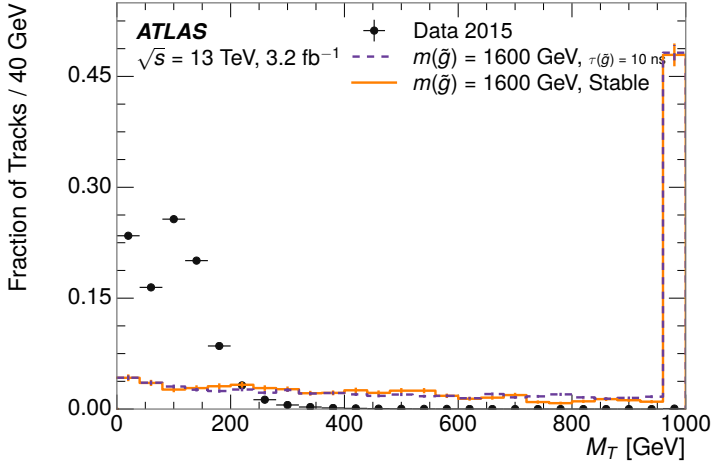


Figure 74: The distribution of M_T for data and simulated signal events, after previous selection requirements have been applied.

3067 detector characteristics, as discussed in Section 10.1.2. To accommodate these
 3068 differences, the SM rejections defined in this section are split to form two signal
 3069 regions, one for long-lifetimes particles, the stable region ($50 \leq \tau[\text{ns}] < \infty \text{ ns}$),
 3070 and one for intermediate lifetime particles, the metastable region ($0.4 < \tau[\text{ns}] <$
 3071 50).

3072 Jets can be very effectively rejected by considering the larger-scale isolation of
 3073 the candidate track. In this case the isolation focuses on the production of nearby
 3074 particles as a jet-veto, rather than the isolation from overlapping tracks based on
 3075 N_{split} that was used to reduce high-ionization backgrounds. As explained in Sec-
 3076 tion 10.1, the fragmentation process which produces an R-Hadron is very hard
 3077 and thus is not expected to produce additional particles with a summed momen-
 3078 tum of more than 5 GeV. The jet-veto uses the summed momentum of tracks
 3079 with a cone of $\Delta R < 0.25$, referred to as p_T^{Cone} , which is shown in Figure 75 for
 3080 data and simulated signal events. In the data this value has a peak at zero from
 3081 isolated tracks such as leptons, and a long tail from jets which contains as much
 3082 as 80% of the background above 20 GeV at this stage of the selection. In signal
 3083 events p_T^{Cone} is strongly peaked at zero and significantly less than 1% of signal
 3084 events have p_T^{Cone} above 20 GeV. This makes a requirement of $p_T^{\text{Cone}} < 20 \text{ GeV}$
 3085 a very effective method to reject background without losing signal efficiency.
 3086 For the stable signal region, this cut is further tightened to $p_T^{\text{Cone}} < 5 \text{ GeV}$ as
 3087 it is the most effective variable remaining to extend the search reach for long
 3088 lifetimes.

3089 Even for fully isolated particles, there are additional methods to reject each
 3090 type of particle using information in the muon system and calorimeters. Muons
 3091 can be identified very reliably using the tracks in the muon system, as described
 3092 in Section 7.3. For intermediate lifetimes the LLPs do not survive long enough
 3093 to reach the muon system, and so muons are vetoed by rejecting tracks that as-
 3094 sociate to a muon with medium muon identification requirements (Section 7.3).
 3095 For longer lifetimes, this rejection is not applied because LLPs which reach the

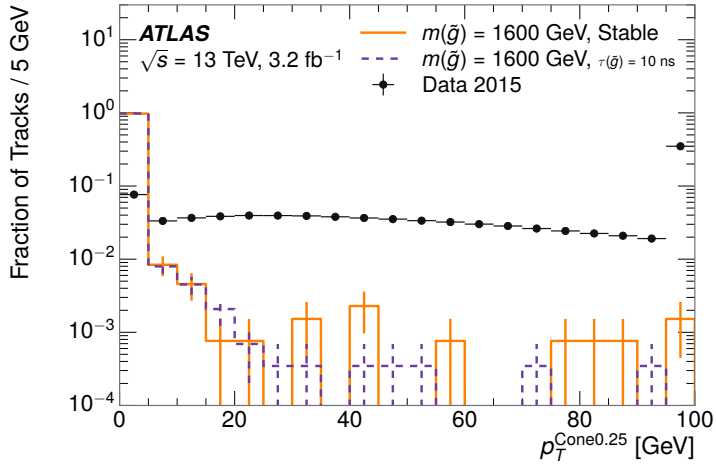


Figure 75: The distribution of summed tracked momentum within a cone of $\Delta R < 0.25$ around the candidate track for data and simulated signal events, after previous selection requirements have been applied.

3096 muon system can be identified as muons as often as 30% of the time in simulated
 3097 samples.

3098 Calorimeter-based particle rejection relies on the expected small deposits of
 3099 energy from LLPs. When the lifetime is long enough to reach the calorimeter, a
 3100 LLP deposits little of its energy as it traverses the material, as discussed in Sec-
 3101 tion 10.1. Even when the particle does decay before the calorimeter, the major-
 3102 ity of its energy is carried away by the LSP and not deposited in the calorimeter.
 3103 In both cases the energy is expected to be distributed across the layers of the
 3104 calorimeters and not peaked in just one layer. This can be quantified in terms
 3105 of E/p , the ratio of calorimeter energy of a nearby jet to the track momentum,
 3106 and f_{EM} , the fraction of energy in that jet within the electromagnetic calorime-
 3107 ter. When no jets fall within a cone of 0.05 of the particle, E/p and f_{EM} are both
 3108 defined as zero. E/p is expected to be above 1.0 for typical SM particles because
 3109 of calibration and the contributions from other nearby particles, as discussed in
 3110 Chapter 8. At these momenta there is no significant zero fraction due to inter-
 3111 actions with the detector or insufficient energy deposits (see Section 8.2.2). f_{EM}
 3112 is peaked close to 1.0 for electrons, and distributed between 10% and 90% for
 3113 hadrons.

3114 These trends can be seen in the two dimensional distribution for signal in
 3115 Figure 76 for stable and metastable (10 ns) events. The majority of R-Hadrons
 3116 in both samples fall into the bin for $E/p = 0$ and $f_{\text{EM}} = 0$ because the majority
 3117 of the time there is no associated jet. In the stable sample, when there often is
 3118 an associated jet, E/p is typically still below 0.1, and the f_{EM} is predominantly
 3119 under 0.8. In the metastable sample, on the other hand, E/p is larger but still
 3120 typically below 0.1 because of actual jets produced during the decay. The f_{EM} is
 3121 much lower on average in this case, below 0.1, because the 10 ns lifetime particles
 3122 rarely decay before passing through the electromagnetic calorimeter. Figure 76
 3123 also includes simulated Z decays to electrons or tau leptons. From the decays

3124 to electrons it is clear that the majority of electrons have f_{EM} above 0.9. The
 3125 tau decays include a variety of products. Muons can be seen in the bin where
 3126 $E/p = 0$ and $f_{\text{EM}} = 0$ because they do not have an associated jet. Electrons fall
 3127 into the range where $E/p > 1$ and $f_{\text{EM}} > 0.9$. Hadronic tau decays are the most
 3128 common, and fall in the range of $0.1 < f_{\text{EM}} < 0.9$ and $E/p > 1.0$.

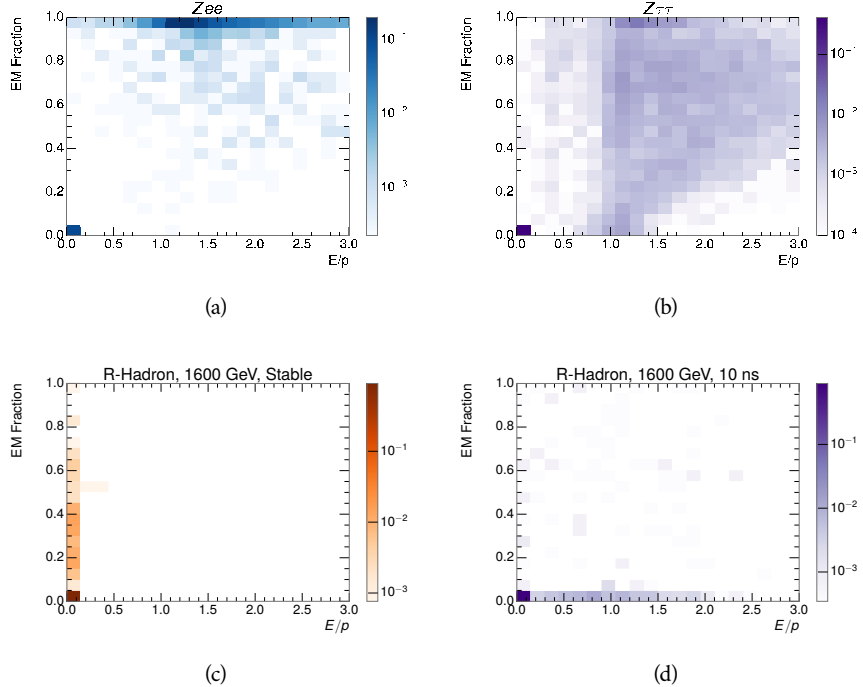


Figure 76: The normalized, two-dimensional distribution of E/p and f_{EM} for simulated
 (a) $Z \rightarrow ee$, (b) $Z \rightarrow \tau\tau$, (c) 1200 GeV Stable R-Hadron events, and (d) 1200
 GeV, 10 ns R-Hadron events.

3129 These differences motivate an electron rejection by requiring an f_{EM} below
 3130 0.9. Similarly, isolated hadrons are rejected by requiring $E/p < 1.0$. These re-
 3131 quirements combine to remove the majority of isolated electrons and hadrons
 3132 but retain over 95% of the simulated signal across a range of masses and lifetimes.

3133 11.4 IONIZATION

3134 The final requirement on the candidate track is the primary discriminating vari-
 3135 able, the ionization in the pixel detector. That ionization is measured in terms
 3136 of dE/dx , which was shown for data and simulated signal events in Figure 72.
 3137 dE/dx is dramatically greater for the high mass signal particles than the back-
 3138 grounds, which start to fall immediately after the minimally ionizing peak at 1.1
 3139 $\text{MeV g}^{-1} \text{cm}^2$. The dE/dx for candidate tracks must be greater than a pseudorapidity-
 3140 dependent threshold, specifically $1.80 - 0.11|\eta| + 0.17\eta^2 - 0.05\eta^3 \text{ MeV g}^{-1} \text{ cm}^{-2}$,
 3141 in order to correct for an approximately 5% dependence of the MIP peak on η .
 3142 The requirement was chosen as part of the signal region optimization, and man-

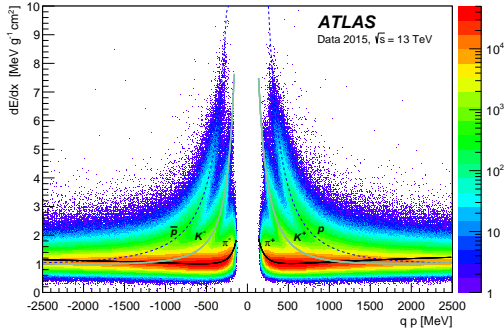


Figure 77: Two-dimensional distribution of dE/dx versus charge signed momentum (qp) for minimum-bias tracks. The fitted distributions of the most probable values for pions, kaons and protons are superimposed.

ages to reduce the backgrounds by a factor of 100 while remaining 70-90% efficient for simulated signal events depending on the mass.

11.4.1 MASS ESTIMATION

The mean value of ionization in silicon is governed by the Bethe equation and the most probable value follows a Landau-Vavilov distribution [9]. Those forms inspire a parametric description of dE/dx in terms of $\beta\gamma$,

$$(dE/dx)_{MPV}(\beta\gamma) = \frac{p_1}{\beta^{p_3}} \ln(1 + [p_2 \beta\gamma]^{p_5}) - p_4 \quad (21)$$

which performs well in the range $0.3 < \beta\gamma < 1.5$. This range includes the expected range of $\beta\gamma$ for the particles targeted for this search, with $\beta\gamma \approx 2.0$ for lower mass particles ($O(100 \text{ GeV})$) and up to $\beta\gamma \approx 0.5$ for higher mass particles ($O(1000 \text{ GeV})$). The parameters, p_i , are fit using a 2015 data sample of low-momentum pions, kaons, and protons as described in Ref. [85]. Figure 77 shows the two-dimensional distribution of dE/dx and momentum along with the above fitted values for $(dE/dx)_{MPV}$.

The above equation (21) is then numerically inverted to estimate $\beta\gamma$ and the mass for each candidate track. In simulated signal events, the mean of this mass value reproduces the generated mass up to around 1800 GeV to within 3%, and 3% shift is applied to correct for this difference. The mass distributions prior to this correction are shown for a few stable mass points in Figure 78. The large widths of these distributions come from the high variability in energy deposits in the pixel detector as well as the uncertainty on momentum measurements at high momentum, but the means converge to the expected values.

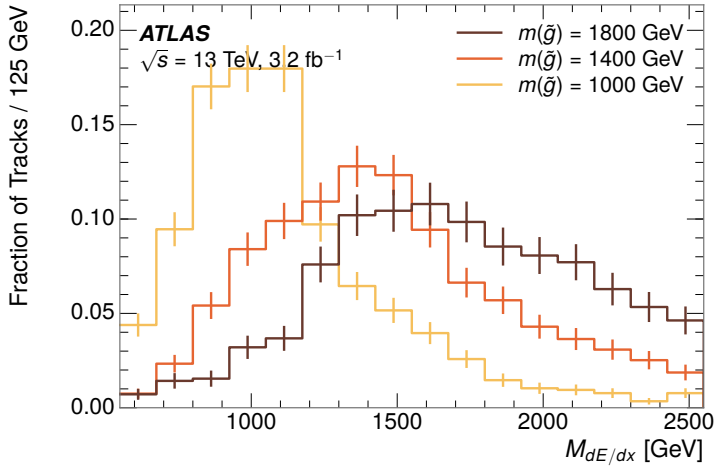


Figure 78: The distribution of mass estimated using dE/dx for simulated stable R-Hadrons with masses between 1000 and 1600 GeV.

This analysis evaluates expected yields and the resulting cross sectional limits using windows in this mass variable. The windows are formed by fitting mass distributions in simulated signal events like those in Figure 78 to Gaussian distributions and taking all events that fall within $\pm 1.4\sigma$ of the mean. As can be seen in Figure 78, typical values for this width are $\sigma \approx 300 - 500$ GeV depending on the generated mass.

11.5 EFFICIENCY

The numbers of events passing each requirement through ionization are shown in Table 9 for the full 2015 dataset and a simulated 1600 GeV, 10 ns lifetime R-Hadron sample. The table highlights the overall acceptance \times efficiency for signal events, which for this example is 19%. Between SM rejection and ionization, this signal region reduces the background of tracks which pass the kinematic requirements down by an additional factor of almost 2000.

There is a strong dependence of this efficiency on lifetime and mass, with efficiencies dropping to under 1% at low lifetimes. Figure 79 shows the dependence on both mass and lifetime for all signal samples considered in this search. The dependence on mass is relatively slight and comes predominantly from the increasing fraction of R-Hadrons which pass the ionization cut with increasing mass. The trigger and E_T^{miss} requirements are most efficient for particles that decay before reaching the calorimeters. However, the chance of a particle to be reconstructed as a high-quality track decreases significantly at low lifetimes as the particle does not propagate sufficiently through the inner detector. These effects lead to a maximum in the selection efficiency for lifetimes around 10-30 ns.

The inefficiency of this signal region at short lifetimes comes almost exclusively from an acceptance effect, in that the particles do not reach the necessary

Selection	Exp. Signal Events	Observed Events in 3.2 fb^{-1}
Generated	26.0 ± 0.3	
E_T^{miss} Trigger	24.8 ± 0.3 (95%)	
$E_T^{\text{miss}} > 130 \text{ GeV}$	23.9 ± 0.3 (92%)	
Track Quality and $p_T > 50$	10.7 ± 0.2 (41%)	368324
Isolation Requirement	9.0 ± 0.2 (35%)	108079
Track $p > 150 \text{ GeV}$	6.6 ± 0.2 (25%)	47463
$M_T > 130 \text{ GeV}$	5.8 ± 0.2 (22%)	18746
Electron and Hadron Veto	5.5 ± 0.2 (21%)	3612
Muon Veto	5.5 ± 0.2 (21%)	1668
Ionization Requirement	5.0 ± 0.1 (19%)	11

Table 9: The expected number of events at each level of the selection for metastable $1600 \text{ GeV}, 10 \text{ ns}$ R-Hadrons, along with the number of events observed in data, for 3.2 fb^{-1} . The simulated yields are shown with statistical uncertainties only. The total efficiency \times acceptance is also shown for the signal.

3190 layers of the SCT. This can be seen more clearly by defining a fiducial region
 3191 which includes events with at least one R-Hadron that is produced with non-
 3192 zero charge, $p_T > 50 \text{ GeV}$, $p > 150 \text{ GeV}$, $|\eta| < 2.5$, and a decay distance greater
 3193 than 37 cm in the transverse plane. At short (1 ns) lifetimes, the acceptance into
 3194 this region is as low as 4%. Once this acceptance is accounted for, the selection
 3195 efficiency ranges from 25% at lifetimes of 1 ns up to 45% at lifetimes of 10 ns.

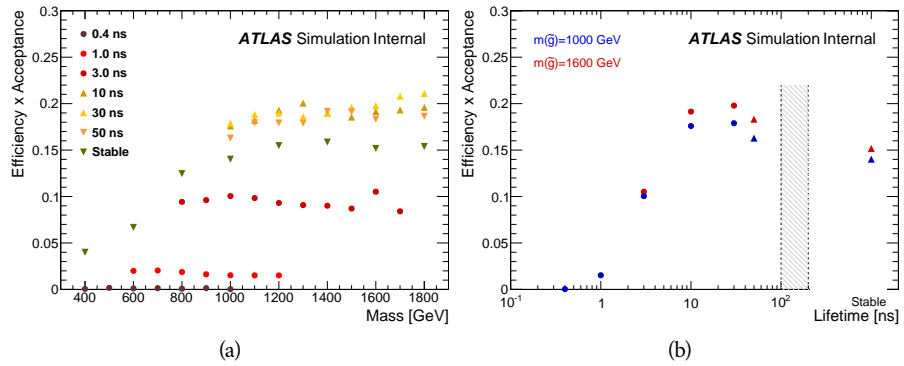


Figure 79: The acceptance \times efficiency as a function of R-Hadron (a) mass and (b) lifetime. (a) shows all of the combinations of mass and lifetime considered in this search, and (b) highlights the lifetime dependence for 1000 GeV and 1600 GeV R-Hadrons.

3196

3197 BACKGROUND ESTIMATION

3198 The event selection discussed in the previous section focuses on detector signa-
 3199 tures, emphasizing a single high-momentum, highly-ionizing track. That track
 3200 is then required to be in some way inconsistent with the expected properties
 3201 of SM particles, with various requirements designed to reject jets, hadrons,
 3202 electrons, and muons (Section 11.3). Therefore the background for this search comes
 3203 entirely from reducible backgrounds that are outliers of various distributions in-
 3204 cluding dE/dx , f_{EM} , and p_T^{Cone} . The simulation can be tuned in various ways to
 3205 do an excellent job of modeling the average properties of each particle type [86],
 3206 but it is not necessarily expected to accurately reproduce outliers. For this rea-
 3207 sons, the background estimation used for this search is estimated entirely using
 3208 data.

3209 12.1 BACKGROUND SOURCES

3210 SM charged particles with lifetimes long enough to form tracks in the inner de-
 3211 tector can be grouped into three major categories based on their detector inter-
 3212 actions: hadrons, electrons, and muons. Every particle that enters into the back-
 3213 ground for this search belongs to one of these types. Relatively pure samples of
 3214 tracks from each of these types can be formed in data by inverting the various
 3215 rejection techniques in Section 11.3. Specifically, muons are selected requiring
 3216 medium muon identification, electrons requiring $E/p > 1.0$ and $f_{EM} > 0.95$,
 3217 and hadrons requiring $E/p > 1.0$ and $f_{EM} < 0.95$.

3218 Figure 80 shows the distributions of momentum and dE/dx for these cate-
 3219 gories in data, after requiring the event level selection as well as the track re-
 3220 quirements on p_T , hits, and N_{split} , as discussed in Section 11.2. Simulated signal
 3221 events are included for reference. These distribution are only illustrative of the
 3222 differences between types, as the rejection requirements could alter their shape.
 3223 This is especially significant for momentum which enters directly into E/p and
 3224 can indirectly affect muon identification. However the various types show clear
 3225 differences in both distributions. The distributions of momentum are not nec-
 3226 cessarily expected to match between the various types because the production
 3227 mechanisms for each type result in different kinematic distributions. dE/dx is
 3228 also different between types because of incomplete isolation; although the re-
 3229 quirement on N_{split} helps to reduce the contribution of nearby particles it does
 3230 not completely remove the effect of overlaps. Muons are better isolated because
 3231 they do not have the additional particle from hadronization present for hadrons
 3232 and they are significantly less likely do interact with the detector and produce
 3233 secondary particles compared to hadrons and electrons. Thus muons have the
 3234 smallest fraction of dE/dx above the threshold of $1.8 \text{ MeVg}^{-1}\text{cm}^2$; hadrons and
 3235 electrons have a larger fraction above this threshold.

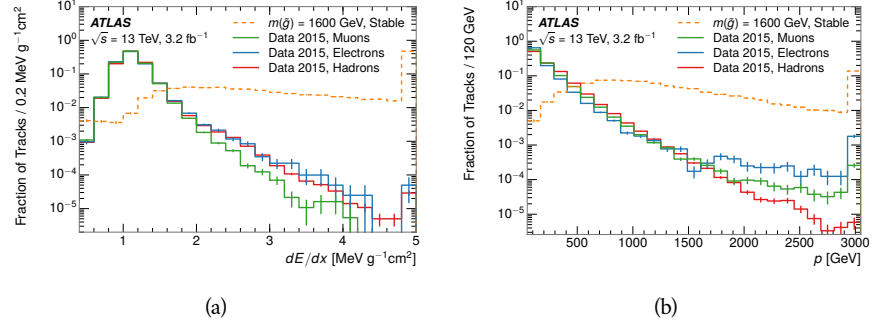


Figure 80: The distribution of (a) dE/dx and (b) momentum for tracks in data and simulated signal after requiring the event level selection and the track selection on p_T , hits, and N_{split} . Each sub-figure shows the normalized distributions for tracks classified as hadrons, electrons, and muons in data and R-Hadrons in the simulated signal.

3236 It is difficult to determine what fraction of each particle type enters into the fi-
 3237 nal signal region. The background method will not have significant dependence
 3238 on the relative contributions of each species, but it is useful to understand the
 3239 differences between each when considering the various tests of the method.

3240 12.2 PREDICTION METHOD

3241 The data-driven background estimation relies on the independence between ion-
 3242 ization and other kinematic variables in the event. For standard model particles
 3243 with momenta above 50 GeV, dE/dx is not correlated with momentum; though
 3244 there is a slight relativistic rise as momentum increases, the effect is small com-
 3245 pared to the width of the distribution of ionization energy deposits.. So, the
 3246 proposed method to estimate the mass distribution of the signal region is to use
 3247 momentum from a track with low dE/dx (below the threshold value) and to com-
 3248 bine it with a random dE/dx value from a dE/dx template. The resulting track is
 3249 just as likely as the original, so a number of such random generations provide the
 3250 expected distributions of momentum and ionization. These are then combined
 3251 using the parametrization described in Section 11.4.1 to form a distribution of
 3252 mass for the signal region.

3253 Algorithmically this method is implemented by forming two distinct Control
 3254 Regions (**CR**s). The first **CR**, CR1, is formed by applying the entire event selec-
 3255 tion from Chapter 11 up to the dE/dx and mass requirements. The dE/dx re-
 3256 quirement is instead inverted for this region. Because of the independence of
 3257 dE/dx , the tracks in this control region have the same kinematic distribution
 3258 as the tracks in the signal region, and are used to measure a two-dimensional
 3259 template of p and η . The second **CR**, CR2, is formed from the event selection
 3260 through the dE/dx requirement, but with an inverted E_T^{miss} requirement. The
 3261 tracks in this control region are expected to have similar dE/dx distributions to
 3262 the signal region before the ionization requirement, and so this region is used to
 3263 measure a two-dimensional template of dE/dx and η .

3264 The contribution of any signal to the control regions is minimized by the in-
 3265 verted selection requirements. Only less than 10% of simulated signal events
 3266 have either dE/dx or E_T^{miss} below the threshold values in the original signal re-
 3267 gion, while the backgrounds are significantly enhanced by inverting those re-
 3268 quirements. The signal contamination is less than 1% in both control regions
 3269 for all of the simulated masses and lifetimes considered in this analysis.

3270 With those measured templates, the shape of the mass estimation is generated
 3271 by first selecting a random (p, η) combination from CR1. This momentum
 3272 value is combined with a dE/dx value taken from the appropriate distribution
 3273 of dE/dx for the selected η from CR2. The use of η in both random samplings
 3274 controls for any correlation between p , dE/dx , and η . Those values are then
 3275 used to calculate a mass in the same way that is done for regular tracks in data,
 3276 see Section 11.4.1. As this procedure includes all dE/dx values, the cut at 1.8
 3277 MeVg $^{-1}$ cm 2 is then enforced to fully model the signal region. The generated
 3278 mass distribution is then normalized by scaling the background estimate to the
 3279 data in the region $M < 160$ GeV, where signals of this type have already been
 3280 excluded [70]. This normalization uses the distributions of mass generated with-
 3281 out the ionization requirement.

3282 The statistical uncertainties on these background distributions are calculated
 3283 by independently fluctuating each bin of the input templates according to their
 3284 Poisson uncertainties. These fluctuations are repeated a large number of times,
 3285 and the uncertainty on the resulting distribution is taken as the root mean square
 3286 (RMS) deviation of the fluctuations from the average. As the procedure uses one
 3287 million random combinations to generate the distributions, The statistical un-
 3288 certainty from the actual random generations is negligible compared to the un-
 3289 certainty from measuring the templates.

3290 12.3 VALIDATION

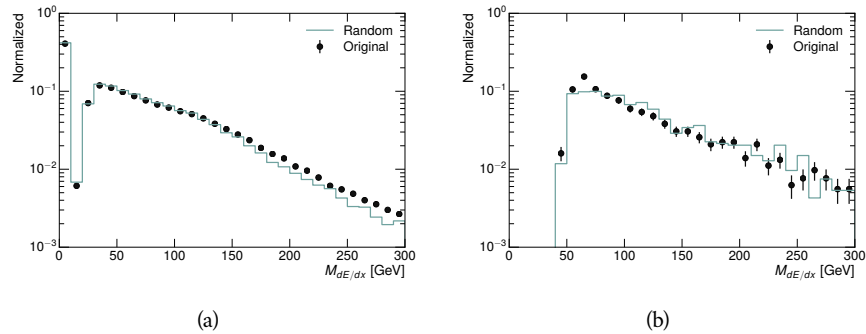
3291 The validity of the background estimation technique can be evaluated in both
 3292 data and simulation. The underlying assumption that random combinations of
 3293 dE/dx and momentum can predict a mass distribution in an orthogonal region
 3294 can be tested using simulated samples where concerns like multiple particle types
 3295 can be controlled. Using the same technique in another set of signal-depleted
 3296 regions in data then extends this confidence to the more complicated case where
 3297 several particle species are inherently included.

3298 12.3.1 CLOSURE IN SIMULATION

3299 The first test of the procedure is done using a simulated sample of $W \rightarrow \mu\nu$
 3300 decays. These types of events provide the ingredients required to test the back-
 3301 ground estimate, E_T^{miss} and isolated tracks, with high statistics. In this example
 3302 there is no signal, so simulated events in the orthogonal CRs are used to estimate
 3303 the shape of the mass distribution of the simulated events in the signal region. To
 3304 reflect the different topology for W boson decays, the CRs use slightly modified
 3305 definitions. In all CRs, the requirement of $p > 150$ GeV and the SM rejection

3306 requirements are removed. Additionally, for the signal region the requirement
 3307 on E_T^{miss} is relaxed to 30 GeV and the corresponding inverted requirement on
 3308 CR2 is also set at 30 GeV.

3309 With these modified selections, the simulated and randomly generated distri-
 3310 butions of $M_{dE/dx}$ are shown in Figure 81. This figure includes the mass distri-
 3311 butions before and after the requirement on dE/dx , which significantly shapes
 3312 the distributions. In both cases the background estimation technique repro-
 3313 duces the shape of $M_{dE/dx}$ in the signal region. There is a small difference in the pos-
 3314 itive tail of the mass distribution prior to the ionization cut, where the random
 3315 events underestimate the fraction of tracks with mass above 150 GeV by about
 3316 20%. After the ionization requirement, however, this discrepancy is not present
 3317 and the two distributions agree to within statistical uncertainties.



3318 Figure 81: The distribution of $M_{dE/dx}$ (a) before and (b) after the ionization requirement
 3319 for tracks in simulated W boson decays and for the randomly generated back-
 3320 ground estimate.

3321 This ability to reproduce the shape of the mass distribution in simulated events
 3322 shows that the technique works as expected. No significant biases are acquired
 3323 in using low dE/dx events to select kinematic templates or in using low E_T^{miss}
 3324 events to select ionization templates, as either would result in a mismodeling of
 3325 the shape of the mass distribution. The simulated events contain only one par-
 3326 ticle type, however, so this test only establishes that the technique works well
 3327 when the the CRs are populated by exactly the same species.

3328 12.3.2 VALIDATION REGION IN DATA

3329 The second test of the background estimate is performed using data in an or-
 3330 thogonal validation region. The validation region, and the corresponding CRs,
 3331 are formed using the same selection requirements as in the nominal method but
 3332 with a modified requirement on momentum, $50 < p[\text{GeV}] < 150$. This allows
 3333 the technique to be checked in a region with very similar properties but where
 3334 the signal is depleted, as the majority of the signal has momentum above 150
 3335 GeV while the backgrounds are enhanced below that threshold. Any biases on
 3336 the particle composition of the CRs for the signal region will be reflected in the
 3337 CRs used to estimate the mass distribution in the validation region.

3335 Figure 82 shows the measured and randomly generated mass distributions for
 3336 data before and after the ionization requirement. The background estimate does
 3337 an excellent job of modeling the actual background before the ionization require-
 3338 ment, with good agreement to within the statistical uncertainties out to the limit
 3339 of the mass distribution. There are very few events in the validation region after
 3340 the ionization requirement, but the few observed events are consistent with the
 3341 background prediction. The good agreement in this validation region provides
 3342 a confirmation that the technique works even in the full-complexity case with
 3343 multiple particle types entering the distributions. Any bias from changes in par-
 3344 ticle composition between regions is small compared to statistical uncertainties.

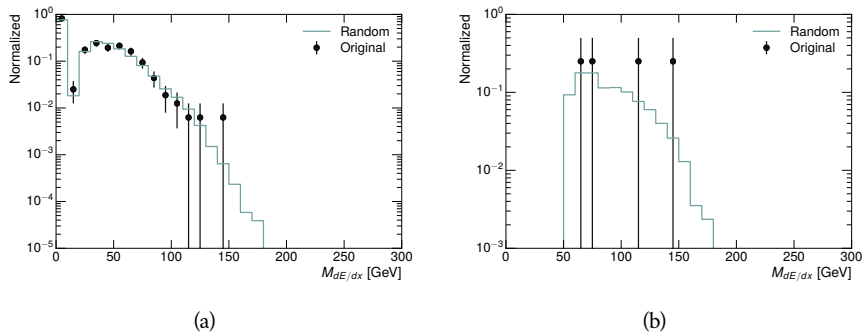


Figure 82: The distribution of $M_{dE/dx}$ (a) before and (b) after the ionization require-
 ment for tracks in the validation region and for the randomly generated back-
 ground estimate.

3345

3346 SYSTEMATIC UNCERTAINTIES AND RESULTS

3347 13.1 SYSTEMATIC UNCERTAINTIES

3348 A number of systematic uncertainties affect the interpretation of the results of
 3349 the search. These uncertainties can broken down into two major categories,
 3350 those which affect the estimate of the background using data and those which
 3351 affect the measurement of the signal yield estimated with simulated events. The
 3352 total measured systematic uncertainties are 7% for the background estimation
 3353 and approximately 32% for the signal yield depending on lifetime. These system-
 3354 atic uncertainties are expected to be small compared to the statistical fluctuations
 3355 of the measured yields so that measured cross-sectional limits will be dominated
 3356 by statistical uncertainties. The following sections describe each source of sys-
 3357 tematic uncertainty for each of the two types.

3358 13.1.1 BACKGROUND ESTIMATE

3359 The systematic uncertainties on the background estimate come primarily from
 3360 considering alternative methods for generating the background distributions.
 3361 These uncertainties are small compared to the statistical uncertainties on the
 3362 background estimate which come from the limited statistics in measuring the
 3363 template distributions, as described in Section 12.2. They are summarized in
 3364 Table 10.

Source of Uncertainty:	Value [%]
Analytic Description of dE/dx	4.0
Muon Fraction (Stable Region only)	3.0
IBL Ionization Correction	3.8
Normalization	3.0
Total (Metastable Region):	6.3
Total (Stable Region):	7.0

Table 10: A summary of the sources of systematic uncertainty for the data-driven background in the signal region. If the uncertainty depends on the mass, the maximum values are reported.

3365 13.1.1.1 ANALYTIC DESCRIPTION OF DE/DX

3366 The background estimate uses a binned template distribution to estimate the
 3367 dE/dx of tracks in the signal region, as described in Section 12.2. It is also possi-

ble to fit that measured distribution to a functional form to help smooth the distribution in the tails of dE/dx where the template is driven by a small number of tracks. Both Landau convolved with a Gaussian and Crystal Ball functions are considered as the functional form and used to re-estimate the background distribution. The deviations compared to the nominal method are found to be 4%, and this is taken as a systematic uncertainty to cover the inability carefully predict the contribution from the long tail of dE/dx where there are few measurements available in data.

3376 13.1.1.2 MUON FRACTION

3377 The stable region of the analysis explicitly includes tracks identified as muons,
 3378 which have a known difference in their dE/dx distributions compared to non-
 3379 muon tracks (Section 12.1). To account for a difference in muon fraction be-
 3380 tween the background region and the signal region for this selection, the dE/dx
 3381 templates for muons and non-muons are measured separately and then the rel-
 3382 ative fraction of each is varied in the random generation. The muon fraction
 3383 is varied by its statistical uncertainty and the resulting difference of 3% in back-
 3384 ground yield is taken as the systematic uncertainty.

3385 13.1.1.3 IBL CORRECTIONS

3386 The IBL, described in Section 6.3.1, received a significant dose of radiation during
 3387 the data collection in 2015. The irradiation can cause a drift in the frontend
 3388 electronics and thus alter the dE/dx measurement which includes the ToT output
 3389 by the IBL. These effects are corrected for in the nominal analysis by scaling the
 3390 dE/dx measurements by a constant factor derived for each run to match the
 3391 average dE/dx value to a reference run where the IBL was known to be stable
 3392 to this effect. However, this corrective factor does not account for inter-run
 3393 variations. To account for this potential drift of dE/dx , the correction procedure
 3394 is repeated by varying the corrections up and down by the maximal run-to-run
 3395 variation from the full data-taking period, which results in an uncertainty of
 3396 3.8%.

3397 13.1.1.4 NORMALIZATION

3398 As described in Section 12.2, the generated distribution of masses is normalized
 3399 in a shoulder region ($M < 160$ GeV) where signals have been excluded by pre-
 3400 vious analyses. That normalization factor is varied by its statistical uncertainty
 3401 and the resulting fluctuation in the mass distribution of 3% is taken as a system-
 3402 atic uncertainty on the background estimate.

3403 13.1.2 SIGNAL YIELD

3404 The systematic uncertainties on the signal yield can be divided into three cate-
 3405 gories; those on the simulation process, those on the modeling of the detector
 3406 efficiency or calibration, and those affecting the overall signal yield. They are
 3407 summarized in Table 10. The largest uncertainty comes from the uncertainty

3408 on the production cross section for gluinos, which is the dominant systematic
 3409 uncertainty in this analysis.

Source of Uncertainty	-[%]	+[%]
ISR Modeling (Metastable Region)	1.5	1.5
ISR Modeling (Stable Region)	14	14
Pile-up Reweighting	1.1	1.1
Trigger Efficiency Reweighting	0.9	0.9
E_T^{miss} Scale	1.1	2.2
Ionization Parametrization	7.1	0
Momentum Parametrization	0.3	0.0
Electron Rejection	0.0	0.0
Hadron Rejection	0.0	0.0
μ Identification	4.3	4.3
Luminosity	5	5
Signal size uncertainty	28	28
Total (Metastable Region)	30	29
Total (Stable Region)	33	32

Table 11: A summary of the sources of systematic uncertainty for the simulated signal yield. The uncertainty depends on the mass and lifetime, and the maximum negative and positive values are reported in the table.

3410 13.1.2.1 ISR MODELING

3411 As discussed in Section 10.2, MadGraph is expected to reproduce the distribution
 3412 of ISR in signal events more accurately than the nominal Pythia samples. The
 3413 analysis reweights the distribution of ISR in the simulated signal events to match
 3414 the distribution found in generated MadGraph samples. This has an effect on the
 3415 selection efficiency in the signal samples, where ISR contributes to the generation
 3416 of E_T^{miss} . To account for the potential inaccuracy on the simulation of ISR at high
 3417 energies, half of the difference between the signal efficiency with the reweighted
 3418 distribution and the original distribution is taken as a systematic uncertainty.

3419 13.1.2.2 PILEUP REWEIGHTING

3420 The simulated events were generated prior to data collection with an estimate of
 3421 the average number of interactions per bunch crossing. This estimate does not
 3422 match the value of pileup during actual data collection, but a large fraction of the
 3423 simulated events would be discarded in order to match the distribution in data.
 3424 Therefore the simulated signal events are not reweighted for pileup by default
 3425 in the analysis. The effect of the pileup on signal efficiency is not expected to
 3426 depend on the mass or lifetime of the generated signal events, which allows all

3427 of the generated signal events to be used together to assess the pileup dependence.
 3428 To account for the potential effect of the difference in the number of interactions
 3429 per bunch crossing between data and simulation, the difference in yield between
 3430 the nominal signal events and the reweighted events averaged over all masses
 3431 and lifetimes is taken as a systematic uncertainty on the yield for each mass and
 3432 lifetime (1.1%).

3433 13.1.2.3 TRIGGER EFFICIENCY REWEIGHTING

3434 As described in Section 11.2, the selection for this analysis does not require a suf-
 3435 ficiently large value of E_T^{miss} to be above the plateau of trigger efficiency. There-
 3436 fore, some signal events which would otherwise pass the event selection can be
 3437 excluded because of the trigger requirement. These effects can be difficult to es-
 3438 timate in simulation, and thus are constrained by comparing data and simulated
 3439 events in an alternative W boson region which uses decays to muons to find a rel-
 3440 atively pure sample of events with missing energy. The trigger efficiency for data
 3441 and simulated W events are shown in Figure 83. The comparison between data
 3442 and MC in this region constrains the simulation of the trigger efficiency. The
 3443 simulated signal events are reweighted by the ratio of data to simulation in the
 3444 W boson decays, while the difference between the data and simulation in those
 3445 decays is taken as a systematic uncertainty. This results in an uncertainty of only
 3446 0.9% as the majority of events are well above the plateau and the disagreement
 3447 between data and simulation is small even below that plateau.

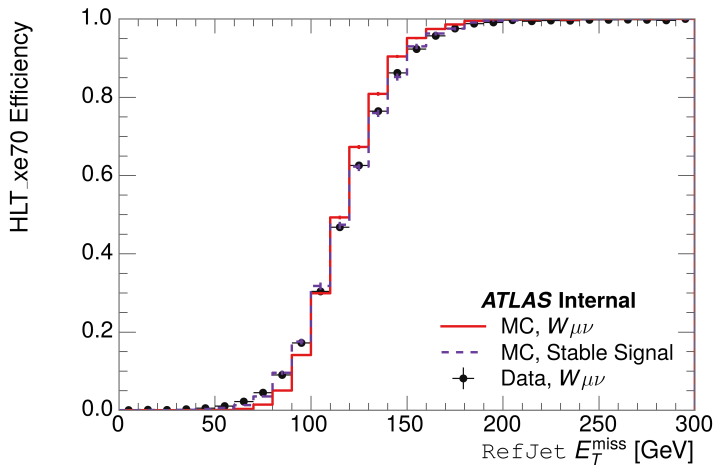


Figure 83: The trigger efficiency for the HLT_xe70 trigger requirement as a function of Calorimeter E_T^{miss} for simulated data events with a W boson selection. Simulated signal events and simulated W boson events are also included.

3448 13.1.2.4 MISSING TRANSVERSE MOMENTUM SCALE

3449 The ATLAS Combined Performance (CP) group provides a default recommenda-
 3450 tion for systematic variations of jets and missing energy (**note: I'm not quite**
 3451 **sure what to cite for this - I don't see any papers from the jet/met group**

Systematic Variation	-[%]	+[%]
JET_GroupedNP_1	-0.7	1.3
JET_GroupedNP_2	-0.7	1.2
JET_GroupedNP_3	-0.5	1.3

Table 12: Example of the contributing systematic variations to the total systematic for the E_T^{miss} Scale, as measured in a 1200 GeV, Stable R-Hadron signal sample.

after this was implemented). These variations enter into this analysis only in the requirement on E_T^{miss} . The effect of the measured scale of E_T^{miss} is evaluated by varying the E_T^{miss} scale according to the one sigma variations provided by all CP recommendations on objects affecting event kinematics in simulated signal events. Missing energy is reconstructed from fully reconstructed objects so any systematic uncertainties affecting jets, muons, electrons, or the E_T^{miss} soft terms are included. The only non-negligible contributions found using this method are itemized in Table 12 for an example signal sample (1200 GeV, Stable R-Hadron), where the systematic is measured as the relative difference in the final signal efficiency after applying the associated variation through the CP tools. The only variations that are significant are the grouped jet systematic variations, which combine recommended jet systematic uncertainties into linearly independent variations.

As the peak of the reconstructed E_T^{miss} distribution in the signal is significantly above the current threshold for events which pass the trigger requirement, the effect of scale variation is expected to be small, which is consistent with the measured systematic of approximately 2%. Events which do not pass the trigger requirement usually fail because there are no ISR jets in the event to balance the R -hadrons' transverse momentum, so the reconstructed E_T^{miss} is low and therefore also expected to be not very sensitive to scale changes.

13.1.2.5 MOMENTUM PARAMETRIZATION

The uncertainty on the signal efficiency from track momentum is calculated using the CP group recommendations for tracks. In particular, only one recommended systematic variation affects track momentum, the sagitta bias for q/P . This uncertainty is propagated to the final selection efficiency by varying the track momentum by the recommended one sigma variation, and the associated uncertainty is found to be negligible (0.3%).

13.1.2.6 IONIZATION REQUIREMENT

The dE/dx distributions in data and simulated events have different most probable values, which is due in part to radiation effects in the detector that are not fully accounted for in the simulation. The difference does not affect the mass measurement used in this analysis, as independent calibrations are done in simulation and in data. However, it does affect the efficiency of the high dE/dx selection requirement. To calculate the size of the effect on the signal efficiency,

3486 the dE/dx distribution in signal simulation is scaled by a scale factor obtained
 3487 from comparing the dE/dx distribution of inclusive tracks in data and in sim-
 3488 ulation. The difference in efficiency for this sample with a scaled dE/dx dis-
 3489 tribution, relative to the nominal case, is taken as a systematic uncertainty on
 3490 signal efficiency. The uncertainty is as large as 7% for low masses and falls to a
 3491 negligible effect for large masses.

3492 13.1.2.7 ELECTRON AND JET REJECTION

3493 The systematic uncertainty on the electron rejection is measured by varying the
 3494 EM fraction requirement significantly, from 0.95 to 0.9. This is found to have
 3495 a less than 0.04% effect on signal acceptance, on average, and so is completely
 3496 negligible. Similarly, the uncertainty on jet rejection is measured by tightening
 3497 the E/p requirement from 0.5 to 0.4. This is found to have no effect on signal
 3498 acceptance, so again the systematic is again negligible.

3499 13.1.2.8 MUON VETO

3500 The metastable signal region requires that the candidate tracks are not identi-
 3501 fied as medium muons because the majority of R-Hadrons in the lifetime range
 3502 included in that region do not reach the muon spectrometers before they de-
 3503 cay. However, the exponential tail of the R-Hadron lifetime distribution results
 3504 in some R-Hadrons traversing the muon spectrometer. These can still fail the
 3505 muon medium identification because they can fail on the requirement on the
 3506 number of precision hits required to pass the loose selection because they ar-
 3507 rive late to the muon spectrometer. This can be seen in Figure 84, which shows
 3508 the efficiency of the muon veto as a function of $1/\beta$, for two simulated stable
 3509 R-Hadron samples.

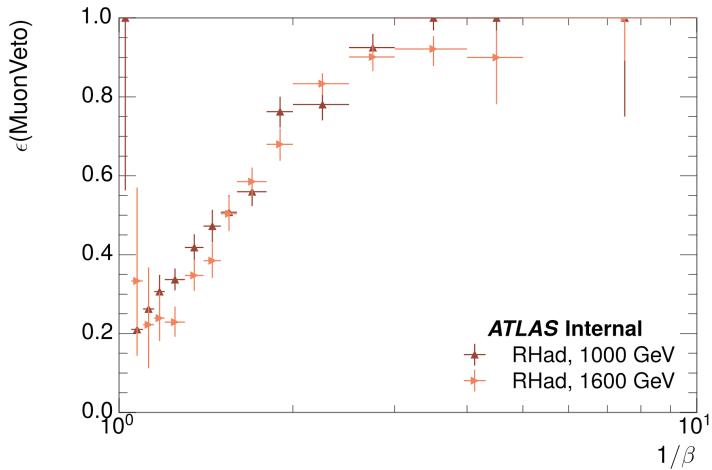


Figure 84: The efficiency of the muon veto for R -hadrons of two different masses, as a function of $1/\beta$ for simulated R-Hadron tracks.

3510 Thus, the efficiency of the muon veto depends on the timing resolution of
 3511 the spectrometer, so an uncertainty is applied to the signal efficiency to cover

3512 differences in timing resolution between data and simulation. First, a sample of
 3513 $Z \rightarrow \mu\mu$ events is selected in data in which one of the muons has a late arrival
 3514 time measured in the MDT. Then the reconstructed β distribution is compared
 3515 to the distribution in simulated $Z \rightarrow \mu\mu$ events; the difference between these
 3516 two distributions reflects the difference in timing resolution between data and
 3517 simulation. To emulate this difference in simulated signal events, the magnitude
 3518 of the difference is used to scale and shift the true β distribution of R-Hadrons in
 3519 simulation. Signal events are then reweighted based on this varied β distribution,
 3520 and the difference in the efficiency of the muon veto selection is compared with
 3521 the nominal and reweighted true β distributions. The difference in muon veto
 3522 efficiency is taken as a systematic uncertainty of the muon veto.

3523 The comparison of reconstructed β between data and simulation is performed
 3524 separately in the barrel, transition, and endcap regions of the spectrometer, and
 3525 the reweighting of the true β distribution in signal is done per region. The com-
 3526 parison of average reconstructed MDT β between data and simulation for the
 3527 barrel region is shown in Figure 85 for $Z \rightarrow \mu\mu$ events. As expected, The uncer-
 3528 tainty is found to be negligible for R-hadrons with short lifetimes, and is only
 3529 significant for lifetimes above 30 ns.

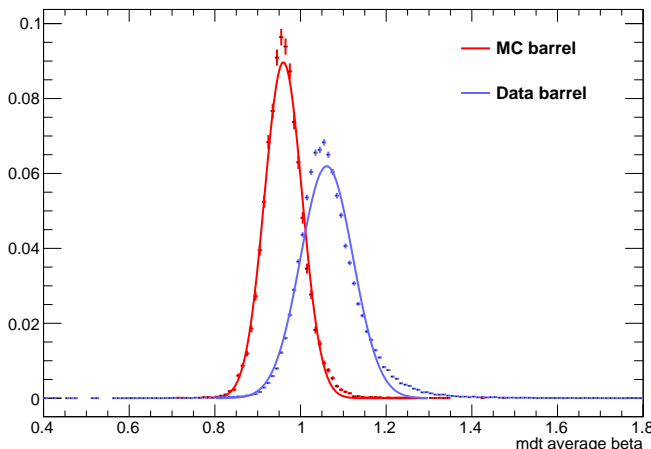


Figure 85: The average reconstructed MDT β distribution for $Z \rightarrow \mu\mu$ events in which
 one of the muons is reconstructed as a slow muon, for both data and simula-
 tion. A gaussian fit is superimposed.

3530 13.1.2.9 LUMINOSITY

3531 The luminosity uncertainty is provided by a luminosity measurement on ATLAS
 3532 and was measured to be 5% at the time of the publication of this analysis.

3533 13.1.2.10 SIGNAL SIZE

3534 As discussed in Section 10.2, the signal cross sections are calculated at NLO in the
 3535 strong coupling constant with a resummation of soft-gluon emission at NLL. The
 3536 uncertainties on those cross sections are between 14% to 28% for the R-Hadrons

Selection Region	Expected Background	Data
Stable	$17.2 \pm 2.6 \pm 1.2$	16
Metastable	$11.1 \pm 1.7 \pm 0.7$	11

Table 13: The estimated number of background events and the number of observed events in data for the specified selection regions prior to the requirement on mass. The background estimates show statistical and systematic uncertainties.

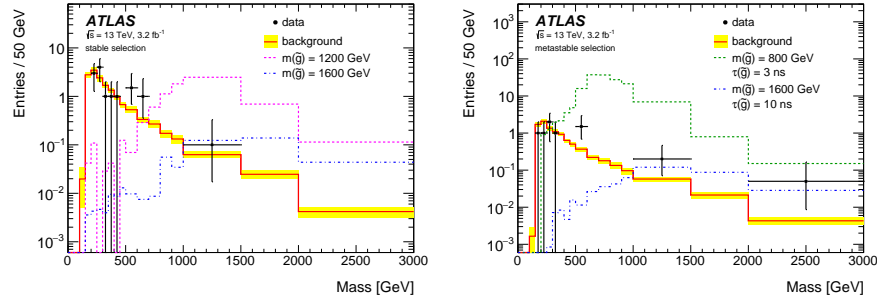


Figure 86: The observed mass distribution of events in data and the generated background distribution in (a) the stable and (b) the metastable signal region. A few example simulated signal distributions are superimposed.

3537 in the range of 400 to 1800 GeV [82, 83], where the uncertainty increases with
 3538 the mass.

3539 13.2 FINAL YIELDS

3540 This full analysis was performed using the 3.2 fb^{-1} from the 2015 data-taking.
 3541 Using the selections discussed in Chapter 11, sixteen events were observed in
 3542 the stable signal region and eleven events were observed in the metastable signal
 3543 region, prior to requirements on the candidate track mass. The background esti-
 3544 mate discussed in Chapter 12 predicts $17 \pm 2.6(\text{stat}) \pm 1.2(\text{syst})$ events for the
 3545 stable region and $11.1 \pm 1.7(\text{stat}) \pm 0.7(\text{syst})$ events for the metastable region.
 3546 These counts are summarized in Table 13.

3547 The mass estimated using dE/dx (Section 11.4.1) provides the final discrimi-
 3548 nating variable, where the signal would be expected as an excess in the falling ex-
 3549 ponential tail of the expected background. The observed distribution of masses
 3550 is shown in Figure 86, along with the predicted distribution from the background
 3551 estimate for each signal region. Both include a few example simulated signal dis-
 3552 tributions, which show the scale of an excess were the R-Hadron signals present.
 3553 There is no statistically significant evidence of an excess in the data over the back-
 3554 ground estimation. From this distribution it is clearly possible to rule out signals
 3555 with lower masses, around 1200 GeV, which have larger cross sections.

3556 13.3 CROSS SECTIONAL LIMITS

3557 Because there is no observed significant excess of events in the signal region, this
 3558 analysis sets upper limits on the allowed cross section for R-Hadron production.
 3559 These limits are set for each mass point by counting the observed events in data,
 3560 along with the expected background and simulated signal events, in windows of
 3561 mass. The mass windows are formed by fitting the distribution of signal events to
 3562 a Gaussian distribution, and the window is then $\pm 1.4\sigma$ around the center of that
 3563 Gaussian. Two examples of the windows formed by this procedure are shown
 3564 in Tables 14-15, for the stable and 10 ns working points. The corresponding
 3565 counts of observed data, expected background, and simulated signal for those
 3566 same working points are shown in Tables 16-17. Appendix B includes the mass
 3567 windows and counts for all of the considered signal points.

$m(\tilde{g})$ [GeV]	Left Extremum [GeV]	Right Extremum [GeV]
1000	655	1349
1100	734	1455
1200	712	1631
1300	792	1737
1400	717	1926
1500	815	2117
1600	824	2122
1700	900	2274
1800	919	2344

Table 14: The left and right extremum of the mass window for each generated mass point with a 10 ns lifetime.

$m(\tilde{g})$ [GeV]	Left Extremum [GeV]	Right Extremum [GeV]
800	627	1053
1000	726	1277
1200	857	1584
1400	924	1937
1600	993	2308
1800	1004	2554

Table 15: The left and right extremum of the mass window used for each generated stable mass point.

3568 The 95% confidence level upper limits on the cross sections for a large grid of
 3569 masses (between 800 and 1800 GeV) and lifetimes (between 0.4 and stable) are
 3570 extracted from these counts with the CL_S method using the profile likelihood

$m(\tilde{g})$ [GeV]	Expected Signal	Expected Background	Observed Data
800	462.83 ± 14.86	1.764 ± 0.080	2.0
1000	108.73 ± 3.38	1.458 ± 0.070	1.0
1200	31.74 ± 0.95	1.137 ± 0.060	1.0
1400	10.22 ± 0.29	1.058 ± 0.058	1.0
1600	3.07 ± 0.09	0.947 ± 0.054	1.0
1800	1.08 ± 0.05	0.940 ± 0.054	1.0

Table 16: The expected number of signal events, the expected number of background events, and the observed number of events in data with their respective statistical errors within the respective mass window for each generated stable mass point

$m(\tilde{g})$ [GeV]	Expected Signal	Expected Background	Observed Data
1000	144.48 ± 5.14	1.499 ± 0.069	2.0
1100	73.19 ± 2.61	1.260 ± 0.060	2.0
1200	41.54 ± 1.41	1.456 ± 0.067	2.0
1300	22.58 ± 0.77	1.201 ± 0.058	2.0
1400	12.70 ± 0.42	1.558 ± 0.071	2.0
1500	6.73 ± 0.24	1.237 ± 0.060	2.0
1600	3.90 ± 0.13	1.201 ± 0.058	2.0
1700	2.27 ± 0.07	1.027 ± 0.052	2.0
1800	1.34 ± 0.04	1.019 ± 0.052	2.0

Table 17: The expected number of signal events, the expected number of background events, and the observed number of events in data with their respective statistical errors within the respective mass window for each generated mass point with a lifetime of 10 ns.

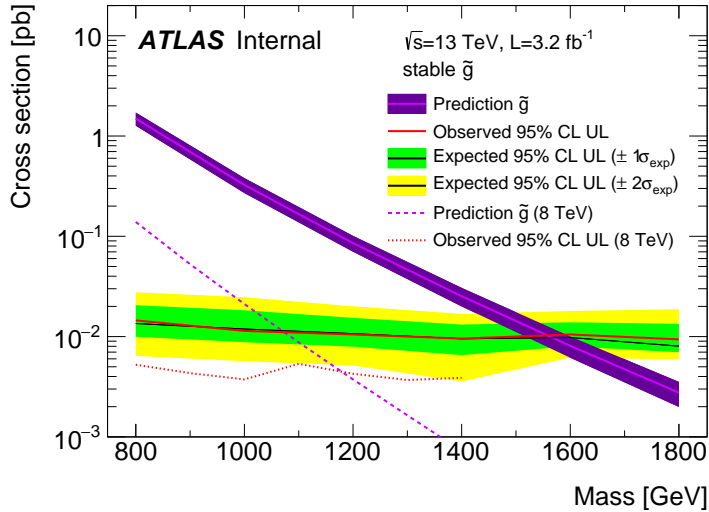


Figure 87: The observed and expected cross section limits as a function of mass for the stable simulated signal. The predicted cross section values for the corresponding signals are included.

ratio as a test statistic [87]. For this procedure, the systematic uncertainties estimated for the signal and background yields are treated as Gaussian-distributed nuisance parameters. The uncertainty on the normalization of the expected background distribution is included in the expected background events. At this point the expected cross section limit is calculated for both the metastable and stable signal region for each lifetime point, and the region with the best expected limit is selected for each lifetime. Using that procedure, the metastable region is used for lifetimes up to and including 30 ns, and the stable region for lifetimes above it.

The resulting cross-sectional upper limits are shown as a function of mass in Figure 87 and Figure 88 for each lifetime considered. The limits are interpolated linearly between each mass point, and the dependence of the limit on the mass is small as the efficiency is relatively constant for large R-Hadron masses. There is however a strong dependence on lifetime, as discussed in Section 11.5, where the probability to form a fully reconstructed track and the kinematic freedom to produce E_T^{miss} result in a local maximum in the limit at 10–30 ns. The figures also include the expected cross section for pair-produced gluino R-Hadrons for reference. For the 10 ns and stable cross section limits, both the observed limit and expected cross section for the Run 1, 8 TeV version of this analysis are included. There the cross sectional limits are lower because of the increased available luminosity, while the signal cross sections were also much lower because of the lower collision energy.

13.4 MASS LIMITS

The cross-sectional limits can then be used to derive a lower mass limit for gluino R-Hadrons by comparing them to the theoretically predicted production cross

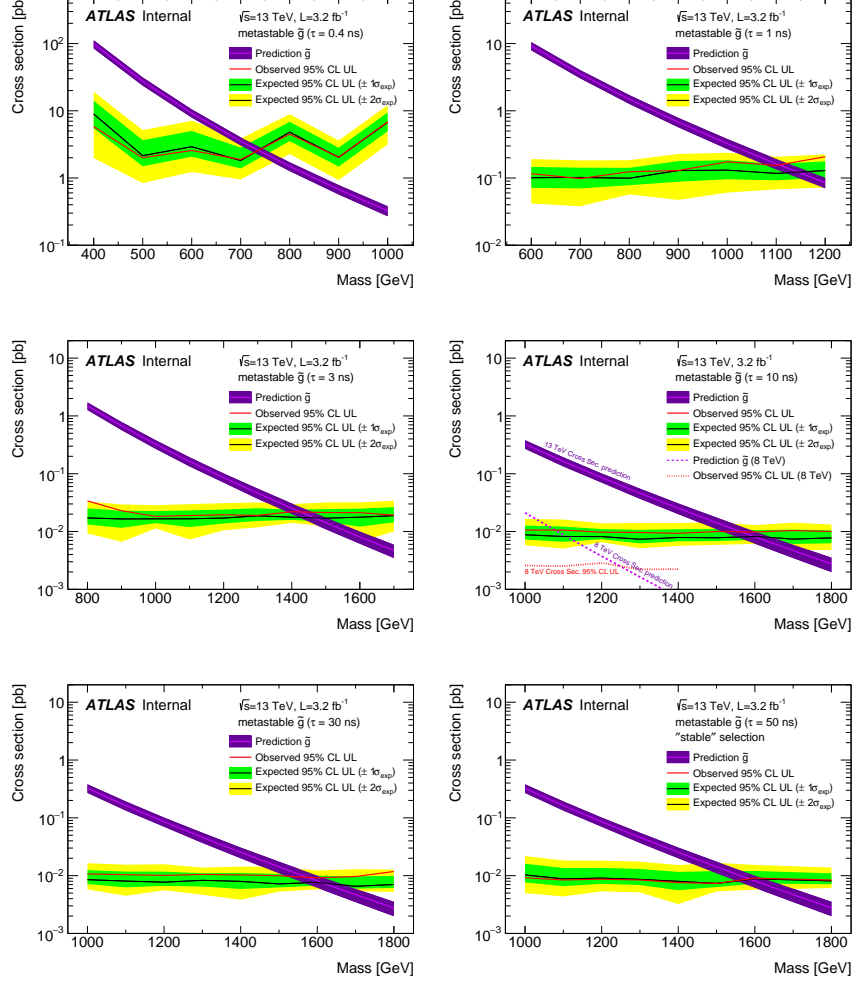


Figure 88: The observed and expected cross section limits as a function of mass for each generated lifetime. The predicted cross section values for the corresponding signals are included.

sections. These mass limits range from only 740 GeV at the lowest lifetimes considered, where the selection efficiency is very low, to up to 1580 GeV at 30 ns where the selection efficiency is maximized. The observed and expected mass limits for each lifetime point are detailed in Table 18, which also lists which selection region was used for each lifetime. These excluded range of masses as a function of lifetime is also shown in Figure 89. The Run 1 limits are included for comparison; the limits have increased by about 200 GeV on average. The search has also improved since the previous incarnation from Run 1 in optimizing the region between 30 GeV and detector-stable lifetimes by introducing the second signal region. The definition of the stable region prevents the significant drop in mass limit that occurred above 30 GeV in the Run 1 analysis.

Selection	τ [ns]	$M_{\text{obs}} > [\text{GeV}]$	$M_{\text{exp}} > [\text{GeV}]$
Metastable	0.4	740	730
"	1.0	1110	1150
"	3.0	1430	1470
"	10	1570	1600
"	30	1580	1620
Stable	50	1590	1590
"	stable	1570	1580

Table 18: The observed and expected 95% CL lower limit on mass for gluino R-Hadrons for each considered lifetime.

13.5 CONTEXT FOR LONG-LIVED SEARCHES

This search plays an important role in the current, combined [ATLAS](#) search for long lived particles. The mass limits provided by various [ATLAS](#) searches for long-lived gluino R-Hadrons can be seen in Figure 90. This search provides the most competitive limit for lifetimes between 3 ns up through very long lifetimes, where it is still competitive with dedicated searches for stable particles. The limits placed on gluino production are very similar to the limits on promptly decaying models.

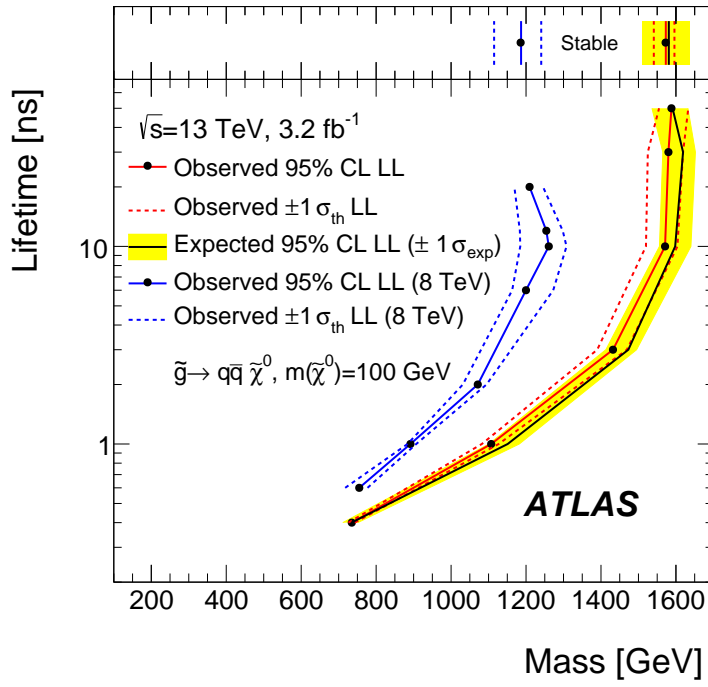


Figure 89: The excluded range of masses as a function of gluino lifetime. The expected lower limit (LL), with its experimental $\pm 1\sigma$ band, is given with respect to the nominal theoretical cross-section. The observed 95% LL obtained at $\sqrt{s} = 8 \text{ TeV}$ [70] is also shown for comparison.

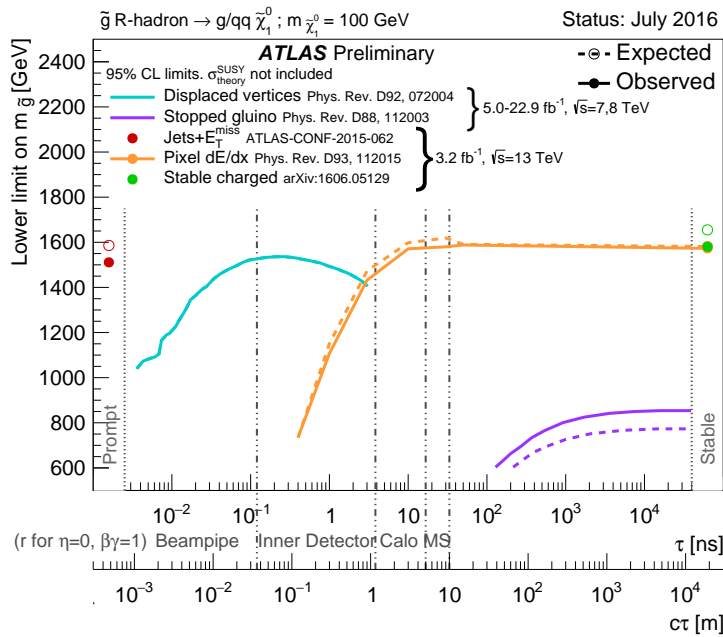


Figure 90: The constraints on the gluino mass as a function of lifetime for a split-supersymmetry model with the gluino R-Hadrons decaying into a gluon or light quarks and a neutralino with mass of 100 GeV. The solid lines indicate the observed limits, while the dashed lines indicate the expected limits. The area below the curves is excluded. The dots represent results for which the particle is assumed to be prompt or stable.

3615

PART VI

3616

CONCLUSIONS

3617

You can put some informational part preamble text here.

14

3618

3619 SUMMARY AND OUTLOOK

3620 14.1 SUMMARY

3621 14.2 OUTLOOK

3622

PART VII

3623

APPENDIX

3624

A

3625

3626 INELASTIC CROSS SECTION

B

3627

3628 EXPANDED R-HADRON YIELDS AND LIMITS

$m(\tilde{g})$ [GeV]	Left Extremum [GeV]	Right Extremum [GeV]
1000	682	1387
1100	763	1478
1200	801	1606
1300	809	1841
1400	861	2011
1500	920	2032
1600	952	2173
1800	1017	2422

Table 19: The left and right extremum of the mass window for each generated mass point with a 50 ns lifetime.

$m(\tilde{g})$ [GeV]	Left Extremum [GeV]	Right Extremum [GeV]
1000	689	1321
1100	746	1513
1200	788	1670
1300	860	1734
1400	833	1925
1500	852	2048
1600	833	2283
1700	946	2379
1800	869	2505

Table 20: The left and right extremum of the mass window for each generated mass point with a 30 ns lifetime.

$m(\tilde{g})$ [GeV]	Left Extremum [GeV]	Right Extremum [GeV]
1000	655	1349
1100	734	1455
1200	712	1631
1300	792	1737
1400	717	1926
1500	815	2117
1600	824	2122
1700	900	2274
1800	919	2344

Table 21: The left and right extremum of the mass window for each generated mass point with a 10 ns lifetime.

$m(\tilde{g})$ [GeV]	Left Extremum [GeV]	Right Extremum [GeV]
800	531	1065
900	576	1165
1000	610	1345
1100	635	1432
1200	663	1563
1300	620	1667
1400	742	1727
1500	761	1937
1600	573	2000
1700	621	2182

Table 22: The left and right extremum of the mass window used for each generated mass point with a lifetime of 3 ns.

$m(\tilde{g})$ [GeV]	Left Extremum [GeV]	Right Extremum [GeV]
600	411	758
700	385	876
800	486	970
900	406	987
1000	408	1136
1100	555	1196
1200	516	1378

Table 23: The left and right extremum of the mass window used for each mass point with a lifetime of 1 ns.

$m(\tilde{g})$ [GeV]	Left Extremum [GeV]	Right Extremum [GeV]
400	204	510
500	295	639
600	288	702
700	323	701
800	190	771
900	277	677
1000	249	688

Table 24: The left and right extremum of the mass window for each generated mass point with a lifetime of 0.4 ns.

$m(\tilde{g})$ [GeV]	Left Extremum [GeV]	Right Extremum [GeV]
800	627	1053
1000	726	1277
1200	857	1584
1400	924	1937
1600	993	2308
1800	1004	2554

Table 25: The left and right extremum of the mass window used for each generated stable mass point.

$m(\tilde{g})$ [GeV]	Expected Signal	Expected Background	Observed Data
1000	131.18 ± 6.35	1.803 ± 0.081	1.0 ± 1.0
1100	71.11 ± 3.35	1.409 ± 0.069	1.0 ± 1.0
1200	37.18 ± 1.75	1.310 ± 0.066	1.0 ± 1.0
1300	20.76 ± 0.95	1.431 ± 0.069	1.0 ± 1.0
1400	12.63 ± 0.57	1.273 ± 0.065	1.0 ± 1.0
1500	6.57 ± 0.29	1.115 ± 0.059	1.0 ± 1.0
1600	3.56 ± 0.16	1.041 ± 0.057	1.0 ± 1.0
1800	1.27 ± 0.05	0.918 ± 0.053	1.0 ± 1.0

Table 26: The expected number of signal events, the expected number of background events, and the observed number of events in data with their respective statistical errors within the respective mass window for each generated mass point with a lifetime of 50 ns.

$m(\tilde{g})$ [GeV]	Expected Signal	Expected Background	Observed Data
1000	144.65 ± 6.34	1.328 ± 0.063	2.0 ± 1.4
1100	75.28 ± 3.27	1.255 ± 0.060	2.0 ± 1.4
1200	40.51 ± 1.75	1.193 ± 0.058	2.0 ± 1.4
1300	20.91 ± 0.93	0.997 ± 0.051	2.0 ± 1.4
1400	11.97 ± 0.51	1.131 ± 0.056	2.0 ± 1.4
1500	6.81 ± 0.28	1.111 ± 0.055	2.0 ± 1.4
1600	4.19 ± 0.16	1.193 ± 0.058	2.0 ± 1.4
1700	2.42 ± 0.09	0.963 ± 0.050	2.0 ± 1.4
1800	1.46 ± 0.05	1.138 ± 0.056	3.0 ± 1.7

Table 27: The expected number of signal events, the expected number of background events, and the observed number of events in data with their respective statistical errors within the respective mass window for each generated mass point with a lifetime of 30 ns.

$m(\tilde{g})$ [GeV]	Expected Signal	Expected Background	Observed Data
1000	144.48 ± 5.14	1.499 ± 0.069	2.0 ± 1.4
1100	73.19 ± 2.61	1.260 ± 0.060	2.0 ± 1.4
1200	41.54 ± 1.41	1.456 ± 0.067	2.0 ± 1.4
1300	22.58 ± 0.77	1.201 ± 0.058	2.0 ± 1.4
1400	12.70 ± 0.42	1.558 ± 0.071	2.0 ± 1.4
1500	6.73 ± 0.24	1.237 ± 0.060	2.0 ± 1.4
1600	3.90 ± 0.13	1.201 ± 0.058	2.0 ± 1.4
1700	2.27 ± 0.07	1.027 ± 0.052	2.0 ± 1.4
1800	1.34 ± 0.04	1.019 ± 0.052	2.0 ± 1.4

Table 28: The expected number of signal events, the expected number of background events, and the observed number of events in data with their respective statistical errors within the respective mass window for each generated mass point with a lifetime of 10 ns.

$m(\tilde{g})$ [GeV]	Expected Signal	Expected Background	Observed Data
800	362.97 ± 14.68	1.841 ± 0.080	5.0 ± 2.2
900	169.20 ± 6.69	1.710 ± 0.076	3.0 ± 1.7
1000	84.78 ± 3.23	1.727 ± 0.076	2.0 ± 1.4
1100	40.06 ± 1.60	1.679 ± 0.075	2.0 ± 1.4
1200	20.06 ± 0.81	1.598 ± 0.072	2.0 ± 1.4
1300	10.76 ± 0.43	1.851 ± 0.080	2.0 ± 1.4
1400	5.52 ± 0.22	1.374 ± 0.064	2.0 ± 1.4
1500	3.16 ± 0.13	1.355 ± 0.064	2.0 ± 1.4
1600	2.13 ± 0.11	2.235 ± 0.093	3.0 ± 1.7
1700	1.10 ± 0.06	1.995 ± 0.085	2.0 ± 1.4

Table 29: The expected number of signal events, the expected number of background events, and the observed number of events in data with their respective statistical errors within the respective mass window for each generated mass point with a lifetime of 3 ns.

$m(\tilde{g})$ [GeV]	Expected Signal	Expected Background	Observed Data
600	431.80 ± 36.60	2.418 ± 0.099	3.0 ± 1.7
700	192.77 ± 15.28	3.267 ± 0.126	3.0 ± 1.7
800	69.63 ± 5.90	2.125 ± 0.089	3.0 ± 1.7
900	28.91 ± 2.59	3.114 ± 0.121	3.0 ± 1.7
1000	13.64 ± 1.22	3.359 ± 0.129	5.0 ± 2.2
1100	6.13 ± 0.57	1.879 ± 0.081	3.0 ± 1.7
1200	3.24 ± 0.30	2.387 ± 0.098	5.0 ± 2.2

Table 30: The expected number of signal events, the expected number of background events, and the observed number of events in data with their respective statistical errors within the respective mass window for each generated mass point with a lifetime of 1 ns.

$m(\tilde{g})$ [GeV]	Expected Signal	Expected Background	Observed Data
400	181.71 ± 75.59	6.780 ± 0.238	4.0 ± 2.0
500	103.88 ± 30.05	4.310 ± 0.160	4.0 ± 2.0
600	28.34 ± 9.34	4.868 ± 0.177	4.0 ± 2.0
700	13.62 ± 4.00	3.908 ± 0.147	4.0 ± 2.0
800	2.75 ± 1.15	9.001 ± 0.308	8.0 ± 2.8
900	2.25 ± 0.71	5.045 ± 0.183	5.0 ± 2.2
1000	0.34 ± 0.19	6.026 ± 0.214	6.0 ± 2.4

Table 31: The expected number of signal events, the expected number of background events, and the observed number of events in data with their respective statistical errors within the respective mass window for each generated mass point with a lifetime of p4 ns.

$m(\tilde{g})$ [GeV]	Expected Signal	Expected Background	Observed Data
800	462.83 ± 14.86	1.764 ± 0.080	2.0 ± 1.4
1000	108.73 ± 3.38	1.458 ± 0.070	1.0 ± 1.0
1200	31.74 ± 0.95	1.137 ± 0.060	1.0 ± 1.0
1400	10.22 ± 0.29	1.058 ± 0.058	1.0 ± 1.0
1600	3.07 ± 0.09	0.947 ± 0.054	1.0 ± 1.0
1800	1.08 ± 0.05	0.940 ± 0.054	1.0 ± 1.0

Table 32: The expected number of signal events, the expected number of background events, and the observed number of events in data with their respective statistical errors within the respective mass window for each generated stable mass point

- 3630 [1] A. D. Martin, W. J. Stirling, R. S. Thorne, and G. Watt. “Parton distributions
3631 for the LHC”. In: *Eur. Phys. J.* C63 (2009), pp. 189–285. doi: [10.1140/epjc/s10052-009-1072-5](https://doi.org/10.1140/epjc/s10052-009-1072-5). arXiv: [0901.0002 \[hep-ph\]](https://arxiv.org/abs/0901.0002).
- 3633 [2] Prajwal Raj Kafle, Sanjib Sharma, Geraint F. Lewis, and Joss Bland-Hawthorn.
3634 “On the Shoulders of Giants: Properties of the Stellar Halo and the Milky
3635 Way Mass Distribution”. In: *Astrophys. J.* 794.1 (2014), p. 59. doi: [10.1088/0004-637X/794/1/59](https://doi.org/10.1088/0004-637X/794/1/59). arXiv: [1408.1787 \[astro-ph.GA\]](https://arxiv.org/abs/1408.1787).
- 3637 [3] Lyndon Evans and Philip Bryant. “LHC Machine”. In: *JINST* 3 (2008), S08001.
3638 doi: [10.1088/1748-0221/3/08/S08001](https://doi.org/10.1088/1748-0221/3/08/S08001).
- 3639 [4] C Lefevre. “LHC: the guide (English version). Guide du LHC (version anglaise)”.
3640 2009. URL: <https://cds.cern.ch/record/1165534>.
- 3641 [5] ATLAS Collaboration. “The ATLAS Experiment at the CERN Large Hadron
3642 Collider”. In: *JINST* 3 (2008), S08003. doi: [10.1088/1748-0221/3/08/S08003](https://doi.org/10.1088/1748-0221/3/08/S08003).
- 3644 [6] S. Chatrchyan et al. “The CMS experiment at the CERN LHC”. In: *JINST*
3645 3 (2008), S08004. doi: [10.1088/1748-0221/3/08/S08004](https://doi.org/10.1088/1748-0221/3/08/S08004).
- 3646 [7] A. Augusto Alves Jr. et al. “The LHCb Detector at the LHC”. In: *JINST* 3
3647 (2008), S08005. doi: [10.1088/1748-0221/3/08/S08005](https://doi.org/10.1088/1748-0221/3/08/S08005).
- 3648 [8] K. Aamodt et al. “The ALICE experiment at the CERN LHC”. In: *JINST* 3
3649 (2008), S08002. doi: [10.1088/1748-0221/3/08/S08002](https://doi.org/10.1088/1748-0221/3/08/S08002).
- 3650 [9] K. A. Olive et al. “Review of Particle Physics”. In: *Chin. Phys. C38* (2014),
3651 p. 090001. doi: [10.1088/1674-1137/38/9/090001](https://doi.org/10.1088/1674-1137/38/9/090001).
- 3652 [10] Daniel Froidevaux and Paris Sphicas. “General-Purpose Detectors for the
3653 Large Hadron Collider”. In: *Annual Review of Nuclear and Particle Science*
3654 56.1 (2006), pp. 375–440. doi: [10.1146/annurev.nucl.54.070103.181209](https://doi.org/10.1146/annurev.nucl.54.070103.181209). URL: <http://dx.doi.org/10.1146/annurev.nucl.54.070103.181209>.
- 3657 [11] M Capeans, G Darbo, K Einsweiller, M Elsing, T Flick, M Garcia-Sciveres,
3658 C Gemme, H Pernegger, O Rohne, and R Vuillermet. *ATLAS Insertable B-*
3659 *Layer Technical Design Report*. Tech. rep. CERN-LHCC-2010-013. ATLAS-
3660 TDR-19. 2010. URL: <https://cds.cern.ch/record/1291633>.
- 3661 [12] T. Cornelissen, M. Elsing, S. Fleischmann, W. Liebig, and E. Moyse. “Con-
3662 cepts, Design and Implementation of the ATLAS New Tracking (NEWT)”.
3663 In: (2007). Ed. by A. Salzburger.
- 3664 [13] “Performance of the ATLAS Inner Detector Track and Vertex Reconstruc-
3665 tion in the High Pile-Up LHC Environment”. In: (2012).

- 3666 [14] ATLAS Collaboration. “A neural network clustering algorithm for the AT-
 3667 LAS silicon pixel detector”. In: *JINST* 9 (2014), P09009. doi: [10.1088/1748-0221/9/09/P09009](https://doi.org/10.1088/1748-0221/9/09/P09009). arXiv: [1406.7690 \[hep-ex\]](https://arxiv.org/abs/1406.7690).
- 3669 [15] ATLAS Collaboration. “Electron reconstruction and identification efficiency
 3670 measurements with the ATLAS detector using the 2011 LHC proton–proton
 3671 collision data”. In: *Eur. Phys. J. C* 74 (2014), p. 2941. doi: [10.1140/epjc/s10052-014-2941-0](https://doi.org/10.1140/epjc/s10052-014-2941-0). arXiv: [1404.2240 \[hep-ex\]](https://arxiv.org/abs/1404.2240). PERF-2013-03.
- 3673 [16] Matteo Cacciari, Gavin P. Salam, and Gregory Soyez. “The anti- k_t jet clus-
 3674 tering algorithm”. In: *JHEP* 04 (2008), p. 063. doi: [10.1088/1126-6708/2008/04/063](https://doi.org/10.1088/1126-6708/2008/04/063). arXiv: [0802.1189 \[hep-ph\]](https://arxiv.org/abs/0802.1189).
- 3676 [17] S. Agostinelli et al. “GEANT4: A simulation toolkit”. In: *Nucl. Instrum. Meth.*
 3677 A 506 (2003), pp. 250–303. doi: [10.1016/S0168-9002\(03\)01368-8](https://doi.org/10.1016/S0168-9002(03)01368-8).
- 3678 [18] ATLAS Collaboration. “A study of the material in the ATLAS inner de-
 3679 tector using secondary hadronic interactions”. In: *JINST* 7 (2012), P01013.
 3680 doi: [10.1088/1748-0221/7/01/P01013](https://doi.org/10.1088/1748-0221/7/01/P01013). arXiv: [1110.6191 \[hep-ex\]](https://arxiv.org/abs/1110.6191).
 3681 PERF-2011-08.
- 3682 [19] ATLAS Collaboration. “Electron and photon energy calibration with the
 3683 ATLAS detector using LHC Run 1 data”. In: *Eur. Phys. J. C* 74 (2014), p. 3071.
 3684 doi: [10.1140/epjc/s10052-014-3071-4](https://doi.org/10.1140/epjc/s10052-014-3071-4). arXiv: [1407.5063 \[hep-ex\]](https://arxiv.org/abs/1407.5063). PERF-2013-05.
- 3686 [20] ATLAS Collaboration. “A measurement of the calorimeter response to sin-
 3687 gle hadrons and determination of the jet energy scale uncertainty using
 3688 LHC Run-1 pp -collision data with the ATLAS detector”. In: (2016). arXiv:
 3689 [1607.08842 \[hep-ex\]](https://arxiv.org/abs/1607.08842). PERF-2015-05.
- 3690 [21] ATLAS Collaboration. “Single hadron response measurement and calorime-
 3691 ter jet energy scale uncertainty with the ATLAS detector at the LHC”. In:
 3692 *Eur. Phys. J. C* 73 (2013), p. 2305. doi: [10.1140/epjc/s10052-013-2305-1](https://doi.org/10.1140/epjc/s10052-013-2305-1). arXiv: [1203.1302 \[hep-ex\]](https://arxiv.org/abs/1203.1302). PERF-2011-05.
- 3694 [22] ATLAS Collaboration. “The ATLAS Simulation Infrastructure”. In: *Eur.*
 3695 *Phys. J. C* 70 (2010), p. 823. doi: [10.1140/epjc/s10052-010-1429-9](https://doi.org/10.1140/epjc/s10052-010-1429-9).
 3696 arXiv: [1005.4568 \[hep-ex\]](https://arxiv.org/abs/1005.4568). SOFT-2010-01.
- 3697 [23] T. Sjöstrand, S. Mrenna, and P. Skands. “A Brief Introduction to PYTHIA
 3698 8.1”. In: *Comput. Phys. Commun.* 178 (2008), pp. 852–867. doi: [10.1016/j.cpc.2008.01.036](https://doi.org/10.1016/j.cpc.2008.01.036). arXiv: [0710.3820](https://arxiv.org/abs/0710.3820).
- 3700 [24] ATLAS Collaboration. *Summary of ATLAS Pythia 8 tunes*. ATL-PHYS-PUB-
 3701 2012-003. 2012. URL: <http://cds.cern.ch/record/1474107>.
- 3702 [25] A.D. Martin, W.J. Stirling, R.S. Thorne, and G. Watt. “Parton distributions
 3703 for the LHC”. In: *Eur. Phys. J. C* 63 (2009). Figures from the [MSTW Website](#),
 3704 pp. 189–285. doi: [10.1140/epjc/s10052-009-1072-5](https://doi.org/10.1140/epjc/s10052-009-1072-5). arXiv: [0901.0002](https://arxiv.org/abs/0901.0002).
- 3706 [26] A. Sherstnev and R.S. Thorne. “Parton Distributions for LO Generators”.
 3707 In: *Eur. Phys. J. C* 55 (2008), pp. 553–575. doi: [10.1140/epjc/s10052-008-0610-x](https://doi.org/10.1140/epjc/s10052-008-0610-x). arXiv: [0711.2473](https://arxiv.org/abs/0711.2473).

- 3709 [27] A. Ribon et al. *Status of Geant4 hadronic physics for the simulation of LHC*
 3710 *experiments at the start of LHC physics program.* CERN-LCGAPP-2010-02.
 3711 2010. URL: <http://lcgapp.cern.ch/project/docs/noteStatusHadronic2010.pdf>.
- 3712
- 3713 [28] M. P. Guthrie, R. G. Alsmiller, and H. W. Bertini. "Calculation of the cap-
 3714 ture of negative pions in light elements and comparison with experiments
 3715 pertaining to cancer radiotherapy". In: *Nucl. Instrum. Meth.* 66 (1968), pp. 29–
 3716 36. doi: [10.1016/0029-554X\(68\)90054-2](https://doi.org/10.1016/0029-554X(68)90054-2).
- 3717 [29] H. W. Bertini and P. Guthrie. "News item results from medium-energy
 3718 intranuclear-cascade calculation". In: *Nucl. Instr. and Meth. A* 169 (1971),
 3719 p. 670. doi: [10.1016/0375-9474\(71\)90710-X](https://doi.org/10.1016/0375-9474(71)90710-X).
- 3720 [30] V.A. Karmanov. "Light Front Wave Function of Relativistic Composite
 3721 System in Explicitly Solvable Model". In: *Nucl. Phys. B* 166 (1980), p. 378.
 3722 doi: [10.1016/0550-3213\(80\)90204-7](https://doi.org/10.1016/0550-3213(80)90204-7).
- 3723 [31] H. S. Fesefeldt. *GHEISHA program.* Pitha-85-02, Aachen. 1985.
- 3724 [32] G. Folger and J.P. Wellisch. "String parton models in Geant4". In: (2003).
 3725 arXiv: [nucl-th/0306007](https://arxiv.org/abs/hep-ph/0306007).
- 3726 [33] N. S. Amelin et al. "Transverse flow and collectivity in ultrarelativistic
 3727 heavy-ion collisions". In: *Phys. Rev. Lett.* 67 (1991), p. 1523. doi: [10.1103/PhysRevLett.67.1523](https://doi.org/10.1103/PhysRevLett.67.1523).
- 3729 [34] N. S. Amelin et al. "Collectivity in ultrarelativistic heavy ion collisions". In:
 3730 *Nucl. Phys. A* 544 (1992), p. 463. doi: [10.1016/0375-9474\(92\)90598-E](https://doi.org/10.1016/0375-9474(92)90598-E).
- 3732 [35] L. V. Bravina et al. "Fluid dynamics and Quark Gluon string model - What
 3733 we can expect for Au+Au collisions at 11.6 AGeV/c". In: *Nucl. Phys. A* 566
 3734 (1994), p. 461. doi: [10.1016/0375-9474\(94\)90669-6](https://doi.org/10.1016/0375-9474(94)90669-6).
- 3735 [36] L. V. Bravin et al. "Scaling violation of transverse flow in heavy ion colli-
 3736 sions at AGS energies". In: *Phys. Lett. B* 344 (1995), p. 49. doi: [10.1016/0370-2693\(94\)01560-Y](https://doi.org/10.1016/0370-2693(94)01560-Y).
- 3738 [37] B. Andersson et al. "A model for low-pT hadronic reactions with general-
 3739 izations to hadron-nucleus and nucleus-nucleus collisions". In: *Nucl. Phys.*
 3740 *B* 281 (1987), p. 289. doi: [10.1016/0550-3213\(87\)90257-4](https://doi.org/10.1016/0550-3213(87)90257-4).
- 3741 [38] B. Andersson, A. Tai, and B.-H. Sa. "Final state interactions in the (nuclear)
 3742 FRITIOF string interaction scenario". In: *Z. Phys. C* 70 (1996), pp. 499–
 3743 506. doi: [10.1007/s002880050127](https://doi.org/10.1007/s002880050127).
- 3744 [39] B. Nilsson-Almqvist and E. Stenlund. "Interactions Between Hadrons and
 3745 Nuclei: The Lund Monte Carlo, Fritiof Version 1.6". In: *Comput. Phys. Com-*
 3746 *mun.* 43 (1987), p. 387. doi: [10.1016/0010-4655\(87\)90056-7](https://doi.org/10.1016/0010-4655(87)90056-7).
- 3747 [40] B. Ganhuyag and V. Uzhinsky. "Modified FRITIOF code: Negative charged
 3748 particle production in high energy nucleus nucleus interactions". In: *Czech.*
 3749 *J. Phys.* 47 (1997), pp. 913–918. doi: [10.1023/A:1021296114786](https://doi.org/10.1023/A:1021296114786).

- 3750 [41] ATLAS Collaboration. “Topological cell clustering in the ATLAS calorimeters and its performance in LHC Run 1”. In: (2016). arXiv: [1603.02934](https://arxiv.org/abs/1603.02934) [hep-ex].
- 3751
3752
3753 [42] Peter Speckmayer. “Energy Measurement of Hadrons with the CERN ATLAS Calorimeter”. Presented on 18 Jun 2008. PhD thesis. Vienna: Vienna, Tech. U., 2008. URL: <http://cds.cern.ch/record/1112036>.
- 3754
3755
3756 [43] CMS Collaboration. “The CMS barrel calorimeter response to particle beams from 2 to 350 GeV/c”. In: *Eur. Phys. J. C* 60.3 (2009). doi: [10.1140/epjc/s10052-009-0959-5](https://doi.org/10.1140/epjc/s10052-009-0959-5).
- 3757
3758
3759 [44] J. Beringer et al. (Particle Data Group). “Review of Particle Physics”. In: *Chin. Phys. C* 38 (2014), p. 090001. URL: <http://pdg.lbl.gov>.
- 3760
3761 [45] P. Adragna et al. “Measurement of Pion and Proton Response and Longitudinal Shower Profiles up to 20 Nuclear Interaction Lengths with the ATLAS Tile Calorimeter”. In: *Nucl. Instrum. Meth. A* 615 (2010), pp. 158–181. doi: [10.1016/j.nima.2010.01.037](https://doi.org/10.1016/j.nima.2010.01.037).
- 3762
3763
3764 [46] ATLAS Collaboration. “Jet energy measurement and its systematic uncertainty in proton–proton collisions at $\sqrt{s} = 7$ TeV with the ATLAS detector”. In: *Eur. Phys. J. C* 75 (2015), p. 17. doi: [10.1140/epjc/s10052-014-3190-y](https://doi.org/10.1140/epjc/s10052-014-3190-y). arXiv: [1406.0076](https://arxiv.org/abs/1406.0076) [hep-ex]. PERF-2012-01.
- 3765
3766
3767
3768 [47] Hung-Liang Lai, Marco Guzzi, Joey Huston, Zhao Li, Pavel M. Nadolsky, et al. “New parton distributions for collider physics”. In: *Phys. Rev. D* 82 (2010), p. 074024. doi: [10.1103/PhysRevD.82.074024](https://doi.org/10.1103/PhysRevD.82.074024). arXiv: [1007.2241](https://arxiv.org/abs/1007.2241) [hep-ph].
- 3769
3770
3771
3772 [48] E. Abat et al. “Study of energy response and resolution of the ATLAS barrel calorimeter to hadrons of energies from 20 to 350 GeV”. In: *Nucl. Instrum. Meth. A* 621.1-3 (2010), pp. 134 – 150. doi: <http://dx.doi.org/10.1016/j.nima.2010.04.054>.
- 3773
3774
3775
3776 [49] ATLAS Collaboration. “Jet energy measurement with the ATLAS detector in proton–proton collisions at $\sqrt{s} = 7$ TeV”. In: *Eur. Phys. J. C* 73 (2013), p. 2304. doi: [10.1140/epjc/s10052-013-2304-2](https://doi.org/10.1140/epjc/s10052-013-2304-2). arXiv: [1112.6426](https://arxiv.org/abs/1112.6426) [hep-ex]. PERF-2011-03.
- 3777
3778
3779
3780 [50] Nausheen R. Shah and Carlos E. M. Wagner. “Gravitons and dark matter in universal extra dimensions”. In: *Phys. Rev. D* 74 (2006), p. 104008. doi: [10.1103/PhysRevD.74.104008](https://doi.org/10.1103/PhysRevD.74.104008). arXiv: [hep-ph/0608140](https://arxiv.org/abs/hep-ph/0608140) [hep-ph].
- 3781
3782
3783
3784 [51] Jonathan L. Feng, Arvind Rajaraman, and Fumihiro Takayama. “Graviton cosmology in universal extra dimensions”. In: *Phys. Rev. D* 68 (2003), p. 085018. doi: [10.1103/PhysRevD.68.085018](https://doi.org/10.1103/PhysRevD.68.085018). arXiv: [hep-ph/0307375](https://arxiv.org/abs/hep-ph/0307375) [hep-ph].
- 3785
3786
3787
3788 [52] Paul H. Frampton and Pham Quang Hung. “Long-lived quarks?” In: *Phys. Rev. D* 58 (5 1998), p. 057704. doi: [10.1103/PhysRevD.58.057704](https://doi.org/10.1103/PhysRevD.58.057704). URL: <http://link.aps.org/doi/10.1103/PhysRevD.58.057704>.
- 3789
3790
3791

- 3792 [53] C. Friberg, E. Norrbin, and T. Sjostrand. “QCD aspects of leptoquark pro-
 3793 duction at HERA”. In: *Phys. Lett.* B403 (1997), pp. 329–334. doi: [10.1016/S0370-2693\(97\)00543-1](https://doi.org/10.1016/S0370-2693(97)00543-1). arXiv: [hep-ph/9704214](https://arxiv.org/abs/hep-ph/9704214) [hep-ph].
- 3795 [54] Herbert K. Dreiner. “An introduction to explicit R-parity violation”. In:
 3796 (1997). arXiv: [hep-ph/9707435](https://arxiv.org/abs/hep-ph/9707435).
- 3797 [55] Edmond L. Berger and Zack Sullivan. “Lower limits on R-parity-violating
 3798 couplings in supersymmetry”. In: *Phys. Rev. Lett.* 92 (2004), p. 201801. doi:
 3799 [10.1103/PhysRevLett.92.201801](https://doi.org/10.1103/PhysRevLett.92.201801). arXiv: [hep-ph/0310001](https://arxiv.org/abs/hep-ph/0310001).
- 3800 [56] R. Barbieri, C. Berat, M. Besancon, M. Chemtob, A. Deandrea, et al. “R-
 3801 parity violating supersymmetry”. In: *Phys. Rept.* 420 (2005), p. 1. doi: [10.1016/j.physrep.2005.08.006](https://doi.org/10.1016/j.physrep.2005.08.006). arXiv: [hep-ph/0406039](https://arxiv.org/abs/hep-ph/0406039).
- 3803 [57] M. Fairbairn et al. “Stable massive particles at colliders”. In: *Phys. Rept.* 438
 3804 (2007), p. 1. doi: [10.1016/j.physrep.2006.10.002](https://doi.org/10.1016/j.physrep.2006.10.002). arXiv: [hep-ph/0611040](https://arxiv.org/abs/hep-ph/0611040).
- 3806 [58] Christopher F. Kolda. “Gauge-mediated supersymmetry breaking: Intro-
 3807 duction, review and update”. In: *Nucl. Phys. Proc. Suppl.* 62 (1998), p. 266.
 3808 doi: [10.1016/S0920-5632\(97\)00667-1](https://doi.org/10.1016/S0920-5632(97)00667-1). arXiv: [hep-ph/9707450](https://arxiv.org/abs/hep-ph/9707450).
- 3809 [59] Howard Baer, Kingman Cheung, and John F. Gunion. “A Heavy gluino as
 3810 the lightest supersymmetric particle”. In: *Phys. Rev. D* 59 (1999), p. 075002.
 3811 doi: [10.1103/PhysRevD.59.075002](https://doi.org/10.1103/PhysRevD.59.075002). arXiv: [hep-ph/9806361](https://arxiv.org/abs/hep-ph/9806361).
- 3812 [60] S. James Gates Jr. and Oleg Lebedev. “Searching for supersymmetry in
 3813 hadrons”. In: *Phys. Lett. B* 477 (2000), p. 216. doi: [10.1016/S0370-2693\(00\)00172-6](https://doi.org/10.1016/S0370-2693(00)00172-6). arXiv: [hep-ph/9912362](https://arxiv.org/abs/hep-ph/9912362).
- 3815 [61] G. F. Giudice and A. Romanino. “Split supersymmetry”. In: *Nucl. Phys. B*
 3816 699 (2004), p. 65. doi: [10.1016/j.nuclphysb.2004.11.048](https://doi.org/10.1016/j.nuclphysb.2004.11.048). arXiv:
 3817 [hep-ph/0406088](https://arxiv.org/abs/hep-ph/0406088).
- 3818 [62] N. Arkani-Hamed, S. Dimopoulos, G. F. Giudice, and A. Romanino. “As-
 3819 pects of split supersymmetry”. In: *Nucl. Phys. B* 709 (2005), p. 3. doi: [10.1016/j.nuclphysb.2004.12.026](https://doi.org/10.1016/j.nuclphysb.2004.12.026). arXiv: [hep-ph/0409232](https://arxiv.org/abs/hep-ph/0409232).
- 3821 [63] Glennys R. Farrar and Pierre Fayet. “Phenomenology of the Production,
 3822 Decay, and Detection of New Hadronic States Associated with Supersym-
 3823 metry”. In: *Phys. Lett.* B76 (1978), pp. 575–579. doi: [10.1016/0370-2693\(78\)90858-4](https://doi.org/10.1016/0370-2693(78)90858-4).
- 3825 [64] A. C. Kraan, J. B. Hansen, and P. Nevski. “Discovery potential of R-hadrons
 3826 with the ATLAS detector”. In: *Eur. Phys. J.* C49 (2007), pp. 623–640. doi:
 3827 [10.1140/epjc/s10052-006-0162-x](https://doi.org/10.1140/epjc/s10052-006-0162-x). arXiv: [hep-ex/0511014](https://arxiv.org/abs/hep-ex/0511014)
 3828 [hep-ex].
- 3829 [65] Rasmus Mackeprang and David Milstead. “An Updated Description of
 3830 Heavy-Hadron Interactions in GEANT-4”. In: *Eur. Phys. J.* C66 (2010), pp. 493–
 3831 501. doi: [10.1140/epjc/s10052-010-1262-1](https://doi.org/10.1140/epjc/s10052-010-1262-1). arXiv: [0908.1868](https://arxiv.org/abs/0908.1868)
 3832 [hep-ph].

- 3833 [66] ATLAS Collaboration. “Search for massive, long-lived particles using mul-
 3834 titrack displaced vertices or displaced lepton pairs in pp collisions at $\sqrt{s} =$
 3835 8 TeV with the ATLAS detector”. In: *Phys. Rev. D* 92 (2015), p. 072004.
 3836 doi: [10.1103/PhysRevD.92.072004](https://doi.org/10.1103/PhysRevD.92.072004). arXiv: [1504.05162 \[hep-ex\]](https://arxiv.org/abs/1504.05162).
 3837 SUSY-2014-02.
- 3838 [67] ATLAS Collaboration. “Search for charginos nearly mass degenerate with
 3839 the lightest neutralino based on a disappearing-track signature in pp col-
 3840 lisions at $\sqrt{s} = 8$ TeV with the ATLAS detector”. In: *Phys. Rev. D* 88 (2013),
 3841 p. 112006. doi: [10.1103/PhysRevD.88.112006](https://doi.org/10.1103/PhysRevD.88.112006). arXiv: [1310.3675](https://arxiv.org/abs/1310.3675)
 3842 [hep-ex]. SUSY-2013-01.
- 3843 [68] ATLAS Collaboration. “Searches for heavy long-lived sleptons and R-Hadrons
 3844 with the ATLAS detector in pp collisions at $\sqrt{s} = 7$ TeV”. In: *Phys. Lett. B*
 3845 720 (2013), p. 277. doi: [10.1016/j.physletb.2013.02.015](https://doi.org/10.1016/j.physletb.2013.02.015). arXiv:
 3846 [1211.1597 \[hep-ex\]](https://arxiv.org/abs/1211.1597). SUSY-2012-01.
- 3847 [69] ATLAS Collaboration. “Searches for heavy long-lived charged particles
 3848 with the ATLAS detector in proton–proton collisions at $\sqrt{s} = 8$ TeV”. In:
 3849 *JHEP* 01 (2015), p. 068. doi: [10.1007/JHEP01\(2015\)068](https://doi.org/10.1007/JHEP01(2015)068). arXiv:
 3850 [1411.6795 \[hep-ex\]](https://arxiv.org/abs/1411.6795). SUSY-2013-22.
- 3851 [70] ATLAS Collaboration. “Search for metastable heavy charged particles with
 3852 large ionisation energy loss in pp collisions at $\sqrt{s} = 8$ TeV using the AT-
 3853 LAS experiment”. In: *Eur. Phys. J. C* 75 (2015), p. 407. doi: [10.1140/epjc/s10052-015-3609-0](https://doi.org/10.1140/epjc/s10052-015-3609-0). arXiv: [1506.05332 \[hep-ex\]](https://arxiv.org/abs/1506.05332). SUSY-
 3854 2014-09.
- 3855 [71] ATLAS Collaboration. “Search for heavy long-lived charged R -hadrons
 3856 with the ATLAS detector in 3.2 fb^{-1} of proton–proton collision data at
 3857 $\sqrt{s} = 13$ TeV”. In: *Phys. Lett. B* 760 (2016), pp. 647–665. doi: [10.1016/j.physletb.2016.07.042](https://doi.org/10.1016/j.physletb.2016.07.042). arXiv: [1606.05129 \[hep-ex\]](https://arxiv.org/abs/1606.05129).
- 3860 [72] Torbjorn Sjöstrand, Stephen Mrenna, and Peter Skands. “PYTHIA 6.4 Physics
 3861 and Manual”. In: *JHEP* 0605 (2006), p. 026. doi: [10.1088/1126-6708/2006/05/026](https://doi.org/10.1088/1126-6708/2006/05/026). arXiv: [hep-ph/0603175](https://arxiv.org/abs/hep-ph/0603175).
- 3863 [73] *Further ATLAS tunes of PYTHIA6 and Pythia 8*. Tech. rep. ATL-PHYS-PUB-
 3864 2011-014. Geneva: CERN, 2011. url: <https://cds.cern.ch/record/1400677>.
- 3866 [74] Aafke Christine Kraan. “Interactions of heavy stable hadronizing parti-
 3867 cles”. In: *Eur. Phys. J. C* 37 (2004), pp. 91–104. doi: [10.1140/epjc/s2004-01946-6](https://doi.org/10.1140/epjc/s2004-01946-6). arXiv: [hep-ex/0404001 \[hep-ex\]](https://arxiv.org/abs/hep-ex/0404001).
- 3869 [75] M. Fairbairn et al. “Stable massive particles at colliders”. In: *Phys. Rept.* 438
 3870 (2007), p. 1. doi: [10.1016/j.physrep.2006.10.002](https://doi.org/10.1016/j.physrep.2006.10.002). arXiv: [hep-ph/0611040](https://arxiv.org/abs/hep-ph/0611040).
- 3872 [76] W. Beenakker, R. Hopker, M. Spira, and P. M. Zerwas. “Squark and gluino
 3873 production at hadron colliders”. In: *Nucl. Phys. B* 492 (1997), p. 51. doi:
 3874 [10.1016/S0550-3213\(97\)00084-9](https://doi.org/10.1016/S0550-3213(97)00084-9). arXiv: [hep-ph/9610490](https://arxiv.org/abs/hep-ph/9610490).

- 3875 [77] A. Kulesza and L. Motyka. "Threshold resummation for squark-antisquark
 3876 and gluino-pair production at the LHC". In: *Phys. Rev. Lett.* 102 (2009),
 3877 p. 111802. doi: [10.1103/PhysRevLett.102.111802](https://doi.org/10.1103/PhysRevLett.102.111802). arXiv: [0807.2405 \[hep-ph\]](https://arxiv.org/abs/0807.2405).
- 3879 [78] A. Kulesza and L. Motyka. "Soft gluon resummation for the production
 3880 of gluino-gluino and squark-antisquark pairs at the LHC". In: *Phys. Rev.*
 3881 *D* 80 (2009), p. 095004. doi: [10.1103/PhysRevD.80.095004](https://doi.org/10.1103/PhysRevD.80.095004). arXiv:
 3882 [0905.4749 \[hep-ph\]](https://arxiv.org/abs/0905.4749).
- 3883 [79] Wim Beenakker, Silja Brensing, Michael Kramer, Anna Kulesza, Eric Lae-
 3884 nen, et al. "Soft-gluon resummation for squark and gluino hadroproduc-
 3885 tion". In: *JHEP* 0912 (2009), p. 041. doi: [10.1088/1126-6708/2009/12/041](https://doi.org/10.1088/1126-6708/2009/12/041). arXiv: [0909.4418 \[hep-ph\]](https://arxiv.org/abs/0909.4418).
- 3887 [80] W. Beenakker, S. Brensing, M.n Kramer, A. Kulesza, E. Laenen, et al. "Squark
 3888 and Gluino Hadroproduction". In: *Int. J. Mod. Phys. A* 26 (2011), p. 2637.
 3889 doi: [10.1142/S0217751X11053560](https://doi.org/10.1142/S0217751X11053560). arXiv: [1105.1110 \[hep-ph\]](https://arxiv.org/abs/1105.1110).
- 3890 [81] Michael Krämer et al. *Supersymmetry production cross sections in pp collisions*
 3891 at $\sqrt{s} = 7$ TeV. 2012. arXiv: [1206.2892 \[hep-ph\]](https://arxiv.org/abs/1206.2892).
- 3892 [82] Rasmus Mackeprang and Andrea Rizzi. "Interactions of Coloured Heavy
 3893 Stable Particles in Matter". In: *Eur. Phys. J.* C50 (2007), pp. 353–362. doi:
 3894 [10.1140/epjc/s10052-007-0252-4](https://doi.org/10.1140/epjc/s10052-007-0252-4). arXiv: [hep-ph/0612161](https://arxiv.org/abs/hep-ph/0612161)
 3895 [hep-ph].
- 3896 [83] Rasmus Mackeprang and David Milstead. "An Updated Description of
 3897 Heavy-Hadron Interactions in GEANT-4". In: *Eur. Phys. J.* C66 (2010), pp. 493–
 3898 501. doi: [10.1140/epjc/s10052-010-1262-1](https://doi.org/10.1140/epjc/s10052-010-1262-1). arXiv: [0908.1868](https://arxiv.org/abs/0908.1868)
 3899 [hep-ph].
- 3900 [84] J. Alwall, R. Frederix, S. Frixione, V. Hirschi, F. Maltoni, O. Mattelaer, H. S.
 3901 Shao, T. Stelzer, P. Torrielli, and M. Zaro. "The automated computation of
 3902 tree-level and next-to-leading order differential cross sections, and their
 3903 matching to parton shower simulations". In: *JHEP* 07 (2014), p. 079. doi:
 3904 [10.1007/JHEP07\(2014\)079](https://doi.org/10.1007/JHEP07(2014)079). arXiv: [1405.0301 \[hep-ph\]](https://arxiv.org/abs/1405.0301).
- 3905 [85] "dE/dx measurement in the ATLAS Pixel Detector and its use for particle
 3906 identification". In: (2011).
- 3907 [86] ATLAS Collaboration. "The ATLAS Simulation Infrastructure". In: *Eur.*
 3908 *Phys. J.* C70 (2010), pp. 823–874. doi: [10.1140/epjc/s10052-010-1429-9](https://doi.org/10.1140/epjc/s10052-010-1429-9). arXiv: [1005.4568 \[physics.ins-det\]](https://arxiv.org/abs/1005.4568).
- 3910 [87] Alexander L. Read. "Presentation of search results: The CL(s) technique".
 3911 In: *J. Phys. G* 28 (2002). [11(2002)], pp. 2693–2704. doi: [10.1088/0954-3899/28/10/313](https://doi.org/10.1088/0954-3899/28/10/313).

3913 DECLARATION

3914 Put your declaration here.

3915 *Berkeley, CA, September 2016*

3916

Bradley Axen

3917

3918 COLOPHON

3919

Not sure that this is necessary.